Rheological analysis of ultra-thin polymer films : viscoelastic properties investigation from improved experimental inflation technique coupled with interfeometric microscopy and finite element method

Anastasiia Shpiruk

Université de Strasbourg

Université de Strasbourg

École doctorale
Physique, chimie-physique
ED 182
Université de Strasbourg

ÉCOLE DOCTORALE de Physique et Chimie-Physique (ED182)

Institut Charles Sadron, CNRS UPR22

THÈSE présentée par :

Anastasiia SHPIRUK

soutenue le **24 janvier 2022**

pour obtenir le grade de : **Docteur de l'Université de Strasbourg**

Discipline/Spécialité : Physique des polymères

Modélisation et étude expérimentale des propriétés viscoélastiques de films polymères ultra-minces par technique de gonflement couplée à la microscopie interférométrique.

THÈSE dirigée par :

Dr. Rubin, Anne	Maître de conférences, ICS, Strasbourg

RAPPORTEURS :

Prof. LE BOURHIS, Eric	Professeur, Univesité de Poitiers, ISAE-ENSMA, Poitiers
Prof. CORET, Michel	Professeur, Ecole Centrale de Nantes, Institut GeM, Nantes

AUTRES MEMBRES DU JURY :

Examinateur

Dr. FLURY, Manuel	Maître de conférences, INSA de Strasbourg, ICube, Strasbourg

---

Invités

Dr. ANSTOTZ, Freddy	Maître de conférences, Université de Strasbourg, ICube, Strasbourg
Dr. MONTGOMERY, Paul	Directeur de Recherche, CNRS, Strasbourg
Dr. SOLAR, Mathieu	Maître de conférences, INSA de Strasbourg, Strasbourg

Acknowledgements

First of all, I would like to thank ICS, the lab colleagues and in particular Anne Rubin for welcoming me into the MIM team. Special thanks to the IPP team from ICube: Paul Montgomery and Freddy Anstotz guidance with the setup and constant moral support. Working with them was a real pleasure and the experience that I received from them was precious. I would also like to mention Sébastien Marbach (IPP team, ICube), without whom the experiment wouldn't have started for many more months and who helped me to jump into interferometry more easily. I would also like to thank Mathieu Solar for showing me the world of simulations and for his creativity and ideas.

There would be much less sense in all of it without my friends: Vaibhav Sharma, Nicolas Capit, Imen Ben Djemaa, Marie Sébastien and Eulalie Lafarge. Also, special thanks to Udod Tetiana, Olga Sulialina, the Demydiuk family and Kyivski Bro supporting me and helping me to survive the dark periods.

Of course, I thank my family for constant support in all of my decisions and just for being close to me during these years. Special thanks and place in my heart goes to my family dogs, Molko and Aris.

There are not enough words either to describe how grateful I am to Fedir Demydiuk. This achievement is as much mine as yours. Thank you for being by my side for all these years and many more ahead.

Contents

Chapter 1

Introduction

1.0.1 Context

Polymers are materials with significant advantages in terms of their mechanical stability, flexibility and functionality. Their scope has extensive use in many everyday areas of our lives, in the fields of materials science, industry, medicine, etc. Technical progress requires these materials to be adapted for new forms of use, with modifications in their structure and even the synthesis of new polymers. One of the most important features that is required nowadays from a polymer material is the maintaining of its stability upon reduction in size. According to Moore's law [1], the critical dimension of microelectronic devices was predicted to reduce by approximately a factor of two every year, while the CPU transistor count increased by the same factor of 2. After years of technological progress, the tendency described by Moore's law is a decrease in the size of 0.7 every two years, while the CPU transistor count increase is as predicted Fig.1.1 [2]. Polymers are used as a coating material or as part of the device itself and so are used extensively in microchips, circuit boards, motherboards and energy storage devices etc. as well as optical coatings and in other important applications.

1.0.2 Bulk and ultrathin polymer films

Together with the beneficial characteristics of plasticity, elasticity and endurance of the polymers, these are the reasons for the growth of interest in polymers through the years. Polymers differ from other materials by existence of well-defined characteristic temperature - the glass transition temperature T_g that marks the transition between two states

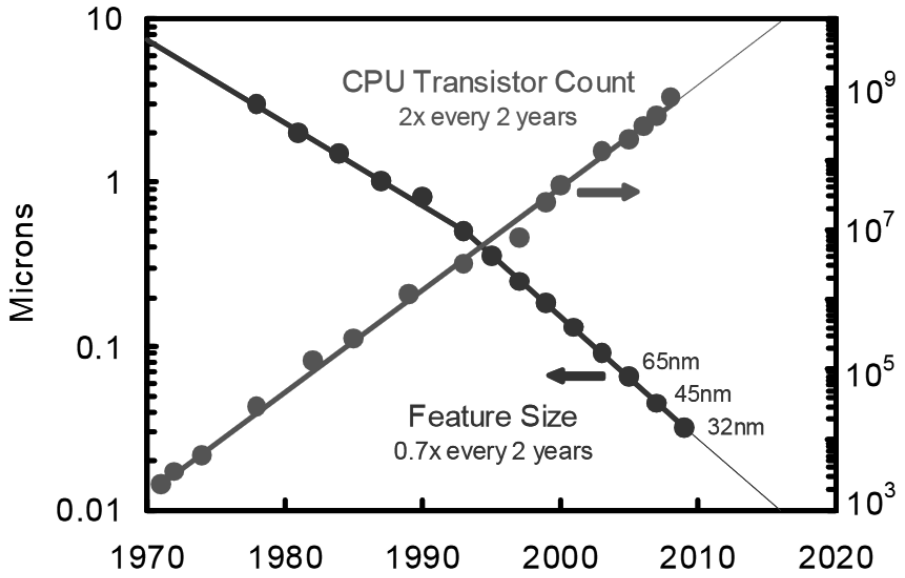

Figure 1.1: Moore's Law: CPU transistor count has increased by 2X and feature size has decreased by 0.7X every two years [2].

of the polymer: a hard and rigid material below T_g and a flexible and soft elastomer-type material above T_g. The significant scientific breakthrough in the area of size-reduced polymers was the investigation of ultra-thin (less than 100 nm) polymer films proposed by Keddie and Jones 25 years ago [3]. They noticed a drastic decrease in the glass transition temperature T_g due to the decrease in the film thickness and marked the beginning of a substantial study of confined polymers. In this thickness range (< 100 nm), the chains of the polymer are so confined that random coils may be denatured. Simultaneously, the nature of the T_g change was noticed to be dependent on the chemical nature of the polymer itself, and on the polymer configuration: a remarkable T_g decrease of up to 80 K for polystyrene (PS) [3] and an ambiguous change (either decrease or increase) of T_g for poly(methy1 methacrylate) (PMMA) [4] which was related to the presence of a substrate or not (free-standing). Afterwards, investigations of one-dimensional confinement effects resulted in studies not only of the static properties of polymer films, but also of the dynamic properties, such as chain mobility and the interaction with the surface, which were found to be the characteristics that cause a reduction in T_g [5, 6]. The complexity in the relation between these factors and understanding the nature and mechanical properties of confined polymers and the polymers themselves are key subject in this field today.

1.0.3 Introduction to this work

The thesis is focused on the investigations of the behavior of ultrathin polymer films and in particular on their mechanical properties under different environmental conditions such as temperature, pressure and humidity. The first polymer that was used in this work is Polystyrene (PS) in order to investigate the influence of different pressure levels and how the polymer film behaves in response to the applied pressure. The second polymer, Poly(vinyl acetate) (PVAc) was used to investigate the influence of different humidity levels on the behavior of ultrathin PVAc films under the applied constant pressure. Finally, the Finite Element Method (FEM) was used in the Marc Mentat environment to simulate the experiment and to obtain the mechanical properties that are not available from experiment.

In particular, we concentrate on the creep effect of ultrathin polymer films and the reaching of the threshold point, with the aim of trying to understand both processes and the transition between them from both, the experimental and modeling points of view.

In Chapter 2 an overview of the literature is given together with the main features of the mechanical and physical properties of confined films in comparison to the bulk, as well as the methods of their investigation and characterization. Chapter 3 presents the materials and methods used in this work. Then, Chapter 4 contains the results and analysis of the experiments on the PS and PVAc films. The results and details of simulations are presented in Chapter 5. Finally, the conclusions and perspectives of the project are given in Chapter 6.

Chapter 2

Bibliography

The bibliography chapter consists of three parts, which explain "*what*" changes in the material in the ultrathin film geometry, using of "*which*" investigation method and "*how*" we observe it:

1. Mechanical and physical properties of the polymer in bulk and ultrathin films;

2. Methods of the ultrathin polymer films investigation;

3. Characterisation techniques for making the observations.

2.1 Mechanical and physical properties of polymer films

The mechanical behavior of polymers in the bulk material is defined by numerous structural factors of polymers: molecular weight, crystallinity, cross-linking plasticization, and others [7]. Beside the structural factors, the environment or external influences are also important in determining the mechanical behavior: temperature, pressure, time and rate of stressing or straining, thermal history, stress and strain amplitude, humidity etc.

The glass transition temperature is considered to be the key characteristic of a polymer and as previously mentioned, is well measured for polymers in the bulk [8]. However, in the first systematic investigations of the T_g in thin polymer films [9] the decrease of the T_g with decreasing of the film thickness was reported. The deviations from the expected bulk values led to the growing interest in studying polymers in confined geometries.

The strong dependence on temperature and time (for example, deformation over time) of the properties is explained by the viscoelastic nature of polymers [10]. This implies the behavior of both the *viscous* liquid (in which the rate of deformation is proportional to the applied force) and the *elastic* solid (in which the deformation is proportional to the applied force). All the work performed on the system is dissipated as heat in viscous systems and is stored as potential energy in elastic systems. For viscoelastic systems, part of the energy is dissipated as heat and part is stored, so that the system creeps under constant stress, but may recover part of its deformation, when the stress is removed.

In this section the overview of the deviations of ultrathin polymer films from the bulk is given.

2.1.1 Mobility

According to J.A.Forrest and K.Dalnoki-Veress [11], polymers as glass forming fluids can be described near T_g as being homogeneous on average, but heterogeneous instantaneously and consists of more liquid-like or more solid-like regions. As these regions are structurally indistinguishable and differ only by the dynamics, the length scale of such dynamics cannot be easily determined. To investigate the length scale the finite size effects of confinement can be used. A polymer molecule can be described by different length scales, from the size of the molecule itself to a single monomer. Accordingly, the characteristic time scale range may vary from the segmental relaxation time to the relaxation time of the entire chain's motion. As the solid-like regions grow with a decrease of temperature, they overcome the different length scales characterizing the molecules or the whole system. So long as the size of these regions is not greater than the dimensions of the confined system and the temperature of the system is high, the system will act like in the bulk. As the temperature is lowered, at some point the confined system is commensurate with the solid-like regions and the dynamics of the system differ compared to the bulk system 2.1.

The dynamics in thin films is characterized by the mobility of the chains, which is usually probed by measuring the diffusion of entire chains. The mobility being influenced by confinement effects is the key concept in understanding the mechanical properties of the films [5, 6]. Besides the external effects of confinement that have an influence on the mobility, there is also an internal effect of entanglement, characterized by the molecular weight M_w of the polymer. Proposed by de Gennes [12], such an effect is explained by the

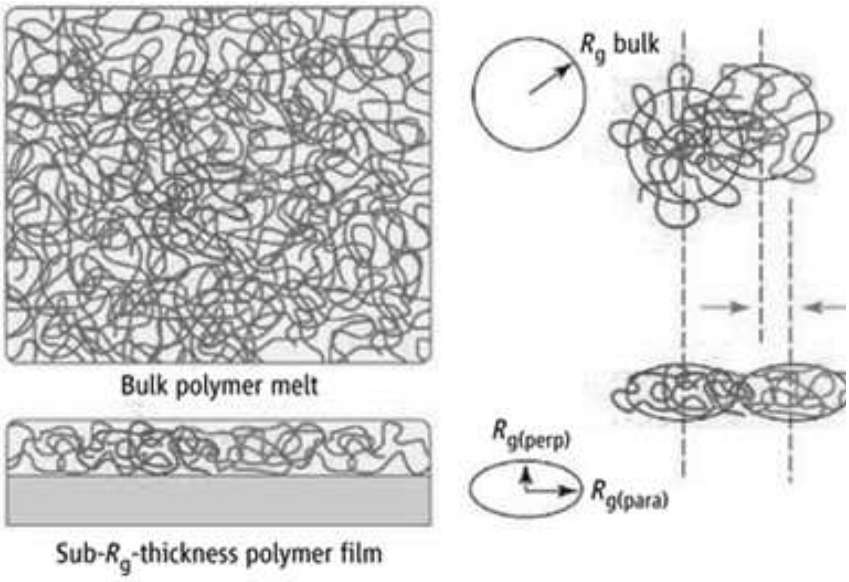

Figure 2.1: The schematic picture of difference between the bulk system and confined system in comparison to the gyration radius of the molecule.

proposal of the entanglement molecular weight M_e, below which the chains are too short to be entangled, so that the mobility of the system is unaltered. For molecular weights above M_e the chains are long enough to be entangled, so the mobility of the system is reduced. The influence of the M_w on the mobility and, consequently, the T_g is given in the § 2.1.2.

2.1.2 Surface effects vs mobility

Supported polymer films

As was mentioned before, the first systematic investigations on confined thin polymer films were performed by Keddie and Jones [3] for PS films supported on hydrogen passivated silicon wafers. The experiments were performed for a range of film thickness (10 - 300 nm) and a range of M_w (120×10^3 - 2900×10^3 Da that corresponds to the root-mean-square end-to-end distance R_{EE} from 20 to 100 nm). The reduction in T_g was found to increase with a reduction in the film thickness, but not dependent on the M_w and the data were described by an empirical relationship:

$$T_g = T_g^{bulk}\Big[1 - \Big(\frac{\alpha}{h}\Big)^{\delta}\Big], \tag{2.1}$$

where T_g^{bulk} is the value of T_g for PS in bulk, h is the film thickness, α and δ are the fit parameters. Such behavior was also detected for PMMA ultrathin polymer films [13]. The tendency of T_g to decrease for supported PS polymer films using different techniques and different substrates is presented in Fig.2.2.

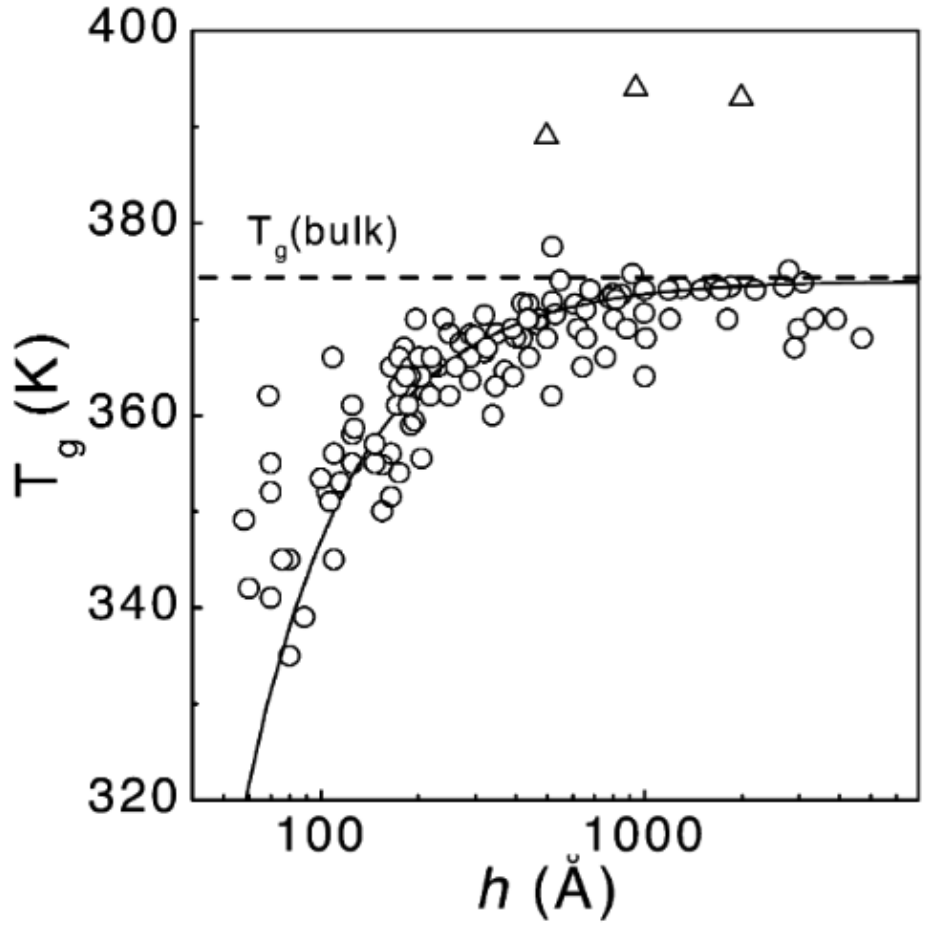

Figure 2.2: Compilation of measured T_g values for supported PS films of different thickness [11] (circles) that obeys Eq.2.1, presented as a solid line. The triangles present the data on similar PS films using the same characterization techniques that result in an increase of T_g compared to the T_g^{bulk} and have been under discussion for many years [11, 14].

The existence of the interaction between a polymer film and a substrate reduces the chain mobility near to the substrate, whereas the free surface was suggested to be liquid-like with an increase in mobility. Obviously, the T_g of these regions will differ, so that the distribution of T_g across the film is of great interest. Experiments with a 14-nm thick labelled layer of PS placed on top, in the middle or near to a substrate of a thick PS polymer film showed a strong dependence of the T_g reduction on the labelled film location and proved the theory of percolation of enhanced mobility from a free surface deeper into a film [15].

Freestanding polymer films

Taking into account the previous slight divergence of the data and the fact that the thickness of ultrathin polymer films could be less than the root-mean-square end-to-end distance R_{EE}, the dynamics of the film could be affected by interaction with the substrate. The solution is therefore to investigate freestanding films, which resolves the impact of such interaction on the results [11]. The first investigation of freestanding polymer films were performed for PS polymer films in the thickness range of 29 - 184 nm and M_w = 760 000 Da using Brillouin light scattering (BLS) [16]. The results of this study were significant for several reasons. Firstly, the T_g values of free-standing polymer films were reduced much more than for supported PS polymer films of the same thickness: for a 20-nm film a T_g was reduced by 70 K below T_g^{bulk}, whereas for a supported film this value was only 10 K. Secondly, the reductions were observed for a greater range of the film thickness: for free-standing polymer films the reductions of T_g were detected at 70 nm, whereas for supported polymer films the reductions were detected at a thickness of 40 nm. Thirdly, the dependence of $T_g(h)$ was qualitatively different from Eq.2.1, so the experiments were broadened to higher M_w and showed the T_g to be strongly dependent on M_w with a visible linear function.

After such results, the interest in the role of M_w became greater and the M_w used in experiments also broadened to low values of M_w. A review of such investigations of the influence of M_w is presented in Fig.2.3 [11].

The complicated behavior of free-standing films from Fig.2.3 showed the strong linear dependence for high M_w, but no discernable dependence for low M_w. The difference in the slope (sharp transition from T_g^{bulk} to lower T_g with decreasing film thickness for high M_w and smooth curve that looks similar to the supported films curve for low M_w) also demonstrates the difference of the transition from T_g^{bulk} to reduced T_g values and marks the difference in the mechanisms responsible for the glass transition. The similarity between the low M_w curve and curve for supported films led to use the Eq.2.1 and resulted in the doubling of the fit parameter α, which can mark the presence of two free surfaces for free-standing polymer films compared to one free surface for supported films [11]. To explain the difference between the two M_w dependence, de Genne proposed the model of two mechanisms for mobility that compete: the first is the small length scale segmental mobility that corresponds to bulk glass transition and the second, in which the polymer

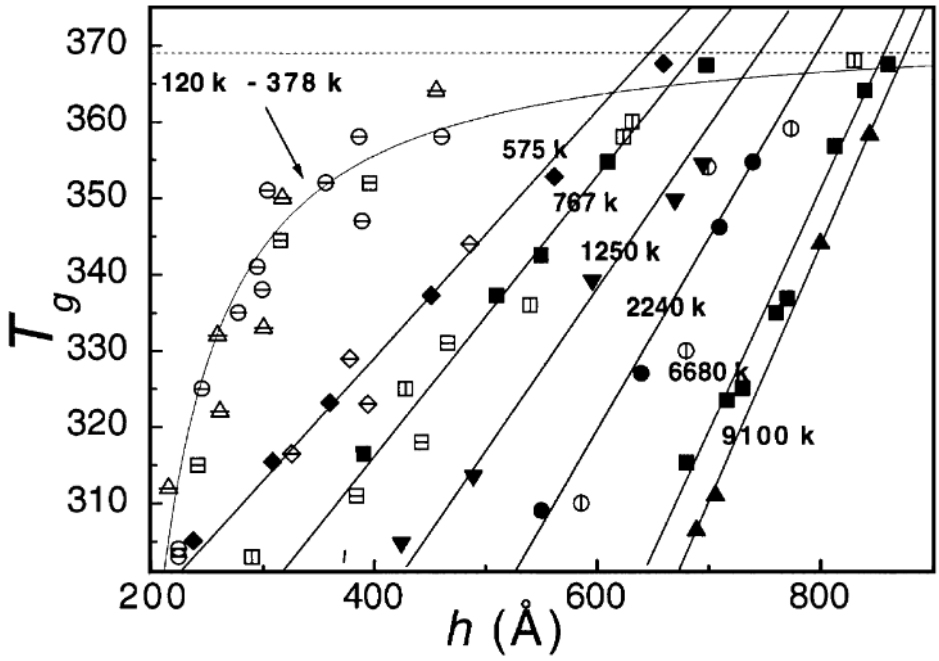

Figure 2.3: Measured T_g for free-standing polymer films for a range of M_w over 120 000 - 9 100 000 Da. The data obtained by BLS technique is marked by hollow symbols: vertical bar indicates data obtained from [17] and horizontal bar indicates data obtained from [18]. The data obtained by ellipsometry is marked by solid symbols [19].

chain "slides" along smaller free volumes [6]. This model describes the data for high M_w, but not for low M_w.

To characterize the polymer film properties without taking into account the interaction with the substrate, we focus on work with freestanding polymer films. Figure 2.3 will be the reference data to define the T_g^{film}.

2.1.3 Viscoelastic properties

Introduction

Viscoelastic functions (focusing on stress and strain here) provide information on the dynamics, on the mechanical behavior of the polymer and even on the structure. The behavior of polymers in the bulk was wide investigated in the last century [10]. The comparison of measurements on the viscoelastic response of ultrathin polymer films is problematic since the measurements can differ according to many aspects: whether it is a freestanding or supported film (liquid support or substrate), which temperature region (below T_g or above, how close to the T_g), which state (rubbery or glassy film, or in the transition mode), with or without annealing (which can influence on the relaxation of

the chains) and, the characteristic times [20]. Such a diversity in the influencing factors requires broader experimental conditions and methods of investigations.

The definition of stress and strain, the simplest polymer deformations and rheological equations that correspond to such deformation, are presented in the Appendix A): Viscoelastic properties of the polymers.

Viscoelastic properties during creep experiments

One of the reasonably uniform ways of investigating the dynamics of a polymer is by measuring its viscoelastic properties in the form of creep compliance, which can be extracted from the stress and strain curve obtained during the creep experiments. However, each method for obtaining stress and strain can differ, so that there is no unique model that can be systematically applied. As the presence of a substrate has an impact on the mobility of the chains (see § 2.1.2), most experiments are based on the use of a liquid substrate (which has no friction and allows the movement of the ultrathin film [20, 21]) or a free-standing film. Representative data on the creep compliance behavior was demonstrated by Bodiguel and Fretigny [20] for various thicknesses of PS films. It has been shown that for thick PS films of 100 nm or more on a liquid substrate, the creep compliance matches the data for the bulk. But for thinner films of 20 - 90 nm thickness, the creep compliance shows a similarity between films of different thickness with only a difference in the shift of the time response (Fig.2.5). In Fig.2.5 can be observed the typical creep compliance behavior with two regimes. In the first regime an increase of the creep compliance at short times corresponds to the end of the transition zone from the glassy state to the melted state with even shorter times for thinner films. In the second regime the slight increase of the creep compliance value corresponds to a rubbery plateau.

In this work we focus on the viscoelastic response of freestanding ultrathin polymer films during the creep experiments.

2.1.4 Humidity

The effect of humidity on the polymers has already been investigated, mainly in terms of vapor sorption of water or ethanol for polymers such as polyurethane [23], poly(vinyl pyrrolidone) [24], and polyacrylamide [25], which are widely used in medicine or as packaging materials, for which the sorption of liquid is undesirable. The complexity appears

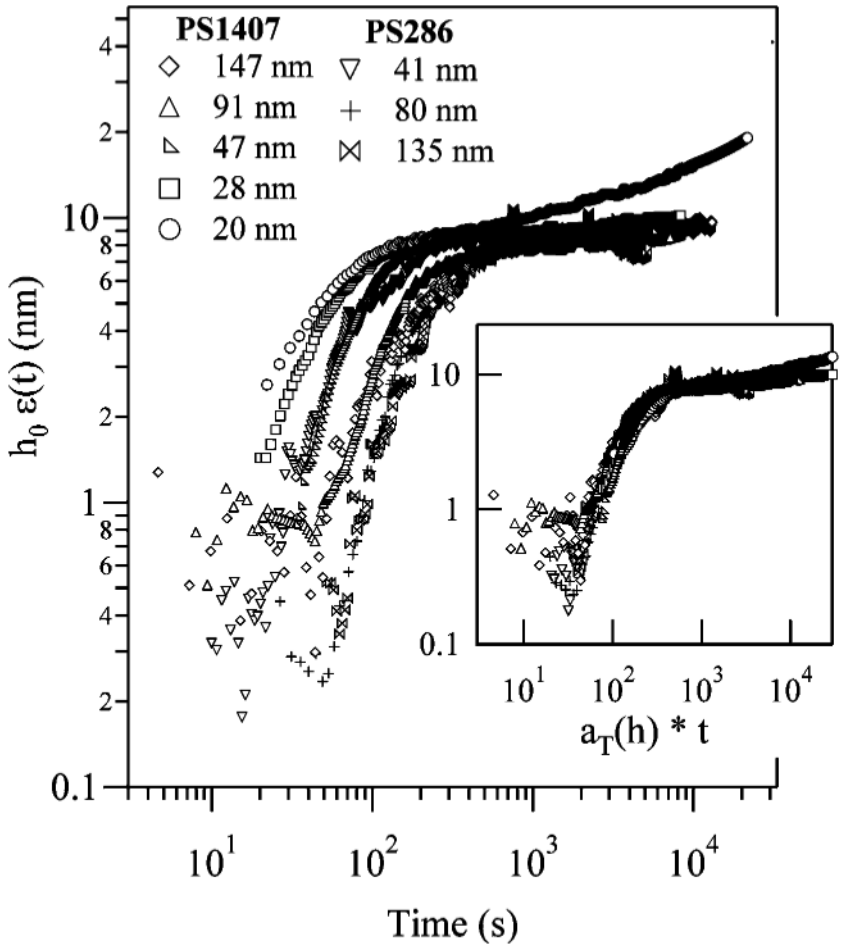

Figure 2.4: Normalized creep compliance for PS1407 (M_w = 1407 kg/mol) and PS286 (M_w = 286 kg/mol) films of initial thickness from 20 to 150 nm. Temperature 105.5°C. The inset figure shows superposition of the creep compliance curves of different thickness, obtained by multiplying the experimantal time by a shift factor $\alpha_T(h)$ [20].

to be due to the dependence of the polymer configuration (bulk or film, supported polymer or free-standing) or of the polymer itself: some polymers were reported to not have their characteristics influenced by adding moisture to the polymer [26]. During the vapor sorption, the polymer film gains the mass of the vapor and, structural changes within the film can occur, such as relaxational effects of the polymer side chains, free volume variations, the lowering of glass-transition temperature, and an increase in the viscoelastic behavior [23]. The plasticization mechanism is attributed to the increasing of free volume and lubrication provided as the water swells the polymer and disrupts polymer-polymer hydrogen bonding [27].

Poly(vinyl acetate) or PVAc, a polymer of the hydrophilic group, was reported to have an ability to absorb a certain amount of moisture, which causes the plasticization of

the polymer chains [28, 29]. Ultrathin polymer films of PVAc of 20 nm were reported to have a decrease in plasticization with water for high annealing temperatures ($T_g + 60°C$) compared to lower annealing temperatures [30]. Also, the interaction of two similar ultrathin polymer films with two different substrates of hydrophilic Al and hydrophobic Au showed the bigger increase of relaxation rate with humidity of the latter [24, 30]. Such results lead to the assumption that the level of water accumulation depends on the type of substrate used. The presence of moisture in PVAc ultra-thin films of 23 nm also acts on the change of the T_g values: for "wet" PVAc films the T_g is higher then for a "dry" one [31]. On the contrary, some results show a decrease of T_g for the 28 nm thick PVAc freestanding polymer film [29] with an increase in the humidity level.

For Polystyrene (PS) polymer films the effect of water plasticization has not been reported in the literature, but for plasticization of polystyrene other solvents, so-called plasticizers, were added during formation of the film, such as terephthalate and phthalate [32]. Also, the CO_2 gas sorption into the PS polymer film has an impact on the plasticization and results in permeability, sorption, and diffusivity changes, which additionally depend on the thickness of the PS films [33, 34]. Taking into account the different responses of PVAc and PS on the moisturizing of polymer films with water, another goal of this work is therefore to investigate the influence of the humidity level on PVAc ultra-thin freestanding films compared to the behavior PS films as a reference of not being sensitive to humidity.

2.2 Methods used to investigate ultrathin polymer films.

Along with the increasing interest in research on ultrathin polymer films, a variety of investigation methods have been developed over the last decades. The measurement of the properties of ultrathin polymer films can be a challenge due to the reduced thickness of the specimen, especially for a freestanding polymer film (see § 2.2.3). In this chapter the main methods o used for investigating the characteristics and properties of ultrathin polymer films are presented.

2.2.1 Surface effects

The first indications of enhanced mobility in thin polymer films were deduced from optical microscopy experiments on breakup or **dewetting** of the polymer films at $T < T_g$, based on the formation and growth of holes in the film, which are directly related to the chain motion [35]. Thin polymer films can be inclined to the formation of holes during heating to the temperatures close to T_g or above. The motion that causes the hole formation initially occurs perpendicularly to the film plane direction, whereas the motion during hole growth is predominantly in the plane of the film [5]. Such experiments can be complicated due to the presence of large stresses (due to the dispersion interaction and surface tension interplay) and the importance of nonlinear viscoelastic effects [36] on the process of hole formation and growth.

The **differential pressure** experiment was developed for probing the hole growth in thin freestanding films down to 51-nm thickness at elevated temperatures, but not higher than T_g^{bulk} due to the rapid growth of holes for high temperatures [37].

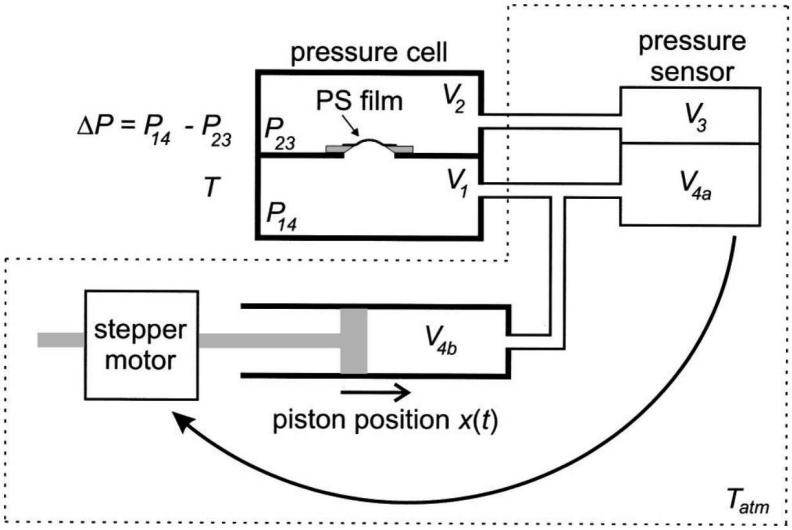

Figure 2.5: Schematic diagram of the differential pressure experiment for probing the hole growth in thin freestanding films [37].

A constant small pressure difference is applied across the film using a piston and the formation and growth of holes is detected as a flow of air through the film. The time dependence of the piston position provides the moment at which holes are formed and can be analyzed to obtain the characteristic growth time. It was shown that hole growth and corresponding whole chain motion occurs only for temperatures close to T_g^{bulk} [5].

2.2.2 Mobility

To probe the molecular mobility in thin polymer films, it is necessary to use a technique that has high sensitivity, because of the small sample volume, or surface sensitivity if surface properties are desirable because of the large surface-to-volume ratio in thin films. In addition, investigation of the chain mobility itself is a challenge due to the scale of the polymer molecules and chains. Basically then, mobility studies come down to measurements of the T_g distribution across the thickness of the polymer film, as first proposed by de Gennes [6].

One such technique is **fluorescence emission intensity**. The fluorescent dyes used as local probes of T_g provide unique advantages in multilayer film investigations. By placing a dye within a single layer of a multilayer film, T_g can be probed as a function of distance from an interface or surface (Fig.2.6). For 14 nm-thick labelled PS polymer film

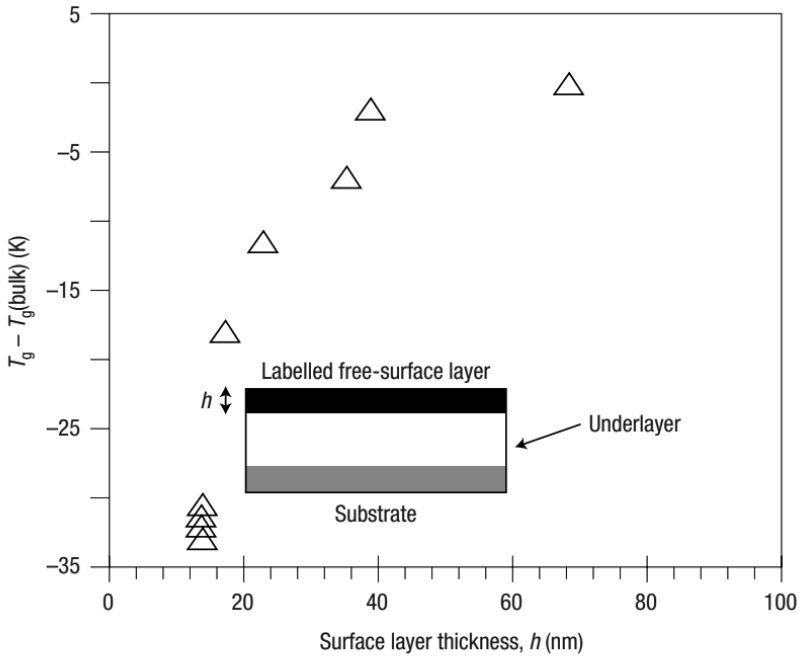

Figure 2.6: The difference in T_g from T_g^{bulk} measured by fluorescence depending on the thickness of labelled polystyrene free-surface placed on top of bulk-like polystyrene underlayers [15].

on top of bulk-size PS film the reduction in T_g was found to be 32 K compared to the bulk T_g, whereas the same 14 nm-thick PS film sandwiched between two 270 nm-thick PS films showed no T_g reduction, which proves the assumption concerning enhanced mobility of the free-surface layer of ultrathin polymer films [15].

Alternatively, **dielectric spectroscopy** can be adapted for the multilayer approach to determine the profile of the structural relaxation time-resolved along the thickness [38]. This method allows the investigation of the relaxation processes and relaxation time distribution for a broad frequency range for temperatures extending from above to below the bulk glass transition. In addition to the depth T_g profile, the method allows the measurement of the dielectric strength (quantitatively proportional to the amount of mobile molecules) and to map the molecular mobility. The experiment with a labelled 15 nm-thick PS polymer film on top of a bulk-thick PS polymer film showed a drop in 85% of the dielectric strength compared to the same 15 nm-thick PS film placed between two 45 nm layers of neat PS, which exhibits a bulk T_g with no changes in dielectric strength to the bulk. It was shown that polymer properties recovered bulk values at a distance smaller than 45 nm from the surface of the ultrathin polymer film [38].

2.2.3 Mechanical properties

By analogy to the simple shear experiments with sudden strain or sudden stress applied (see A.3-A.4), the simple tensile experiment can be performed to measure the response of the material from the applied stress or strain. If the simplest experiments presented above are not possible (for example, due to confined dimensions of the specimen), there are other options available.

Nanoidentation consists of instruments based on the point-probe technique to test thin films and surface mechanical properties. It was developed from the combination of two different methodologies [39]: scanning probe microscopy and microindentation. Unlike scanning probe microscopy, during the nanoindentation experiment an external load is applied to the indenter tip, which enables the push of the tip into the sample creating a nanoscale imprint on the surface. On the other hand, unlike microindentation or conventional indentation experiments in which the analysis uses optical imaging of the indentation imprint, the nanoindentation method was developed to record continuously the load, displacement, time and contact stiffness (which can be interpreted into elastic modulus or hardness of the material). The method is suitable for perfect elastic-plastic materials that have a linear stress-strain curve until they reach their elastic limit, above which they yield plastically at a yield stress value that remains constant during the ensuing deformation.

For the thin polymer films investigation using nanoindentation, a few factors should be mentioned. The indentation experiment requires the penetration of the tip inside the material for some depth. Depending on the thickness of the film, this depth can be limited due to the integrity and changes in the properties of the sample, but which gives the opportunity to measure mechanical properties depending on the depth of penetration. It is common to restrict the maximum depth of penetration in a test to no more than 10% of the film thickness for a rigid substrate [40], which for ultrathin polymer films can be only a few nanometers and leads to high errors in the experimental data or requires the performing of a modeling test. Additionally, the presence of the substrate (no information exists on freestanding ultrathin polymer films) and the material from which it is made and the wetness of the sample can also have an influence on the behavior of the sample during the experiment.

Elastic buckling in the form of wrinkling instability experiments helps to measure the elastic moduli of thin (and also ultrathin) polymer films. The system consists of a soft linear elastic substrate and a thin film, which is stiffer compared to the substrate. When uniaxial compression is applied, the thin polymer film undergoes periodic buckling and starts to wrinkle with a characteristic wrinkling wavelength, balancing between the plate's bending energy and the energy required to deform the underlying substrate [42]. By knowing this wavelength λ, the thickness of the stiff film h and elastic modulus of the substrate E_s, the elastic modulus of the film can be found [41]:

$$E_f = 3E_s\Big(\frac{\lambda}{2\pi h}\Big)^3. \tag{2.2}$$

Even with such a simple computation, the system has some limits. As the wavelength depends linearly on the film thickness, optical microscopy cannot be used for polymer films thinner than 50 nm [42] due to the lateral resolution limit, so Atomic Force Microscopy (AFM, see § 2.3.2) can be used to obtain the profile of the wrinkled film. This method is possible only for supported polymer films, and the influence of the substrate on the mechanical properties of the film is still under the investigation. Therefore, there are methods that allow the measurement of the mechanical properties of freestanding polymer films. One of them is based on the **uniaxial tensile tester** for ultrathin (down to 32 nm-thick) freestanding films [43]. The freestanding film is attached to the holder from one side and to the cantilever from the other 2.7. The cantilever is calibrated for force

and displacement, and moves at a fixed speed, so that the film stretches at a fixed strain rate, and the strain and stress can be calculated from the film's geometry.

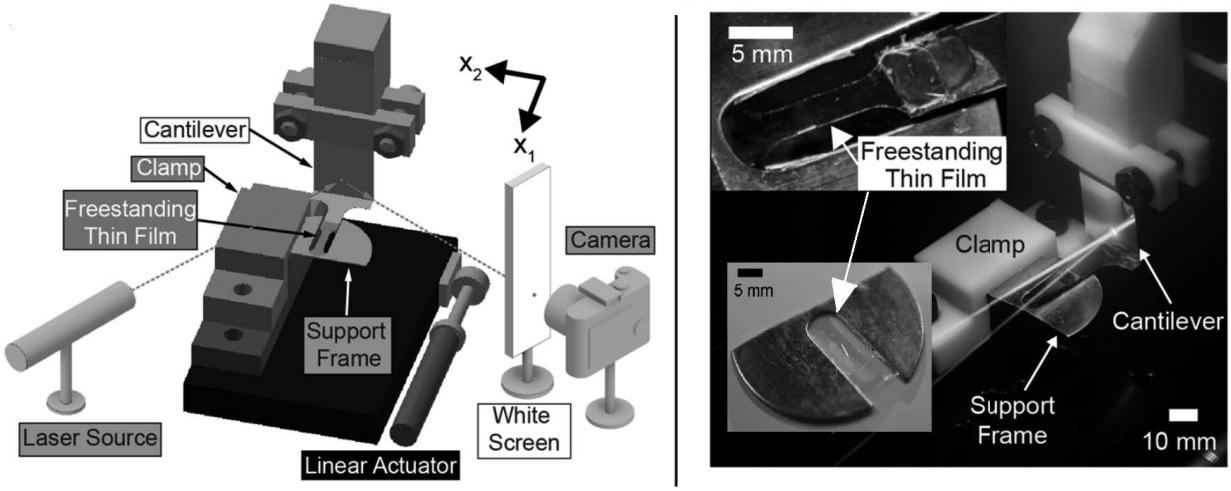

Figure 2.7: The setup of tensile tester for ultrathin freestanding polymer film: schematic picture on the left and real picture with loaded 100-nm thick polystyrene polymer film into the setup [43].

Another option for the investigation of the mechanical properties of freestanding polymer films is the **microbubble inflation technique**. The polymer film is placed on top of a grid consisting of circular holes. It is attached by adhesion between the film and substrate, but remains freestanding in the holes. The polymer film is inflated using pressurized air. By measuring the evolution of the radius of curvature of the bubble, strain and stress can be calculated to obtain the creep compliance [44]. This method is suitable for any polymer film thickness down to a few nm, since the pressure can be regulated to obtain the creep regime of the material deformation and does not have any contact (like with the substrate or cantilever) which can influence the properties of the specimen. These characteristics make the bubble inflation technique the most convenient choice for the investigation of viscoelastic properties of freestanding ultrathin polymer films in this work and is presented in detail below (see § 3.3).

2.2.4 Finite element method in ultrathin polymer films

The finite element method (FEM) has been used for the modeling of ultrathin polymer film systems to mimic and complement the experimental data in order to extract the mechanical properties of the polymer films.

FEM is also used to calculate the electric and magnetic field distribution in the film or

the displacement of the film under load that helps to predict the limits of the elastic-plastic ranges and the rupture of the film [45–47].

The modeling using FEM for ultrathin poly(vinyl formal) films of 100 nm thickness based on the experiment of the indentation probes with an indenter ball showed not only an agreement with experiment, but also allowed the investigation of the elastic and plastic cases of film behavior under the indentation loads [45]. The main complexity of such an approach is to determine a balance between the elastic modulus and pre-strain or pre-stress of the membrane to have an agreement with experimental data, which can be solved by optimizing the calculations of these parameters [45, 48, 49]. Similar results were obtained for experiments and FEM modeling of nanoindentation with different tip geometries by using the FEM of the elastic modulus of ultrathin polymer films by correct calibration and subsequent simulation of the effective nanoindenter geometry Fig.2.8[48, 49].

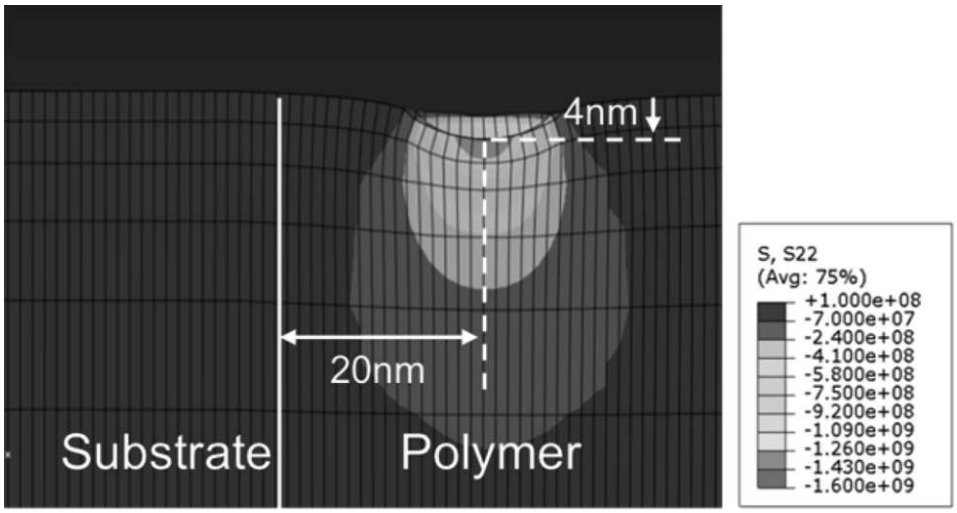

Figure 2.8: Stress fields ($S_2 2$) calculated by FEM for polymer close to the substrate for an indentation with indentation depth of 4 nm. The polymer is purely elastic. The unit of the color bar of stresses is Pa [49].

FEM has been used in parallel to experiments to model the microbubble inflation technique on ultrathin PS polymer films of 30 nm for different geometries of the membrane, either circular or rectangular in shape in order to investigate the influence on the viscoelastic response [47]. The result showed no difference in the rubbery plateau compliance curves and T_g for both geometries, which leads to the conclusion that the bubble, formed from the inflation, is equibiaxial versus plane strain for both cases.

In this work we present the model of the microbubble inflation technique for the creep experiment using FEM.

2.3 Characterization techniques

Apart from the methods for the investigation of ultrathin films described in the previous chapter, the characterization techniques for observing the changes in the film's behavior or structure caused by these methods should also be discussed. In this chapter the common characterization techniques are presented.

2.3.1 Ellipsometry

Ellipsometry is a non-contact optical technique that measures the change in polarization of the light after being reflected from the sample. The most common use of ellipsometry involve measurements of the thickness (or the layers) and the optical properties of the sample (such as refractive indices), but it is also suitable for the investigation of the roughness and the analysis of the oxidation or corrosion of metals, etc.

The use of ellipsometry became popular in the 1960s for reflective materials (SiO_2, gold, titanium, aluminium, etc.), but later became effective for thin organic or polymer films placed on top of a reflective material [50]. The range of thicknesses suitable for ellipsometry varies from nm to μm with an analytical sensitivity of 0.2 nm [50]. In the field of ultrathin polymer films, ellipsometry was used starting from the first investigations of the T_g decrease by Keddie et al. by detecting the discontinuity in thermal expansion occurring at T_g for supported films [3, 4, 9, 17] and freestanding films using transmission ellipsometry, where instead of a reflected light beam, the transmitted through the transparent polymer film light is investigated [19, 51].

The diagram showing the working principle of ellipsometry is presented in Fig.2.9 [52].

The significant question concerning ellipsometry appears when one considers if the error and thickness range is suitable for this technique. Ellipsometry is a technique that is based on determining the change of polarization of light after reflection on the sample, expressed by the Ψ and Δ angles. By fitting the data of these two angles to the generated model, there are more sources of error starting from standard deviation down to systematic errors of experimental data. The errors can be calculated and minimized for each case by using the formulas for all type of errors: sensitivity error, error of output optical constants and output fit residual error [53].

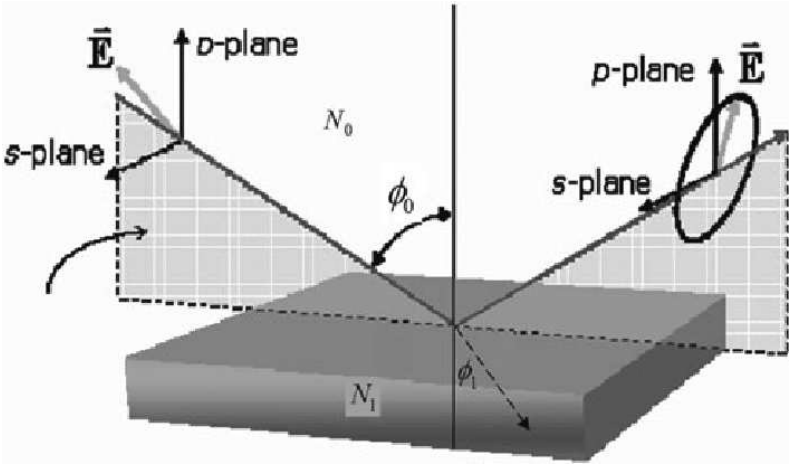

Figure 2.9: The ellipsometry diagram. N_0 and N_1 are the complex indices of refraction, while f_0 and f_1 are the incident and the reflected angle. E is the laser electric field, and s and p are the two distinct polarizations [52].

2.3.2 Atomic Force Microscopy (AFM)

Developed by Binnig et al. in 1986, the AFM principle came from the combination of Scanning Tunneling Microscoy (STM) and stylus profilometry [54]. STM is based on the tunneling phenomenon in vacuum to measure the current of the electrons tunneling through the gap created between the tip and the nearby atoms of the sample's surface. From the stylus profilometer the movable soft cantilever was then taken with an improvement in the ultrasmall mass of the cantilever with a diamond tip on the edge. The result of AFM is an image of the sample surface, obtained by measurement of the force on the tip depending on the proximity to the sample's surface. The AFM technique was developed due to a demand in the increased sensitivity of the method and decreased forces of interaction between the tip and a sample to the interatomic forces between single atoms (the range of forces was decreased to 10^{-18} N compare to 10^{-5} N from STM). The diagram of AFM principle of work is given in Fig.2.10 [55].

The mode of AFM just described is now referred to as the contact mode, since the interaction of a tip with a surface of the sample was significant and close to the surface. Thus AFM was first used for metals and rigid samples. As for the soft materials such as polymers or biological materials, the interaction between the tip and the surface was much weaker and caused damage of the sample surface. So, over the following 10 years the non-contact mode [56] and later, the tapping (dynamic) mode were developed, with both having the oscillating cantilever in the attractive regime close to the surface that minimizes any contact and damage with the surface. The tapping mode has the additional

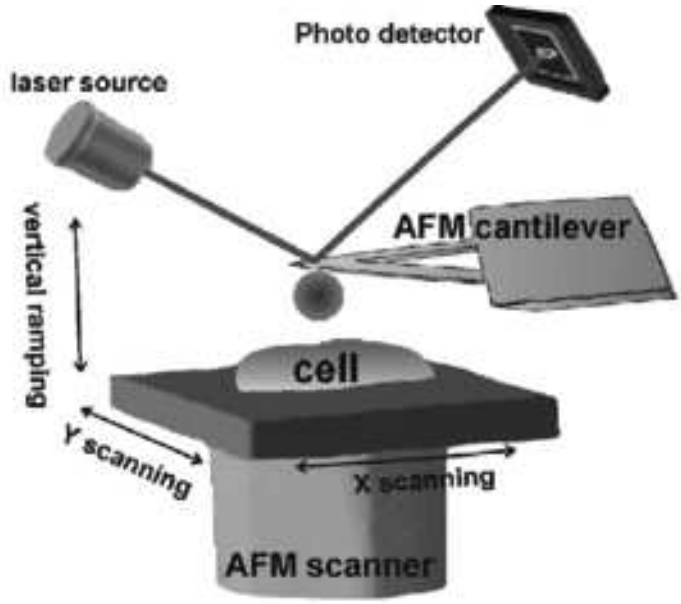

Figure 2.10: A scheme of AFM method [55].

advantages of the proximity to the sample and a decreased amplitude of the oscillations [57]. As the main idea of AFM is to obtain the picture of the sample surface, the usage of this technique concerns measurements of the sample topology, including thickness. But it also helps in investigating the material properties (elastic modulus, stiffness, etc). In the latter case, AFM comes close to nanoidentation (see § 2.2.3) with a controlled contact force beyond the yielding point to prevent the distortion of the surface and/or to obtain data [58, 59].

AFM was used in the experiments on ultrathin polymer films performed by McKenna et al. along with the microbubble inflation method for the investigation of the viscoelastic properties (see § 2.2.3) [29, 44, 60]. Using AFM, the shape of the bubble can be obtained for further calculations of the viscoelastic properties.

Despite the wide and simple use of AFM with the possibility of direct access to the sample, there are limitations of the technique. Firstly, obtaining each frame of a relatively small area of interest requires a significant amount of time (up to 4 minutes for 23 μm $\times$ 23 μm image [60]), which can lead to distorted images due to the evolution of the sample over time. Secondly, this technique has the risk of random disturbance of the sample surface by the tip, which can lead to an error in the stress-strain data or damage of the sample.

Although there are developments in advanced high-speed AFM, up to 1000x times

faster than traditional AFM (2-8 frames per second [61]), it is still limited in frame size to 1-4 μm and because of the high-frequency movements of the tip, the contact load causes more damage to the surface of soft samples [62].

2.3.3 Interference microscopy

Interferometry plays a central role in the investigations of surface topology down to nanoscale structures that results in 2D or 3D images of the sample surface. The manufacturing of high-quality optical surfaces require the precise analysis of the sample topology and local surface roughness. The surface also carries information about functional properties (lubrification, adhesion, friction, leaks, corrosion) of components and systems [63]. The diagram of the Michelson interferometer is presented in Fig.2.11 [64].

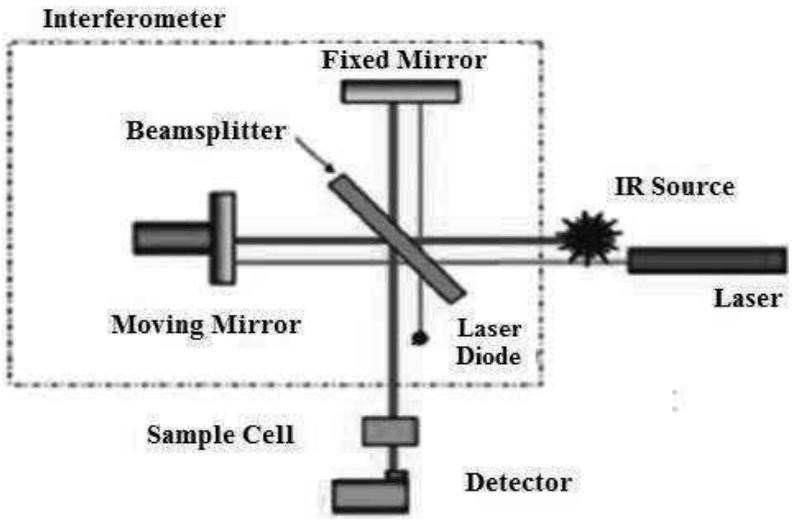

Figure 2.11: The diagram of the most used interferometer - Michelson interferometer [64].

Interferometry can also be used to investigate thickness related aspects such as the thickness of thin coatings, the detection of film defects, the topology of thin coatings, especially for transparent films. Although, the interaction of the light with a transparent film can lead to difficulties in interpreting the mix of the reflected signals [65, 66], especially for ultrathin films [67], this technique has significant advantages. Firstly, it is non-contact and non-destructive, so it can be used for supported or freestanding films of any thickness. Secondly, interferometry has an advantage in the area of the measurement: for example, ellipsometry is a single point technique covering an area of a few μm^2, whereas for interferometry it extends to the field of view of the objective ($\sim$ 100 μm $\times$ 100 μm) with sub-micrometre resolution. Thirdly, the time required for one frame takes

seconds with a significant area of sample that can result in better statistics.

This technique is compatible with the microbubble inflation method of ultrathin polymer films investigation. Such a setup has been developed by the MIM team of the Institut Charles Sadron (Strasbourg, France) and the IPP team of the ICube laboratory (Strasbourg, France) to perform the investigations of freestanding ultrathin polymer films under different conditions of pressure, temperature and humidity [68], which is the goal of this work. The detailed description of the setup and method is given in Chapter 3.

Chapter 3

Materials & Methods

In this chapter we present the protocols of sample preparation for the experiment, including polymer solution preparation, film formation and deposition of the polymer film on top of the grid substrate. The details of the microbubble inflation technique and interference microscopy system used for the experiment are also explained. Finally, the procedure for the analysis of the data is presented.

3.1 Polymer film. Protocol.

In this work we use two polymers **Polystyrene (PS)** and **Poly(vinyl acetate) (PVAc)**:

- **Polystyrene (PS)**, manufactured by PSS Polymer Standards Service GmbH, Germany, M_w=120 000 Da, PDI=1.05, T_g=100°C.
- **Poly(vinyl acetate) (PVAc)**, manufactured by Sigma-Aldrich, Germany, M_w=100 000 Da, PDI=2.6, T_g=30°C.

PS polymer films were used to perform creep experiments at ambient humidity, and PVAc polymer films were used to perform creep experiments with controlled humidity to investigate the influence of humidity on the creeping of the polymer film.

3.1.1 Polymer solution

The polymer solution is prepared by adding toluene (Sigma-Aldrich) to PS in a glass bottle in different weight-by-weight concentrations. A small stirring magnet, also cleaned in toluene, is used to ensure the dissolution of the polymer at room temperature for 1h.

The concentrations used for the polymer solution were the following:

- **PS**: from 0.7% to 1.6% by w/w.
- **PVAc**: from 2.6% to 2.8% by w/w.

3.1.2 Film formation

The procedure of the film formation and characteristics of the spincoating procedure is identical for both the PS and PVAc polymer films.

A silicon wafer ∼2 cm^2 is used as the substrate for polymer film formation. Cleaning of the silicon wafer consists of several steps. Firstly, it is placed in hydrofluoric acid (HF) for 5 minutes, then rinsed with plenty of deionized water and dried with a nitrogen flow. Secondly, it is exposed to the Ultraviolet-Ozone for 1 hour. Afterwards, the silicon wafer is cleaned with a few rinses using acetone and ethanol, and again dried with a nitrogen flow.

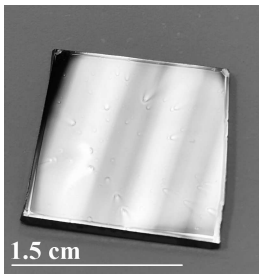

Figure 3.1: The PS polymer film on the top of silicon wafer after spincoating procedure.

A spin-coater is used for the polymer film formation. Before adding the solution (toluene or PS/PVAc-solution) to the silicon surface, a nitrogen flow is used to remove dust from the silicon surface. The cleaned silicon wafer is placed on the nozzle hole, which is connected to the pump that creates the vacuum-like environment, so that the substrate is fixed. A last cleaning step of the surface of the silicon wafer consists of dropping the 120 μl of toluene on the top of silicon surface and spin-coating for 30 sec at a speed of 5000 rpm (500 rpm/sec acceleration), a step which is repeated twice.

The film is formed from 120 μl of polymer solution which is spin-coated for 1 min at a speed of 2500 rpm (500 rpm/sec acceleration) (Fig.3.1).

The thickness of the polymer films on top of the silicon wafer after film formation process was measured using AFM and ellipsometry (Table 3.1).

3.1.3 Film deposition on top of the grid substrate

To ensure the freestanding polymer film configuration, the Si_3N_4 grids (5 mm × 5 mm, Aquamarijn Micro Filtration BV, Netherlands) with a regular array of 5 μm holes were

Material	Concentration	Measured thickness (AFM)	Measured thickness (Ellipsometry)
PS	0.6%	24 ± 2 nm	-
PS	0.7%	28 ± 2 nm	27 ± 1 nm
PS	1.2%	63 ± 4 nm	-
PS	1.6%	80 ± 4 nm	-
PVAc	2.6%	110 ± 5 nm	105 ± 3 nm
PVAc	2.8%	120 ± 5 nm	-

Table 3.1: Measured thickness of the samples for several concentrations of PS and PVAC by AFM and ellipsometry. The ellipsometry measurements were performed for a few samples only, concentrations of which were used mostly in experiments, in order to validate the AFM measurements.

used as a substrate for the inflation method (Fig.3.2).

Before placing the polymer on top of the grids, the grids were cleaned in toluene for 1 h and left to dry in air for 15 minutes under an air hood. Then, 4 grids were placed on top of an aluminium holder and placed in a petri dish with ultra-pure water. For good detaching of the polymer film from the silicon, the edges of the polymer film were removed with a razor. The polymer film was detached from the silicon wafer by bathing it in ultra-pure water in a petri dish, so that the polymer floated on top of the water. Then, the polymer film was taken by pulling out the holder with the grids.

Afterwards, the grids with the polymer film is left in air (but with the petri dish above as a covering to prevent the dust falling on top of the polymer film) for 24 hours to evaporate excess water on the grids and aluminium holder.

3.1.4 Annealing

The annealing of the "polymer film - grid" system provides the adhesion of the polymer film to the grid and relaxation of internal stresses of the polymer film after the spin-coating film formation. This was performed below the temperature $T = T_g^{film} + 10°\text{C}$ for 1 hour and with a temperature fluctuation of ±2°C. The temperature during annealing was measured continuously with a K-type thermometer. As the T_g differs for the PS and PVAc, the annealing temperature was different:

- **PS**: The T_g^{film} depends on the thickness of the film. The data of the T_g^{film} dependence on the polymer film thickness was taken from the literature [9]. For a 30 nm-thick PS polymer film, the $T_g^{film} = 72°\text{C}$, so the annealing temperature T_{ann}

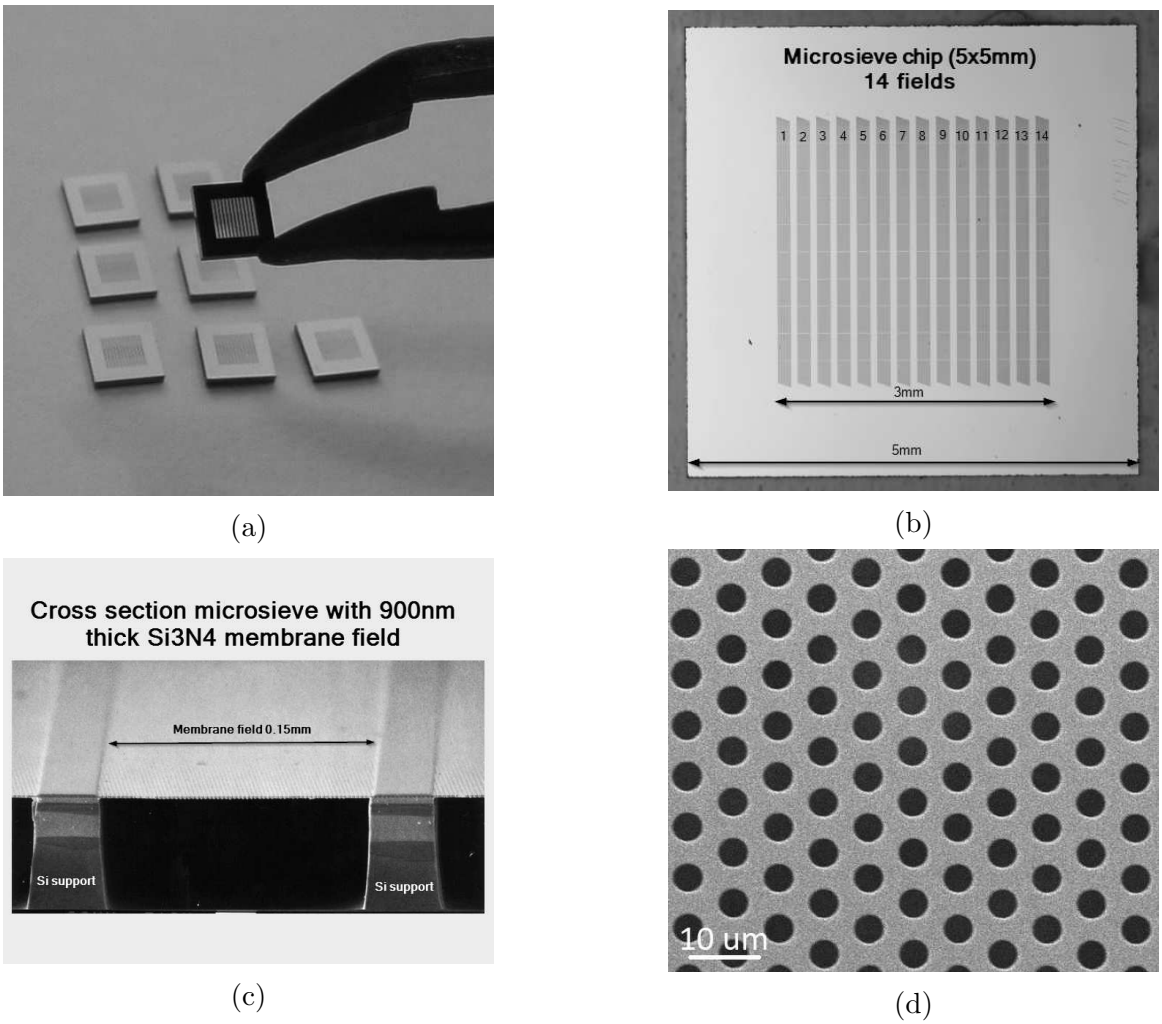

(a) (b) (c) (d)

Figure 3.2: The grid as a substrate of the polymer film: (a) Picture of the grid. The stripes inside the grid correspond to the 14 membranes of Si_3N_4, presented in details in (b) and closer in (c). Each of the membrane contains the holes of 5 μm diameter presented in (d) [69].

was set to 82°C.

- **PVAc**: The glass transition temperature of PVAc polymer films is reported to have no decrease in the T_g^{bulk} for thicknesses down to 67 nm [70], so the $T_g^{film} = T_g = 30$°C. The annealing temperature for the PVAc polymer film was set to 40°C.

After the annealing the sample was cooled down to room temperature for 20 minutes and could be used up to 1 hour after the procedure.

3.1.5 Capillary forces

During the annealing process, the polymer film is drawn inside the holes of the grid due to the capillary effect (Fig.3.3, [60]).

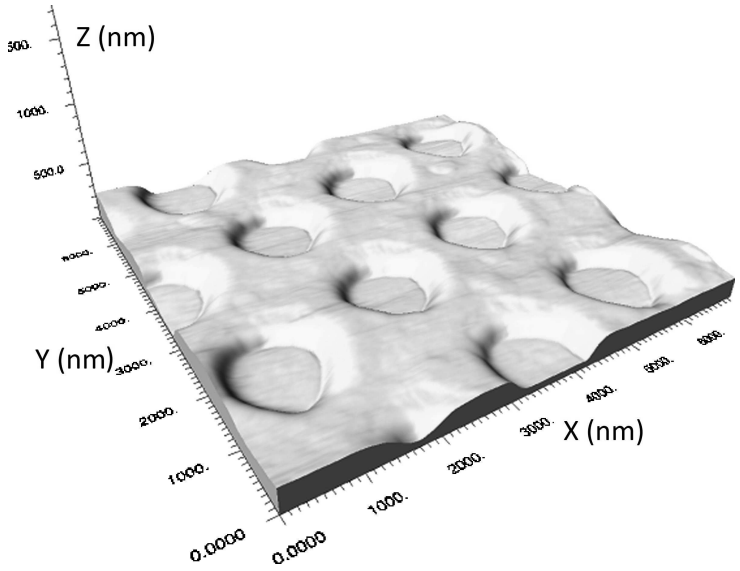

Figure 3.3: Three dimensional AFM image of a coated unpressurized template of polymer film - grid system after annealing at 40°C. The PVAc film is 27.5 nm thick and is scanned at a temperature of 23°C. Capillary forces have drawn the film into the hole to a depth of approximately 200 nm [60].

The effect of the polymer film being drawn into the grid holes was observed for both the PS and PVAc polymer films of different thicknesses.

3.2 Experimental Setup

During the experiment, the pressure, temperature and humidity (for PVAc creep experiments) were controlled to keep the polymer film in the required conditions for performing the creep of the polymer film. In this section a detailed description of the setup used to obtain and regulate these conditions for the experiment is presented.

3.2.1 Pressure cell

The pressure cell used in the present work was developed and custom made by the group (MIM, ICS and IPP, ICube), the fruit of collaborative work since 2016. The first prototype developed by Pierre Chapuis (IE CDD), built around an aluminium base, had temperature and pressure control and led to the first successful measurements on the bubble inflation (Fig.3.4) [68].

The second prototype, also built by Pierre Chapuis, provided improved humidity control as well as the heating of the sample and simultaneous pressure control during the

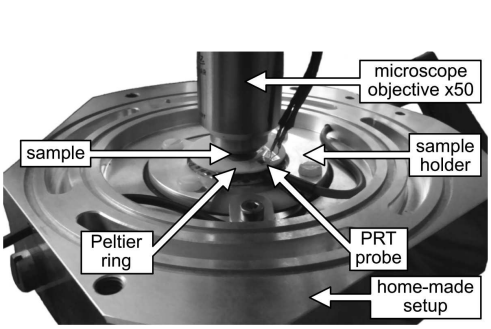

(a)

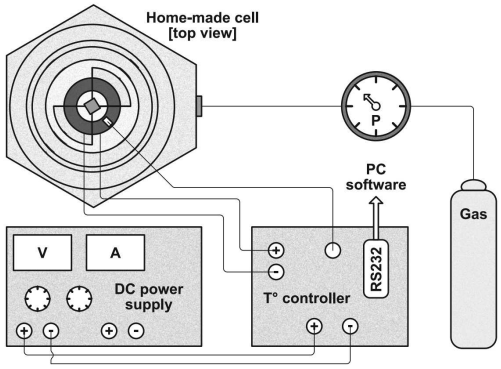

(b)

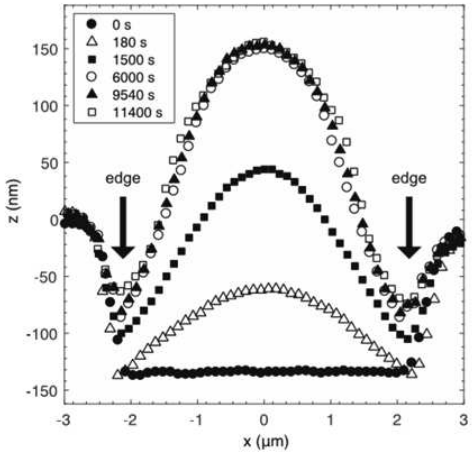

(c)

Figure 3.4: (a) Picture of the first prototype of a custom-made pressure cell with a pressure and temperature controls; (b) The scheme of the first prototype of the experiment. The Peltier ring is controlled by a temperature controller. The sample is symbolized as a gray diamond in the center of a cell; (c) An example of bubble inflation with time for PVAc polymer film [68].

experiment.

It is composed of an aluminium base and aluminium-Teflon holder to fix the sample (Fig.3.5a). The temperature detector is placed on the bottom of the upper part of the cell, which also contains the humidity detector and the four holes for the moisturized nitrogen flow output (Fig.3.5).

The sample is attached to the Teflon stand containing a hole for the pressure. To assure no leaks and for fixing the sample, a double sided adhesive tab (Ted Pella, Inc.) was used. By cutting out a square in the middle of the adhesive tab, the sample is attached to the sides of the Si substrate, only to the grid, so preventing damage to the Si_3N_4 membrane. Afterwards, the aluminum holder is attached with screws to the base so as to fix the sample. The holder was designed with the Peltier ring around the sample

for even heating of the sample. Then, the upper part of the cell is placed on top of the holder and Peltier ring. The full coverage of the Peltier ring with a cell minimize the heat loss. The schematic diagram of the cell and sample is presented in Fig. 3.6.

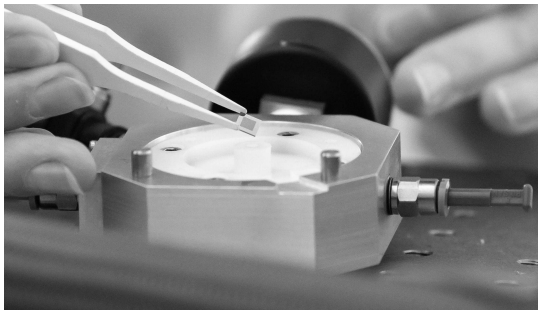

(a)

(b)

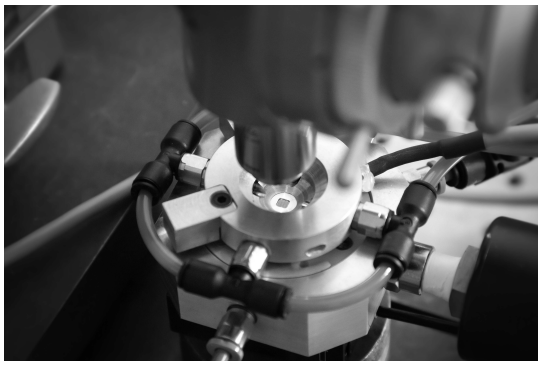

(c)

(d)

Figure 3.5: Pictures of the custom-made pressure cell: (a) The sample (grid with a polymer film on top) on top of the teflon holder; (b) An aluminum holder placed on top of the sample for fixation of the sample. The objective with a green light beam is visible on the top of the picture; (c) Final look of the cell with an upper part of the cell with four holes for a humidity delivery. The humidity detector is a black wire connected to the cell in the right of the picture; (b) Pressure detector, which shows the value of the pressure input inside the cell. The cell itself is located in the back of the detector.

The hole inside the upper part of the cell was made to fit around the objective of the interference microscope.

3.2.2 Pressure, temperature, humidity regulation

The set-up contains controllers and detectors for pressure, temperature of the experiment and humidity:

- **Pressure** was provided by the manually controlled flow of the nitrogen gas from

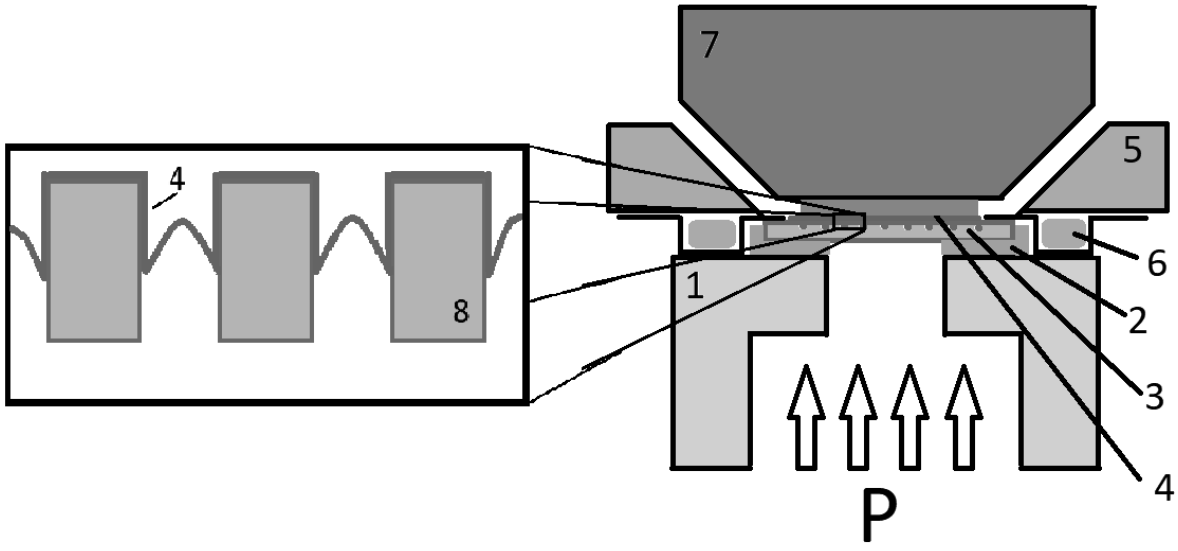

Figure 3.6: Schematic diagram of the experimental cell cross section: (1) Teflon stand with a hole for a pressure input; (2) adhesive tab to ensure no leaks and fixating of the sample; (3) grid with holes; (4) ultrathin polymer film; (5) aluminum holder; (6) Peltier ring; (7) objective of interference microscope; (8) Si_3N_4 grid membrane with holes.

the bottom of the sample. The set-up consists of a manually controlled valve (Festo LRP-1/4-2,5) to open and regulate the nitrogen flow and control the pressure, and a pressure detector at the input to the cell, where the sample is placed (Fig.7.1d). To avoid errors in pressure readings due to the loss in pressure as the gas goes through the system before reaching the sample, the pressure value was taken from the detector, not from the controller. The range of possible pressure inputs is set to be 0 - 1.6 ± 0.025 atm (0 - 0.16 MPa).

- A Peltier ring (Laird Technologies 71063-505) was used as the heating element to reach and regulate the required **temperature** for the experiment. The temperature detector (thermocouple) near to the sample provides feedback to the control system, so as to be able to regulate the temperature automatically using a computer interface (Laird Technologies SC interface software) once it reaches the required value. The temperature control system allows fluctuations of temperature of ±1°C. To obtain the equilibrium of temperature during the experiment, the sample is left at the required temperature for 1h before the start of the experiment.

- **Humidity** regulation is provided by a nitrogen flow moisturized with pure water. This is coupled with a humidity detector to keep the humidity level stable automatically. In order to keep the sample at the required temperature, the water is heated

to the temperature of the experiment. To avoid the loss of heat during transportation of the moisturized nitrogen to the sample, the tube for the flow is also heated to T_{exp} + 10°C. The influence of the moisturized nitrogen flow on the temperature of the sample is regulated by a temperature control system, so that the temperature of the sample can be set to the required experimental temperature value. To obtain the equilibrium of humidity and temperature during the experiment, the sample is left at the required humidity for 1 h before the start of the experiment. During operation, it was noticed that the humidity could fluctuate over time due to a leak of pressure from the cell, which depends on the attachment of the sample to the cell. But after minute of applying the pressure, the system compensate these humidity fluctuations.

3.2.3 Leitz- Linnik interferomic microscope

To obtain interference fringes on the image of the bubbles, a Leitz-Linnik interferometer was used, custom automated by the IPP team and use for many years for measuring the surface roughness of samples.

The system consist of two arms, which contains two identical ×50 (NA = 0.85) objectives and built in a Leitz-Linnik interferometer configuration (Fig. 3.7a). One arm contains the reference mirror, which provides a reference signal of a reflected beam. The beam from the reflection from the sample interferes with the reference signal, creating the fringes (Fig.3.7b).

A quasi-monochromatic green light source with λ = 540 nm is provide by an LED. The cell is placed on top of a piezoelectric nanopositioner (PI PIFOC), which provides the controlled scanning of the fringes over the z-direction. The images are obtained with a color CMOS camera (Photon Focus) mounted on the microscope, with a Giga Ethernet connection to the PC. The measurements are controlled by a personal computer equipped with custom developed LabVIEW based software (National Instrument, ver. 2014, 64 bits) combined with the IMAQ Vision module. The improved version of the software allows acquisition and saving of the data in only a few seconds. The full schematic layout of the Leitz-Linnik interference microscope is presented in Fig.3.7c, [71]. The technique for measuring surface shape is given below.

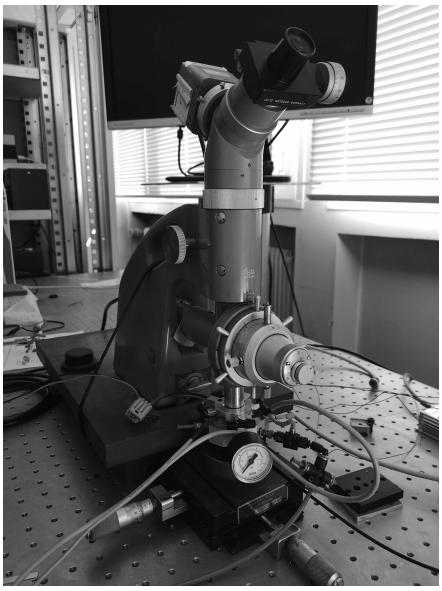

(a)

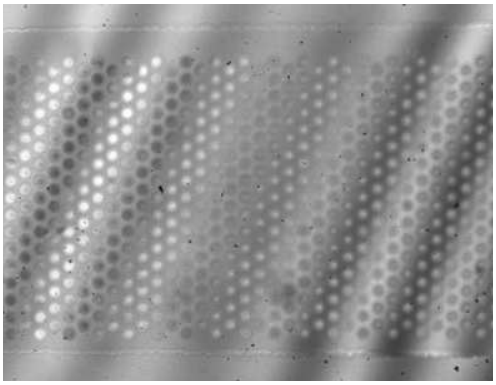

(b)

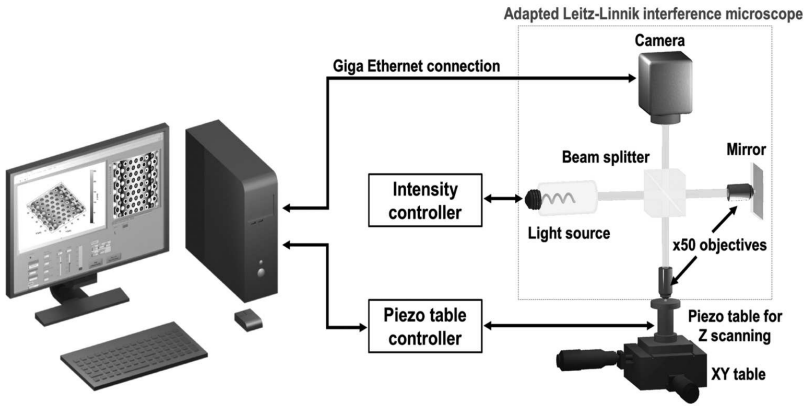

(c)

Figure 3.7: (a) The Leitz-Linnik interferomic microscope coupled with a pressure cell and camera; (b) The picture of real fringes before processing. The two sets of fringes corresponds to the reflections from the Si_3N_4 membrane and from the oxide layer on top of the membrane, which reported by manufacturer to be ~ 1 μm. The first set of fringes was used for the analysis of experiment as only by this fringes the focus on the polymer film inside the film is possible; (c) The schematic layout of the Leitz-Linnik interference microscope [71].

3.3 Microbubble inflation method

After the annealing process, the polymer film is attached to the grid. By applying pressure below the film, since it is fixed by adhesion to the inside of the circular edge of the grid hole with, which has a diameter of 5 μm, the polymer film inflates into bubble. In this method, it is the radius of the bubble curvature that gives information about the

mechanical properties of the film. By measuring the radius of curvature, the biaxial creep compliance can be calculated through the strain and stress history. The creep compliance, D, is defined by the ratio between the strain and applied stress. As the strain increase with time under the constant stress, the creep compliance becomes a dynamic property for time-dependant experiments.

The radius of curvature R for small deflections (few hundred nm for 5 μm diameter of the film) is defined as:

$$R = 1/k, \tag{3.1}$$

where k is the curvature of the bubble, which can be fitted with a 2^{nd} order polynomial $z(x) = ax^2 + bx + c$:

$$k = \frac{|z''|}{(1 + z'^2)^{3/2}}, \tag{3.2}$$

where z', z'' is the first and second derivative of $z(x)$.

The biaxial stress σ_{11} and biaxial strain ϵ_{11} can then be calculated as:

$$\sigma_{11} = \sigma_{22} = \frac{PR}{2t_0} \tag{3.3}$$

and

$$\epsilon_{11} = \epsilon_{22} = \frac{Rsin^{-1}(\frac{R_0}{R})}{R_0} - 1, \tag{3.4}$$

where P - the pressure, t_0 - polymer film thickness, R_0 - the hole radius and R - the radius of curvature [44].

As the radius of curvature of the bubble changes with time as the bubble grows, the stress and strain history has to be taken onto account to calculate the apparent creep compliance [29, 72]:

$$D_{app}(t) = \frac{\epsilon_{11}(t)}{\sigma_{11}(t)} \tag{3.5}$$

where $\epsilon_{11}(t)$ - time-dependent biaxial strain, $\sigma(t)_{11}$ - the time-dependent biaxial stress.

The data obtained at each timestep for stress and strain using Eq.3.3 and Eq.3.4 is fitted by the modified Kohlrausch-Williams-Watts (KWW) function [29, 68]:

$$\sigma(t) = \sigma_0 + \sigma_1 \exp\left[-\left(\frac{t}{\tau}\right)^{\beta_\sigma} \right] \tag{3.6}$$

and

$$\epsilon(t) = \epsilon_0 + \epsilon_1 \left(1 - \exp\left[-\left(\frac{t}{\tau}\right)^{\beta_\epsilon} \right] \right), \tag{3.7}$$

where σ_0, σ_1, ϵ_0 and ϵ_1 are fitting parameters, τ - retardation time, β_σ and β_ϵ - shape parameters for the stress and strain curves, respectively.

Therefore, the apparent creep compliance is determined from Eq.3.5.

3.4 Interference microscopy: Phase Shifting Microscopy

To measure the bubble growth over time, the Leitz-Linnik interference microscope (Fig.3.9) was used with the Phase Shifting Microscopy (PSM) technique to quantify the fringes and surface shape [73]. The use of monochromatic illumination allows the measurement of small roughness and structures of the samples, which is the case of ultrathin bubble inflation [74]. The Leitz-Linnik interferometer is adjusted to produce high contrast fringes superimposed on the surface of the film by modifying the path length difference between the two arms to match the coherence planes [73].

Making a single measurement of a static surface is now well controlled, resulting in a high axial sensitivity of a nm or better, as well as a high accuracy when correctly calibrated. But, the technique has certain limits, for example, in the axial measurement range for measuring step heights which is limited to $\lambda/2$ due to the 2π phase discontinuities. On a smooth surface, these discontinuties can be removed ("phase unwrapping"), but not for an unknown step height ([68]). Measuring nanometric shape of a slightly changing surface over a period of a few hours, as in the case of the bubble inflation technique, leads to additional difficulties.

3.4.1 Deformation of the grid due to the pressure

The main difficulty comes from the fact that while the aim is to measure the local change in nanometric shape of the bubble, the fringes move due to deformation of the Si_3N_4 membrane of the grid (150 μm $\times$ 3 mm) under pressure, resulting in a cylindrical shape and presence of several discontinuities (Fig.3.8,[68]). A solution developed with the first

propotype to avoid the phase discontinuities of the deformed grid surface is to align the fringes parallel to the band of holes by tilting the reference mirror(Fig.3.9b) and only to take the central holes into account for analysis, where the deformation of the grid is at a minimum and can be neglected. Fig.3.9a shows the fringes aligned parallel to the grid's bending axis before applying the pressure.

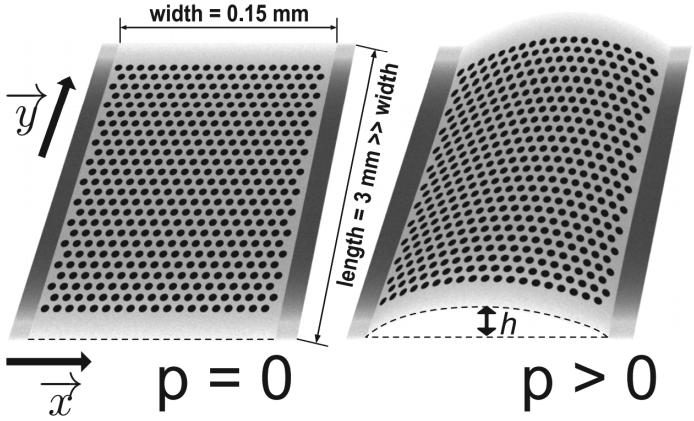

Figure 3.8: Illustration of the deformation of the grid membrane under pressure, where the h is the maximum height of the deformation, noted to be ~ 1.6 μm at 50 kPa pressure [68].

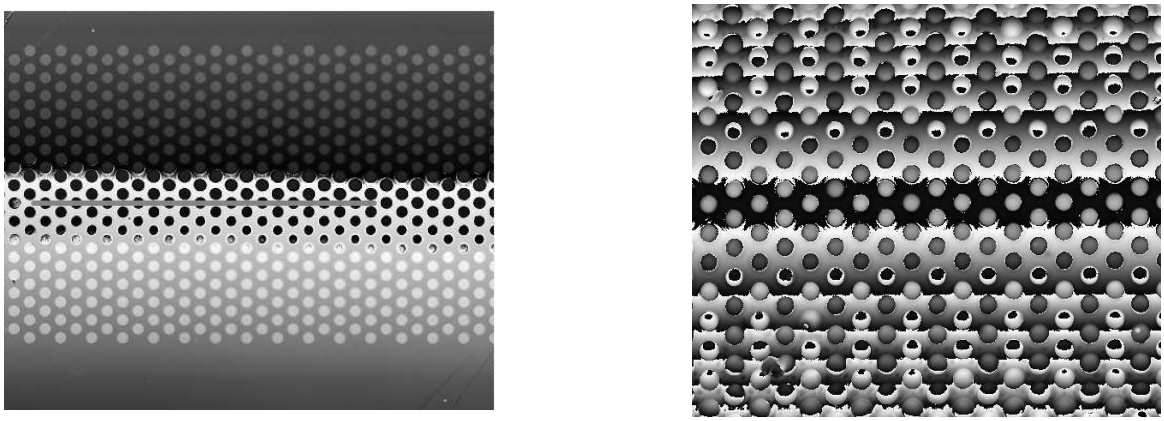

(a) (b)

Figure 3.9: The calculated surface height showing that the interference fringes on the membrane were aligned along the y-direction of the holes in the grid: (a) before the deformation of the membrane due to the pressure; (b) after applying a pressure of 70 kPa. The phase discontinuities are visible as jumps in the intensity, especially on the sides of the holes in the central part of the grid.

3.4.2 Depth profile determination

The PSM technique consists of calculating the depth profile of the sample surface from the phase ϕ as a dependence on the intensity at each pixel (x, y) in the interference fringe image. The algorithm for determining $\phi(x, y)$ uses the intensity data in the 5 images corresponding to the 5 phase-steps produced by moving the piezoelectric stepper, and measuring at each step ϕ=$\pi/2$ over a total phase of 2π [68]:

$$\phi(x,y) = arctan\left[\frac{2(I_2(x,y) - I_4(x,y))}{2I_3(x,y) - I_5(x,y) - I_1(x,y)}\right]. \tag{3.8}$$

The phase discontinuities in Fig.3.9b appear due to the periodicity of the fringes and the 2π jumps of the arctan function. The control of the piezoelectric table with the software of the interferometer allows moving the sample over the z-direction to obtain the position of the fringes in-between phase jumps. Due to the fast deformation of the grid during the first seconds after applying the pressure, refocusing and adjustment of the piezoelectric table is required and can be difficult, resulting in phase jumps. The same effect appears due to the inflation of the bubble above the height of $\lambda/2$. In this case the phase jump is corrected manually during the data analysis (see more in Section 3.5). The height of the surface $z(x, y)$ is defined as:

$$z(x,y) = \frac{\phi(x,y)\lambda_{eff}}{4\pi}, \tag{3.9}$$

where λ_{eff} is the effective wavelength that is larger than λ due to the wide numerical aperture (NA=0.85) and determined by the spacing between the fringes [68].

3.4.3 Data collection

The whole procedure of refocusing in the first few minutes after the pressure is applied takes $\sim$ 10-30 seconds, and the first calculated height image in 1 min (the 5 phase-step procedure takes $\sim$5 seconds). Saving the calculated image then takes $\sim$ 1 second. Nonetheless, since the risk of extra phase jumps appearing in the image during the first minutes of the experiment is high, the data collection can be slowed down so as to be able to adjust the piezo-electric position. After the grid deformation is stabilized, the refocusing of the microscope is rarely required and the collection of the data can proceed using automatic piezoelectric table regulation with the software of the system.

To improve the statistics of the measurement and to avoid random mistakes in the results, the data is collected for 10-15 holes along one central row and averaged as indicated by the green line in Fig.3.9a. A typical profile of the data along such line is presented in Fig.3.10.

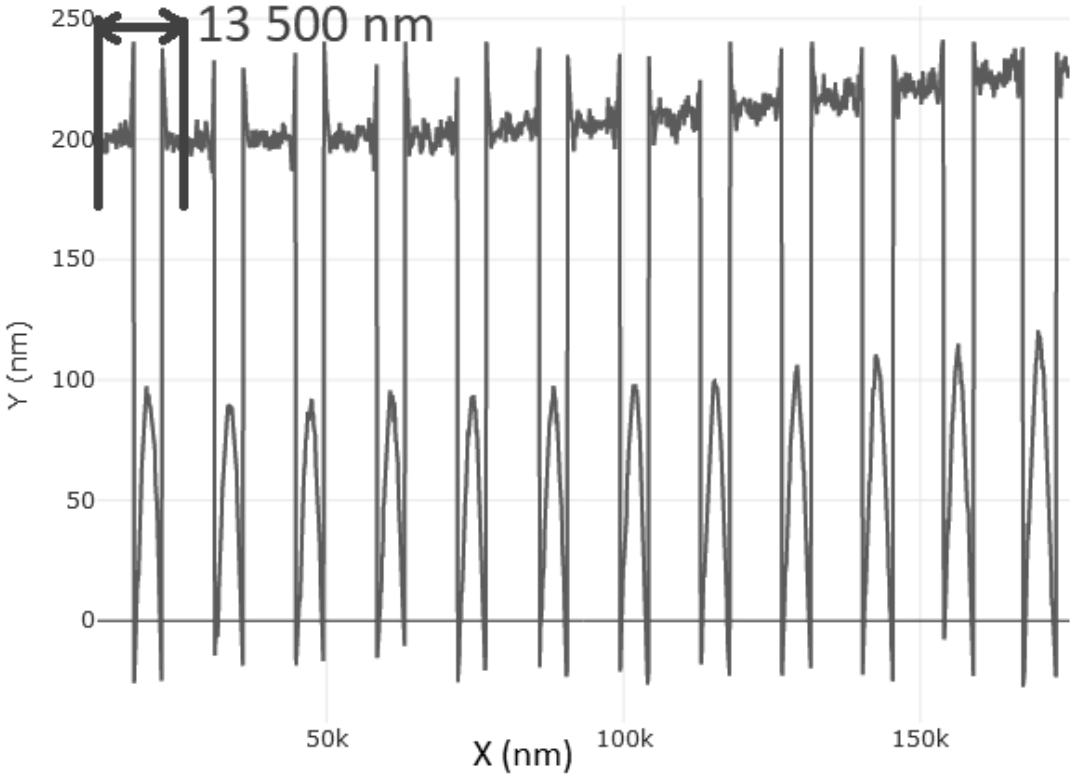

Figure 3.10: A typical sample of a line profile collected from the data of 12 holes after 11 minutes from the start of applying the pressure. The substrate level is set to the y=200 nm value. The drift of the substrate is caused by the position of the grid not being fully flat during fixing. The periodicity of the hole is around 13 500 nm, which corresponds to the size of the hole plus half of the gap between holes) and presented in blue.

3.5 Analysis of bubble shape

The collected data is saved in the .txt files (one file per time point) with two columns containing the x and z values of the bubble's profile. The file contains the data of all of the holes along the line together. The program for the automatic analysis was written by the author in R programming language [75]. The first step of the analysis is to separate the bubbles for each time point, which can be obtained from the periodicity of the hole position in the grids. The x-value of the data corresponds to steps of 0.115 nm (the size of the pixel), and the cutting period is set to be around 13 500 nm (which corresponds to

the hole plus half of the gap between holes) and presented in Fig.3.10. Finally, the data is saved in separate tables for each hole at each time point for further analysis.

The cross-correlation technique [76] was applied to each table to determine the center of each bubble x_c. Then, all the holes at a given time point were aligned along the x axis, so that the centers of symmetry matched. The alignment along z axis was performed by matching the profiles of the film on the substrate.

After the alignment, all the z-coordinates of the bubble profile, that correspond to a given x-coordinate were averaged (Fig.3.11a).

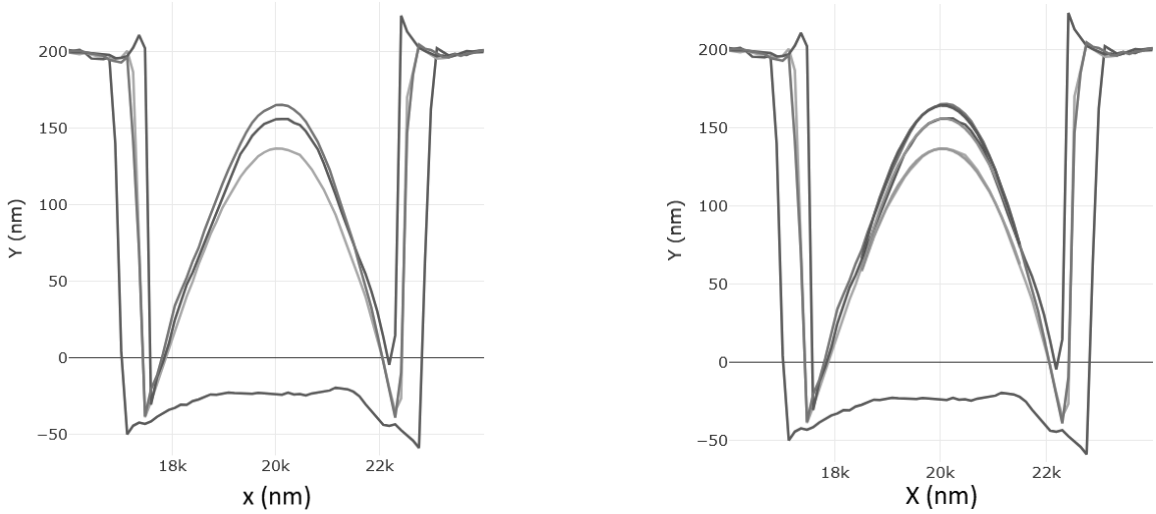

(a) (b)

Figure 3.11: (a) Averaged data for a few of the time steps during an experiment (0 min, 3 min, 38 min, 85 min in order of bubble height); (b) the data from (a) fitted with parabolic function Eq.3.10.

Following McKenna et al. [44], the fit of the bubble was chosen to be a parabolic function:

$$z(x) = Ax^2 + Bx + C, \tag{3.10}$$

where A, B, C are fitting parameters. The fit was applied to the region of $[x_c - 1.5\mu m; x_c + 1.5\mu m]$ (Fig.3.11b). The curvature at the point $x = x_c$ is then determined by Eq.3.2.

Sometimes, the parabolic fit does not follow the bubble shape. For example, in the case of bubble inflection, this is explained in detail below. In this case, we use a function given by Eq.3.11, which we refer to as the spherical function:

$$z(x) = A_0 \times R \times \left[1 - \left(x/R\right)^{\alpha}\right]^{1/\alpha} + A_1, \tag{3.11}$$

where A_0, R, A_1 and α are the fitting parameters. This function also gives information about the radius of curvature of the bubble - R, so that the stress and strain from Eq. 3.3, 3.4 can be found. The further analysis was based on the use of Eq. 3.5 - 3.7.

Chapter 4

Results and Analysis of Experiments

4.1 Introduction

The typical response of polymers to constant stress has three stages of creep: primary creep, which occurs after the elastic regime; secondary or steady-state, where the creep occurs; and tertiary creep which leads to the rupture of the sample due to damage inside the material (Fig.4.1, [79]).

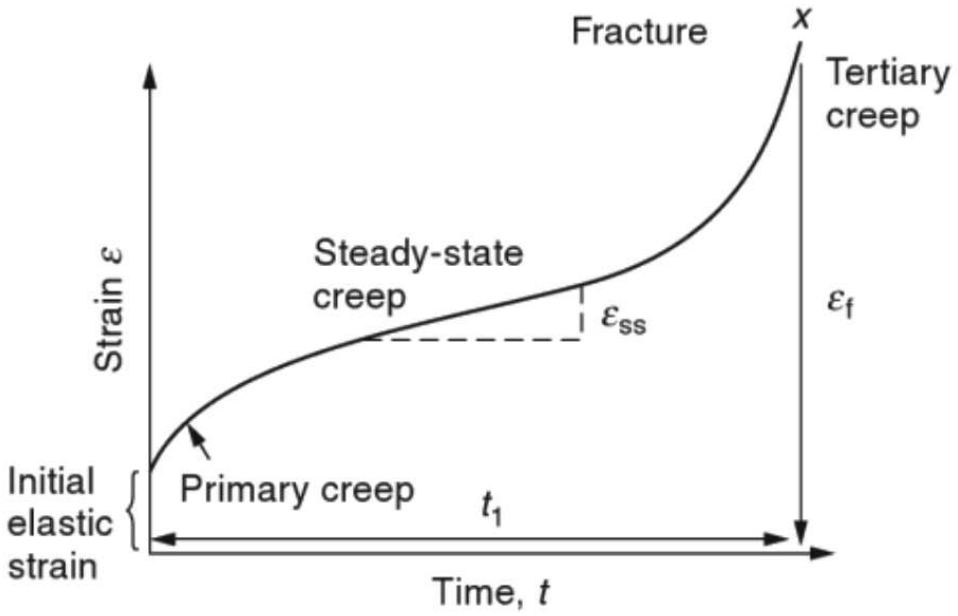

Figure 4.1: Typical creep curve of a viscoelastic material under constant stress [79]. The creep contains three stages: primary creep, secondary or steady-state, where the creep occurs, and tertiary creep which leads to the rupture of the sample due to damage inside the material.

In this work, experiments on the microbubble inflation of ultrathin polymer films resulting from these three mechanical behaviors of the polymer film are performed as a function of the temperature and pressure input. The description of these three behaviors and what happens after the pressure applied is now given.

All three behaviors (Fig.4.2) were observed in this work during experiments on both Polystyrene and Poly(vinyl acetate). The results on the bubble height evolution, the bubble shape, the viscoelastic properties and further analysis of the experiments for both, Polystyrene and Poly(vinyl acetate) are presented in this chapter.

1. **Elastic behavior**. The elastic behavior of the polymer film is present in every experiment and occurs from the beginning of the application of the pressure. As the re-focusing of the setup after applying the pressure and the single measurement of the bubble shape takes time, the first measurement is made at least around 1 minute after the start of applying the pressure. Due to this, the elastic regime that appears during the first moments of applying the pressure is not "catchable" with the present set-up, although, the later elastic behavior of the polymer film is observable. For some experiments the bubble remains at this level and does not evolve further.

2. **Creep of the bubble**. The bubble keeps growing during the whole time of the experiment. This corresponds to secondary (steady-state) creep.

3. **Inflection of the bubble**. The bubble shows a similarity to the creep behavior, but at a certain moment, the inflection points appear and the shape of the bubble changes. In this case, the bubble shape does not recover to the initial shape after the pressure is removed. This leads to the suggestion that the inflection could involve plastic deformation of the film.

The schematic visualisation of the three behaviors is presented in Fig.4.2.

In considering the three behaviors that appear, as described above and given in Fig.4.1, the primary creep is missed for our experiments as the manual re-focusing of the microscope and first measurements take a certain amount of time. The elastic behavior is therefore not visible since it happens during the first moments of the bubble growth. The tertiary creep is also missed with our experiments, as the bubble did not rupture for any of

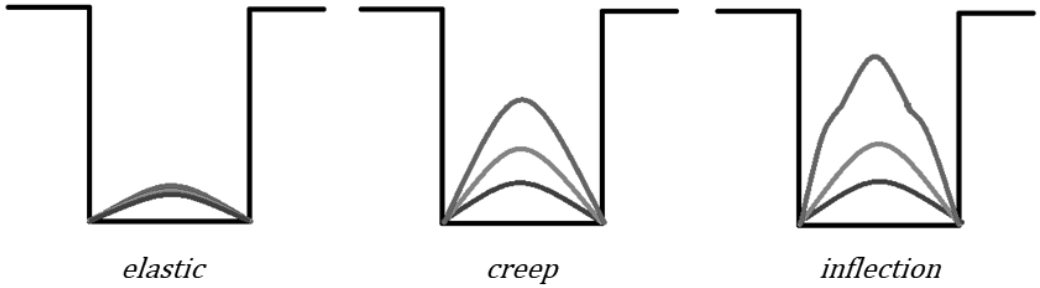

Figure 4.2: The schematic diagram of the three behaviors of polymer film and bubble growth with time under the applied pressure: elastic, creep and inflection.

the experiments we observed. But, the inflection of the bubble appears instead. The suggestion is that the polymer film overcomes the creep and deforms in a plastic-like regime. So, this case is also not a part of Fig.4.1 and only a creep behavior in our experiment can be considered as a secondary creep from Fig.4.1.

4.2 Polystyrene ultrathin films

4.2.1 Experimental conditions for Polystyrene films

As the goal of this work is to investigate ultrathin polymer films, the thickness of interest for PS polymer films was chosen to be 30 nm (the concentration of the polymer - toluene solution is fixed and equal to 0.7%). This thickness was achieved by updating the protocol of the sample preparation to lower the concentrations of the polymer - toluene solution. The temperature of the experiment is set to 63°C ($0.9T_g$) to be close to the glass transition region. The desired type of response (elastic, creep or inflection) is expected to be achieved by regulating the pressure input value (by test experiments, the pressure level range for this work was 0.2 - 0.7 atm). The pressure, higher than 0.7 atm, was not used in experiments as the pressure of 0.7 atm was found to meet the requirements of achieving creep behavior and inflection for some experiments. As the temperature of annealing is related to T_g in the same way as T_{exp} and both are constant for the majority of the experiments, in the end, the value of the applied pressure is the only adjustable parameter in the experiments.

4.2.2 Elastic behavior

In this section, the response of the polymer film during the microbubble inflation experiment at which the bubble does not grow and stays at a certain level of bubble height is named elastic-like (the bubble height is at the same level as the first measurement during the first few minutes). This means that the bubble does not evolve to creep behavior.

The elastic-like behavior is expected to be achieved at a low pressure level. In this case, the stress from the pressure input that acts on the polymer film is not high enough to achieve the transition from elastic-like to creep of the film. Additionally, the creep of the bubble should be achieved at a higher pressure level compared to the elastic-like response. But, in the experiments the elastic-like behavior of the polymer film inflation was achieved at pressures within the range of 0.2-0.7 $\pm$ 0.025 atm during the experiments. Even at the highest pressure level (0.7 atm) the creep behavior is expected, but for some experiments the creep did not appear and the bubble did not grow for the whole duration of the experiment, staying at the same level as after the elastic behavior. This is the evidence that regulating the pressure level itself does not guarantee the switch between the elastic behavior to creep. Thus, one of the characteristics that has a strong dependence on the applied pressure level is the bubble height. This can be explained by the higher level of stress exerted on the film for higher pressure and bigger deformation of the film (Fig.4.3).

The mean strain and mean stress was determined for the experiments for different pressure level (0.2, 0.5 and 0.7 atm) that showed elastic-like behavior and are presented in Fig.4.3d. The error bars indicate standard deviation. The last point with large error bars indicates the experiment with a high pressure level and corresponds to Fig.4.3c. This experiment represents the transition between the elastic-like behavior and creep, as the bubble shows small bubble evolution in time compared to lower pressures. Each curve at Fig.4.3a-4.3c corresponds to data on the bubble shape collected at each time step. The time steps for each experiment are unique due to the re-focusing of the microscope. Also, over the first 30 minutes, the data was collected every 1-3 minutes to have better statistics and information on the bubble growth evolution. After 30 minutes, the data was collected less frequently, one measurement per 5-10 minutes. Usually, this is enough to obtain the evolution of the bubble growth and for the overall experiment of 3 hours there are 40-70 bubble shapes collected. In these graphs all the time steps are shown together for easier visualization of the low bubble evolution over time. As was mentioned before, the data

on the bubble shape is averaged for 10-15 holes for each experiment to avoid occasional bubble growth. The center of the bubble is then determined and placed at the point $x = 20\ \mu m$, and in a similar manner, the substrate membrane is placed at the point $y = 200\ nm$. To estimate the bubble height, the position of the polymer film at $t = 0$ is also averaged and presented in Fig.4.3 with the dashed line.

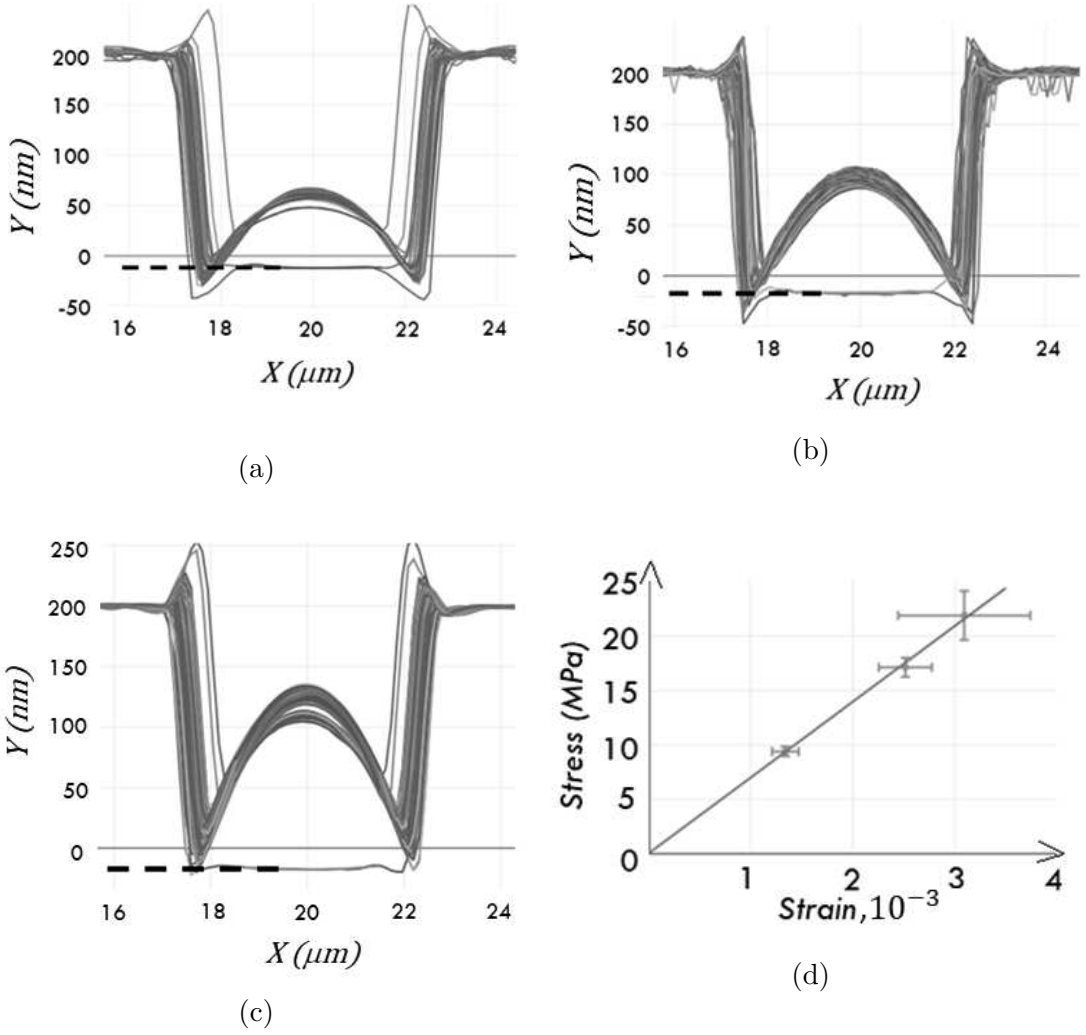

Figure 4.3: The elastic-like behavior during the microbubble inflation experiment. The bubble grows up to a certain height. Each line corresponds to one time step of the measured bubble's shape during the experiment. The horizontal dashed line corresponds to the position of the polymer film at t=0 before the pressure is applied. The overall time for the experiments was 180 minutes. Bubble growth over time at different pressure levels: (a) 0.2 ± 0.025 atm; (b) 0.5 ± 0.025 atm; (c) 0.7 ± 0.025 atm. (d) The mean strain and mean stress for three experiments presented in (a-c). The slope of the fitting curve, which is also the Young's modulus for the elastic response region is equal to 7 GPa.

The dependencies of the bubble height evolution with time for elastic-like behavior on different pressure levels are presented in Fig.4.4a. The bubble height was calculated as a

difference between the position of the bubble before the experiment (corresponding to the level of the dashed line) and the position of the bubble in the center of the bubble. Even this bubble height does not evolve much, the higher pressure leading to a higher bubble. So it can be noticed, that while the type of behavior of the polymer film does not have a strong dependency on the pressure level, the bubble height does.

As was mentioned before, in order to determine the mechanical properties of the polymer film, the strain and stress was extracted from the bubble curvature (see § 3.3). Obviously, the stress and strain values for the elastic-like regime are constant. Typical values of stress and strain in this regime are $\sigma = 1-2\times10^{7}$ Pa and $\epsilon = 1-3\times10^{-3}-10^{-2}$.

The slope of the fitting curve between three dots (corresponding to data from experiments with 0.2 atm, 0.5 atm and 0.7 atm pressure), which is also the Young's modulus for the elastic behavior region ($E = \sigma/\epsilon$), is equal to 7 GPa (Fig.4.3d), which is close to the reported value of the Young's modulus in literature of 5 GPa.

It is noticeable that increasing the pressure to 0.7 atm results in the crossover between the elastic-like and creep behavior (Fig.4.3c-Fig.4.4). The slight creep during this experiment enables not only the calculation of stress and strain from the experiment, but also the fitting of these values to give the time dependencies of stress and strain Eq.3.6-3.7:

$$\sigma(t) = \sigma_0 + \sigma_1 \exp\left[-\left(\frac{t}{\tau}\right)^{\beta_\sigma}\right] \tag{3.6}$$

and

$$\epsilon(t) = \epsilon_0 + \epsilon_1\left(1 - \exp\left[-\left(\frac{t}{\tau}\right)^{\beta_\epsilon}\right]\right), \tag{3.7}$$

where σ_0, σ_1, ϵ_0 and ϵ_1 are fitting parameters, τ - retardation time, β_σ and β_ϵ - shape parameters for the stress and strain curves, respectively.

The time dependencies give a history of the information of the values of strain and stress from the beginning of applying the pressure. In Fig.4.4b the data on strain and stress is presented only for the time range of the experimental data. But, in the end, the time dependencies are saved for a range of times 10^1-10^4, which corresponds to a range from 10 seconds to 10 000 seconds, which is close to 180 min for the experiment.

The results of these fits are presented in Fig.4.4b as lines, while the dots are the raw data of stress and strain, determined from the radius of curvature of the bubble at each time step. As can be seen, the stress slowly relaxes, while the strain increases, which

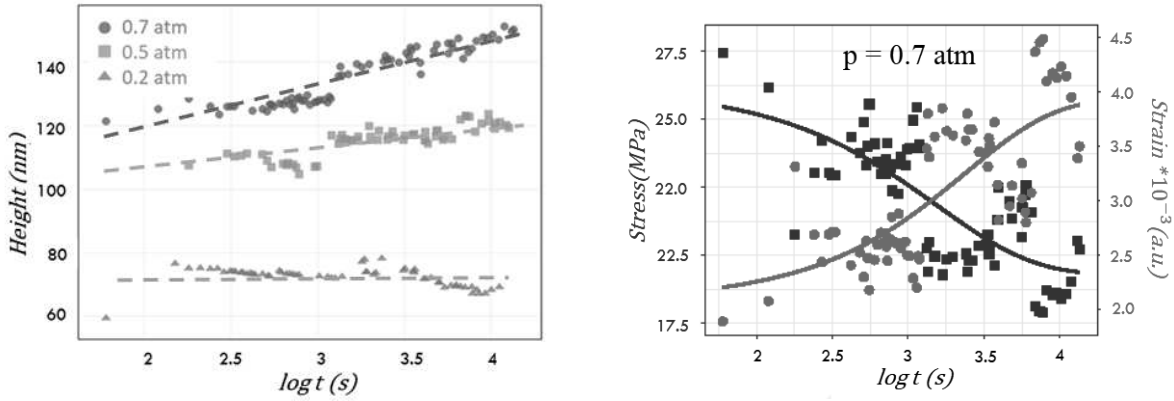

(a) (b)

Figure 4.4: The transition between elastic and creep response during the microbubble inflation experiment. (a) The comparison of the bubble height from Fig.4.3 for three pressure values: 0.2 (triangles), 0.5 (squares) and 0.7 (circles) atm; (b) The strain (circles) and stress (squares) curves based on the analysis of the data at 0.7 atm pressure from circles in (a) and fits using Eq.3.6-3.7.

corresponds to the creep behavior of the polymer film. The creep compliance D for this experiment was calculated from the stress and strain time-dependencies (see Eq.3.5) and is presented in Fig.4.5 in comparison with the creep compliance, calculated by McKenna et al.[29] for a similar polymer film.

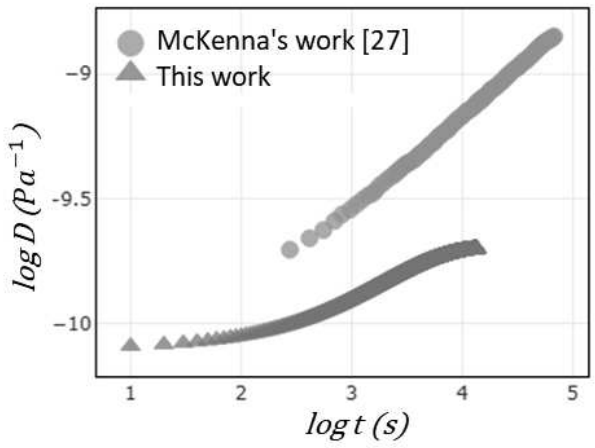

Figure 4.5: Creep compliance for the data from the experiment at 0.7 atm pressure presented in Fig.4.3c (triangles), calculated using Eq.3.5. The creep compliance presented in comparison to McKenna's work (circles) [29] for a 36 nm thick PS polymer film at T_{exp}=69°C ($\sim 0.96T_g$) and 0.14 atm pressure. The sample of McKenna et al. was annealed at 10-15°C over T_g. The slopes of the curves corresponds to viscoelastic behavior of the polymer film.

The values of creep compliances differ due to the different experimental and annealing temperatures compared to T_g: for this work, the experimental temperature is set to $0.9T_g$, whereas in McKenna's work it was $0.96T_g$. The annealing temperature for this work was 10°C over T_g, while for McKenna's work it was 10-15°C. The higher annealing temperature leads to higher relaxation of the internal stresses inside the film, so both of the higher temperatures in McKenna's work lead to higher mobility of chains inside the confined

film, so that the creep of the polymer film would proceed faster, also leading to higher values of creep compliance. The lower value of temperature used in this work also explains reaching faster the rubbery plateau of the polymer film.

4.2.3 Creep behavior

As was mentioned before, the change in the behavior type was expected to be regulated through the change of the pressure input value (with an exception existing for the elastic-like behavior at 0.7 atm pressure level, described in § 4.2.2). The creep of the ultrathin polymer film was observed for the pressure of 0.5-0.7 ± 0.025 atm. Values of pressure higher than 0.7 atm were not used, as at a pressure of 0.7 atm, the inflection of the film and the overcoming of the creep was achieved for some experiments. This indicates the limit of the convenient pressure to achieve the creep of the film. The visualisation of the bubble's creep over 3 hours of experiment is presented in Fig.4.6. Each curve represents the bubble shape at each timestep, when the data was collected. As can be seen, firstly the bubble stays at the same height for some time, and only then the creep occurs.

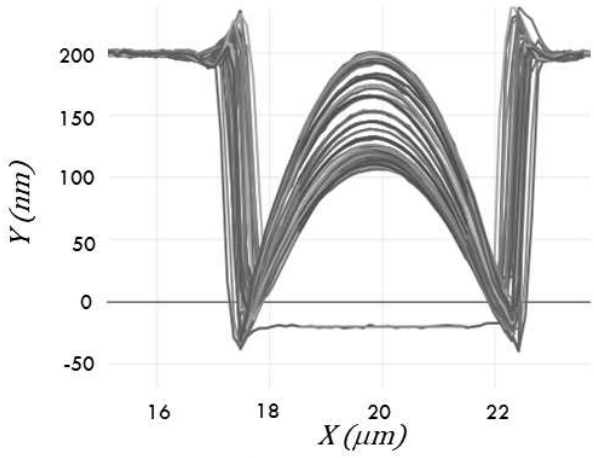

Figure 4.6: The evolution of the bubble height with time. The experiments were performed for 180 minutes at 0.7 atm pressure and a temperature of T_{exp}=63°C. The growth of the bubble is visible over the whole of the 180 minutes of experiment.

The difference between the elastic and creep regimes of the bubble growth is visible from the bubble height evolution with time (Fig.4.7). The height dependencies were fitted with a power law:

$$h(t) = B_0 \times (t^{\alpha}) + h_0, \tag{4.1}$$

where B_0, α, h_0 are fitting parameters. The table of fitting parameters presented in Fig.4.7b.

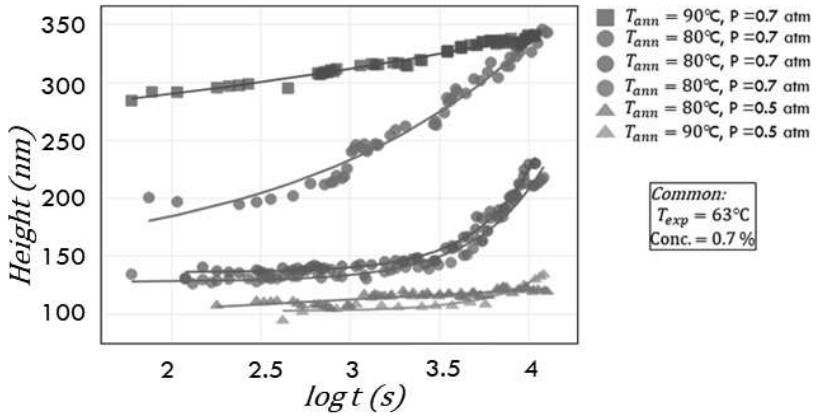

(a)

	B_0	α	h_0
■	43.169	0.113	217.558
●	10.616	0.316	138.923
●	0.000437	1.327	136.037
●	0.002344	1.134	127.805
▲	67.474	0.040	23.061
▲	6.89e-05	1.387	102.439

(b)

Figure 4.7: (a) The comparison of the bubble height evolution for several experiments: data indicated by circles had the same conditions of preparation, annealing and experiment. The data in violet corresponds to the data from Fig.4.6. The triangles presents data at the same pressure level of 0.5 atm with only a difference in the annealing temperature of 80°C (green) and 90°C (orange). The squares represent data from the experiment with a higher annealing temperature 90°C and the highest pressure of 0.7 atm. The data was fitted with power law Eq.4.1; (b) The parameters of fit with a power law.

Fig.4.7 presents the data of the bubble height for elastic-like (triangles) and creep (circles and squares) behavior. The difference between data in circles, which corresponds to three identical experiments, proves the sensitivity of the sample to the preparation conditions and the experiment itself. Even though creep occurs in all three experiments, the bubble height differs by an order of two. Also, in Fig.4.7 the data in brown squares and data with the orange triangles presents the experiments with a higher temperature of annealing (T_g + 20°C). From one of point of view, the difference in annealing temperature of only 10°C shows the difference in bubble height (for the same pressure level of 0.7 atm), twice as big compared to that at the lower annealing temperature. But, from another point of view, for the same higher annealing temperature of 90°C, two pressures of 0.5 atm and 0.7 atm shows a three times the difference in bubble height. From this figure it can be seen how just a small change in either pressure or the annealing temperature can result in such widely varying outcomes. This was one of the reasons why finally, the range of the pressures used was chosen only with three values: 0.2, 0.5 and 0.7 atm, and why the annealing temperature was chosen to be the same in the majority of the experiments.

The creep compliances that correspond to the height data in Fig.4.7 are presented in Fig.4.8.

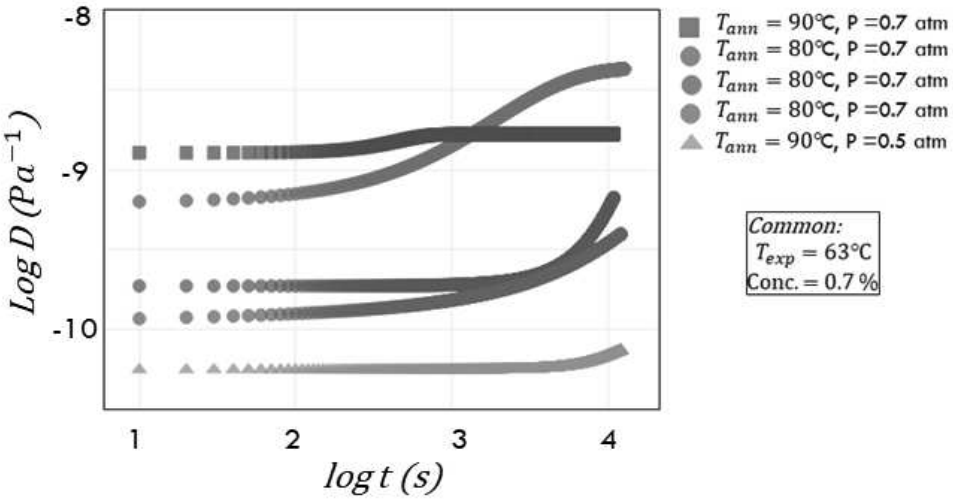

Figure 4.8: The creep compliances for the data presented in Fig.4.7 using the same color correspondences.

The existence of a slope in the creep compliance curve corresponds to creep in the polymer film and growth in strain with a decrease in the stress of the film. When the stress from the pressure is not enough to overcome the balance of stresses in the inflated film, the creep compliance curve will show at constant value, which is also called the rubbery plateau. As can be seen in Fig.4.8, the change in slope of the creep compliance curves correlates to a point when the bubble starts to grow intensively, which can be seen in Fig.4.7.

A difference in the data points can be noticed on the time axis for the height and creep compliance plots. The point to note is that the data of the height of the bubble at each time step is based on raw data of the bubble shape. At the times the measurements were performed, the same time data points are given for the height plot. Meanwhile, the creep compliance is calculated from the time dependencies of the stress and strain, which in turn was found by fitting the raw data of stress and strain from the bubble curvature. As we use the fitted curves as the values of stress and strain, we can continue these curves close to 0. As at zero both strain and stress are zero, the first point of time was chosen to be $logt = 1$, which is 10 seconds. Each next point presented in the creep compliance plot is equal to plus 10 seconds to the previous point. Such a way of presenting the data gives the possibility of providing a history of the creep compliance and not losing the data during the first moments of the measurement.

4.2.4 Inflection of the bubble: threshold

Along with the creep of the bubble, the behavior of the bubble inflection was observed. The visualisation of the bubble shape during bubble inflation is presented in Fig.4.9. The inflection of the bubble does not appear from the beginning of the experiment. For all cases of the bubble inflection appearance, the experiment started in the same way as for the creep experiment, with the inflection of the bubble appearing after a certain time. For the PS films, this time is close to 1 hour after the start of the experiment. Unfortunately, the inflection of the bubble can only be seen during the analysis of the bubble shape. During the experiment, there is no way of knowing beforehand if the bubble shows only the creep behavior or inflections.

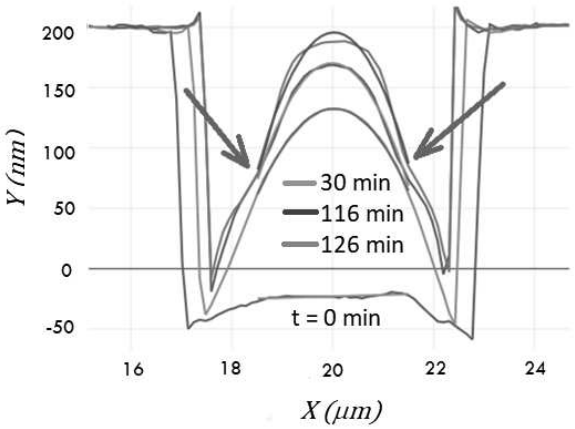

Figure 4.9: The inflection of the bubble shape during the experiment with the standard conditions. The inflection region is presented by red arrows. The temperature of the experiment was set to T_{exp}=63°C, the pressure value p=0.7 atm, and the annealing temperature was set to T_{ann}=80°C. The change in the bubble shape started after $\sim$ 60 minutes after the start of the pressure input. The fitting of the bubble shape does not longer follows the bubble shape.

As the fitting of the bubble shape is no longer valid (the fit with a parabolic function does not follow the bubble shape), there is no possibility of calculating subsequent the stress, strain and creep compliance during the inflection. The phenomenon of the bubble inflection and mechanism of it's appearance in the microbubble inflection experiment is unknown and requires further investigation. One assumption is that the polymer film overcomes the creep regime and starts to behave as in the plastic-like regime. Also, the polymer film may not be homogeneous on large scales, which may lead to necking of the polymer film at the inflection points. Still, the necking on such a nanoscale is not reachable for the setup used in this work. But, the question remains how the necking appears in the same region for all the experiments, where inflection takes place.

The evolution of the height values of the bubble in the case of inflection is scattered in comparison to the previous experiments shown before (creep and elastic-like), which

means that the bubble is less stable after inflection appears (Fig.4.10).

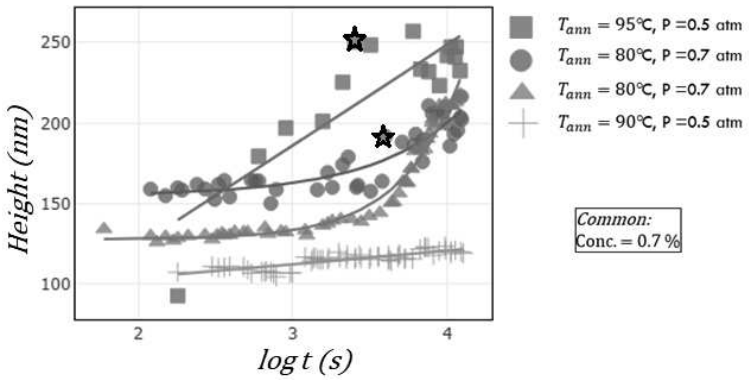

(a)

	B_0	α	h_0
■	3173.11	0.0081	-3168.827
●	0.041	0.761	155.001
▲	0.0023	1.1334	127.805
+	67.474	0.040	23.061

(b)

Figure 4.10: (a) The bubble height evolution for the inflection regime (squares and circles) is more scattered in comparison to the creep (triangles) and the elastic-like regime (crosses). The points with stars correspond to the first appearance of inflection in the bubble. The data was fitted with a power law Eq.4.1; (b) The table with fitting parameters of the data, presented in (a).

The scattering of the bubble height corresponds to the change in the bubble shape after the first inflection point in time. The bubble shape changes from visual inflection, which results in an increase in bubble height, when the inflection appears, but then changes to a wider, but lower bubble (Fig.4.11). Still, after the inflection points appear, the fit no longer follows the bubble shape.

Fig.4.11 shows the play of the bubble shape from higher, but thinner (126 min after start of experiment), to lower, but wider (for example, 173 min). The change in the bubble shape from one to another was observed during the whole of the time left for the experiment.

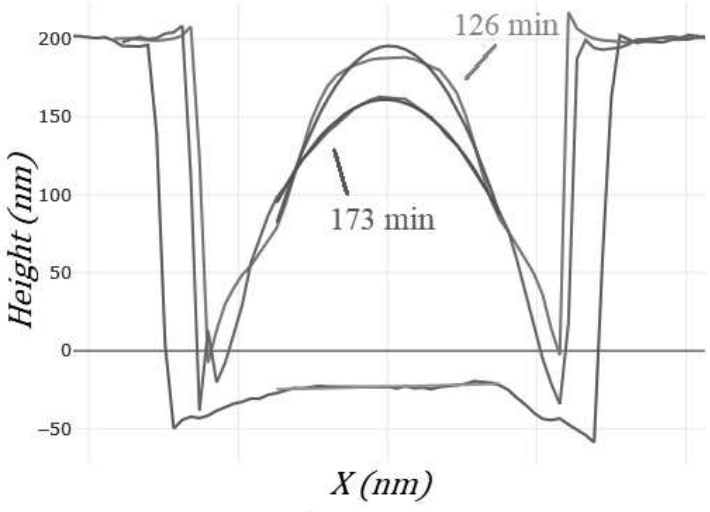

Figure 4.11: The change in bubble height and shape during the experiment with inflection of the bubble shape. The blue line (with orange fit) corresponds to t=0. The green line (with red parabolic fit) corresponds to the bubble shape at t=126 min after the applied pressure of 0.7 atm. The violet line (with brown parabolic fit) corresponds to t=173 min after the applied pressure.

4.2.5 Discussion

After the results on the PS polymer films, there are several points that have to be addressed due to the complexity of the experiment. The measurements of the sample's thickness were made with both ellipsometry and AFM on the polymer film on top of the silicon substrate after the film formation, while the polymer film in the experiment is freestanding. So the presence of the substrate can influence the thickness of the polymer film in the freestanding state.

Another point is that the glass temperature determination from the data of Dalnoki-Veress and Forrest [11] also becomes challenging. The T_g for a thickness of 30 nm corresponds to the range of 68-72°C. The test experiments showed the T_g = 70°C as an acceptable temperature to achieve the creep stage of the polymer film in this work. Concerning the thickness of the polymer film, during the annealing process, the film moves partially inside the hole of the grid due to the capillary process, which leads to a thinning of the film. According to McKenna et al [77], the pre-strain in the film that is induced due to this movement of the film into the hole can be approximately between 1% to 25%. This corresponds to $\lambda = 1.01$ to 1.25, which in turn leads to a reduction in the thickness by a factor of $1/\lambda^2$. For the "worst" case, when $\lambda = 1.25$, the new thickness is equal to 19 nm (30 nm originally). This means that T_g drops to $\sim$ 40°C according to the work by Dalnoki-Veress [11], which is lower than the T_g values used in this work by 44%. By following this assumption, such a drastic change in T_g for thinner polymer films would lead to the need to change all the characteristic of the experiments. What can be concluded is that the evolution in the film thickness during the bubble inflation can be assumed to have a trend towards thinning. In practice, this is challenging to measure. The rough geometrical estimation of the polymer film thickness on the 250-nm height bubble showed a reduction in the thickness of up to 40%. Such a reduction could lead to a decrease in T_g by as much as 30°C.

4.2.6 Conclusions

The microbubble inflation technique, coupled with interference microscopy, allows a measurements to be performed without contact with the polymer film. Optical analysis of

the bubble shape at each time step allows measurement of the evolution of the bubble growth over a scale of a few hundred nm and this information can be used to give the mechanical properties of the film.

The experiments on ultrathin Polystyrene films of 30 nm thickness were performed at different pressure levels. Depending on the pressure level, three behaviors of the polymer film were obtained. The **elastic-like** behavior, for which the bubble does not grow with time, stays at the same bubble height. For such a case, the mechanical properties such as stress and strain of the polymer film are constant. The bubble height shows a strong dependence on the pressure applied. The pressure level of 0.7 atm was found to be a convenient pressure to obtain the **creep** behavior. The constant growth of the bubble in this case allows the determination of the time dependencies of the strain, stress and creep compliance. The results on creep compliance are comparable with previous investigations on similar polymer films. In addition, for high levels of pressure, the **inflection** of the bubble shape appears. The fitting of the bubble with a parabolic fit is not possible for such a case since the shape of the bubble changes. The extraction of the mechanical properties in this case is not appropriate and cannot be quantified with the computation previously proposed. One assumption made is that the deflection of the bubble is so high that the polymer film overcomes the creep behavior and the bubble deforms in a plastic-like regime. This means that the polymer film overcomes the yield point and the polymer film does not recover its initial shape, when the pressure is removed. Also, the polymer film might not be homogeneous and inflection appears due to necking of the fragile regions, where the polymer film is at its most inhomogeneous.

The whole experiment involves many characteristics and conditions of sample preparation, together with a variety of experimental conditions. For example, the concentration of the polymer-toluene solution, the characteristics of the spin-coating procedure, the annealing temperature and duration, the temperature during the experiment, the age of the polymer film, and the temperature and humidity level of the environment near to the sample are just some of the characteristics, which have or might have an impact on the behavior of the polymer film. Due to such a diversity of possibilities, in this work we chose to limit the number of variables by only changing the pressure level for investigating the behavior of the polymer film in response pressure.

The project has many possibilities to investigate the influence of characteristics that

are described above. As the experiment is sensitive to each of these characteristics, the influence of each of them could be investigated by changing only one characteristic per experiment. Also, finding a different method for attaching the polymer film to the grid without annealing would also remove another major factor of influence on the results of the experiments. Finally, being able to measure the thickness of each sample would also reduce the error of the T_g estimation.

4.3 Poly(vynil acetate) ultrathin polymer films. Influence of humidity

For the PS polymer films the regime of the polymer film response was regulated by changing the pressure value. For the PVAc ultrathin films the regulation between the regimes occurs by changing the humidity level. As was mentioned before (see § 4.1), all three regimes were observed for the PVAc polymer films. The conditions of the experiment and sample preparation were the same for all of the samples (except humidity):

1. Concentration of the polymer solution in toluene was 2.6% w/w if not specified to the contrary (a few of the experiments were performed for 2.8% w/w concentration). Such concentrations were used to obtain ultrathin PVAc films of 100-120 nm thickness. The preparation of the polymer films with lower concentrations and lower thickness were not possible since such films simply dissolve in water. This phenomenon can be related to the critical amount of water that the polymer film can absorb. In this case, the protocol needs to be improved. In this work, the thickness of the PVAc films was 100-120 nm.

2. The annealing temperature was set to 40°C, which is equal to T_g+10°C.

3. The temperature during the experiment was set to T_{exp}=27°C, which corresponds to $0.9T_g$ to be close to the glass transition region, where the creep of the polymer film is reachable.

4. The pressure used for all experiments was set to p=0.25 ± 0.025 atm. Such pressure was found to be convenient to obtain creep behavior of the polymer film.

The humidity range in this work was set to 10-60 %. The lowest humidity of 10% can be considered as a low-humidity level. The highest humidity level that was used in this work is 60% since even for such humidity the bubble deflection was high and inflection for some experiments appeared. Therefore, higher than 60% humidity level was considered as being not relevant for this work. In this chapter the three regimes of polymer film response on the pressure input for different humidity levels are presented.

4.3.1 Elastic response range of PVAc

It is hard to say whether it is the humidity level that turns the creeping of the polymer film on or off. There is no strong dependence on the behavior of the polymer film at different humidity levels. But this certainly has an impact on the bubble height. One would expect that the elastic-like behavior would correspond to low humidity levels. But, for the PVAc films the elastic-like regime was observed for two humidity levels of 25% and 50% with a huge deflection of the bubble (Fig.4.12). The elastic-like behavior for PS corresponds to a low bubble height and an absence of the bubble evolution. But for the PVAc, the elastic-like behavior described here, differs from that of the PS. The huge deflection of the PVAc polymer film straight from the beginning of the experiment means that the polymer film might overcome the elastic response and creep of the bubble in the first moments of applying the pressure. Still, the evolution of the bubble is comparable to that of the PS film, where the change in the bubble height only varies by around 50 nm.

In Fig.4.12, the bubble deflection for both cases is greater than the bubble deflection for the majority of the experiments, which are presented below. One possible explanation is that the polymer film overcomes the creep behavior in the first moments of the experiment, so that the deflection is huge and the bubble no longer grows. The data in triangles represents the creep for a low humidity level of 10%, which proves the sensitivity of the experiment.

The elastic-like case is rare for experiments with PVAc, but still possible. The appearance of this case was not reproducible for other experiments, but the huge deflection of the bubble during the experiment was observed for high humidity level, which is presented below. The determination of the stress and strain curves for such an elastic-like response is difficult due to the non-uniform data on stress and strain obtained, so that the creep compliance calculation is also not possible for similar cases.

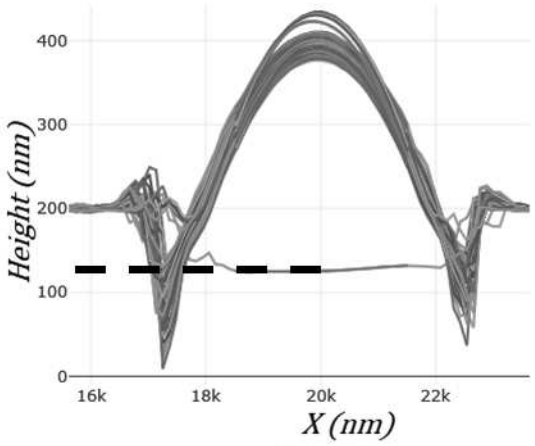

(a)

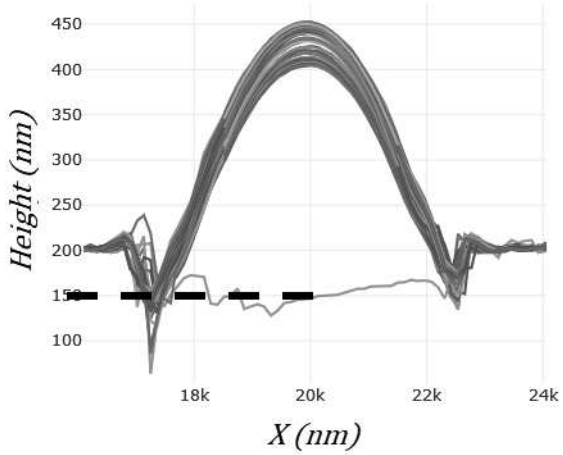

(b)

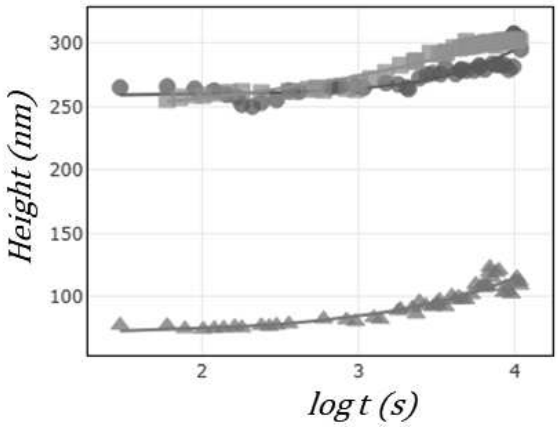

	B_0	α	h_0
■	7.208	0.249	233.847
●	0.013	0.860	259.064
▲	0.468	0.494	70.599

(c)

Figure 4.12: Experimental results of the bubble deflection in the elastic-like regime for two different humidity levels at the same pressure level of 0.25 atm and temperature of 27°C ($0.9T_g$). The dashed horizontal lines corresponds to the polymer film position at timestep t=0; (a) The humidity level of 50%. The first measured bubble shape was obtained at 30 seconds after applying the pressure. The bubble does not grow over time during the whole of the 3h of the experiment. The creep of the bubble starts only after 3h of the experiment; (b) The humidity level of 25%. The deflection of the bubble matches the previous data from (a); (c) The comparison of bubble height evolution of data from (a) in squares, (b) in circles to the bubble deflection for the experiment at low humidity level (10%) in triangles. The parameters of the fit of the bubble height are presented in table.

4.3.2 Creep of the PVAc as a function of humidity

The majority of the experiments on PVAc show that the creep of the polymer film for all the levels of humidity has a strong dependence of the deflection level on the humidity level during the creep behavior (Fig.4.13).

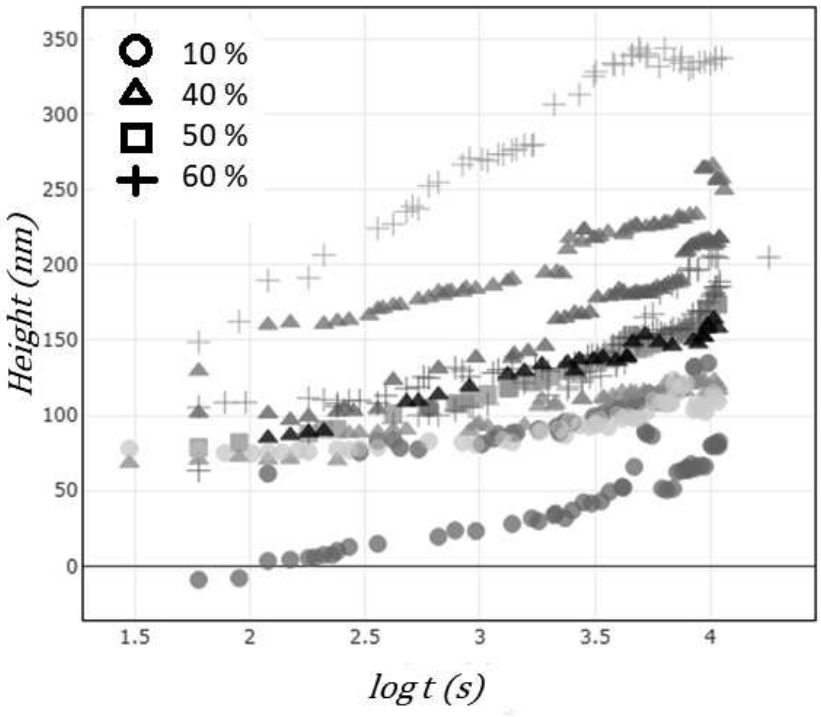

Figure 4.13: The dependence of the bubble deflection evolution over time of the experiment (180 minutes). Four different humidity levels presented in symbols: 10% in triangles, 40% in circles, 50% in squares, 60% in crosses.

For easier representation, the Fig.4.13 is presented below as a function of the humidity level per plot (Fig.4.14). The overall tendency shows that the bubble deflection becomes higher with an increase in the humidity level. The close deflection values for high humidity levels such as 40% and 60% could be explained the levels of the humidity being close to the critical humidity mass sorption by the polymer film.

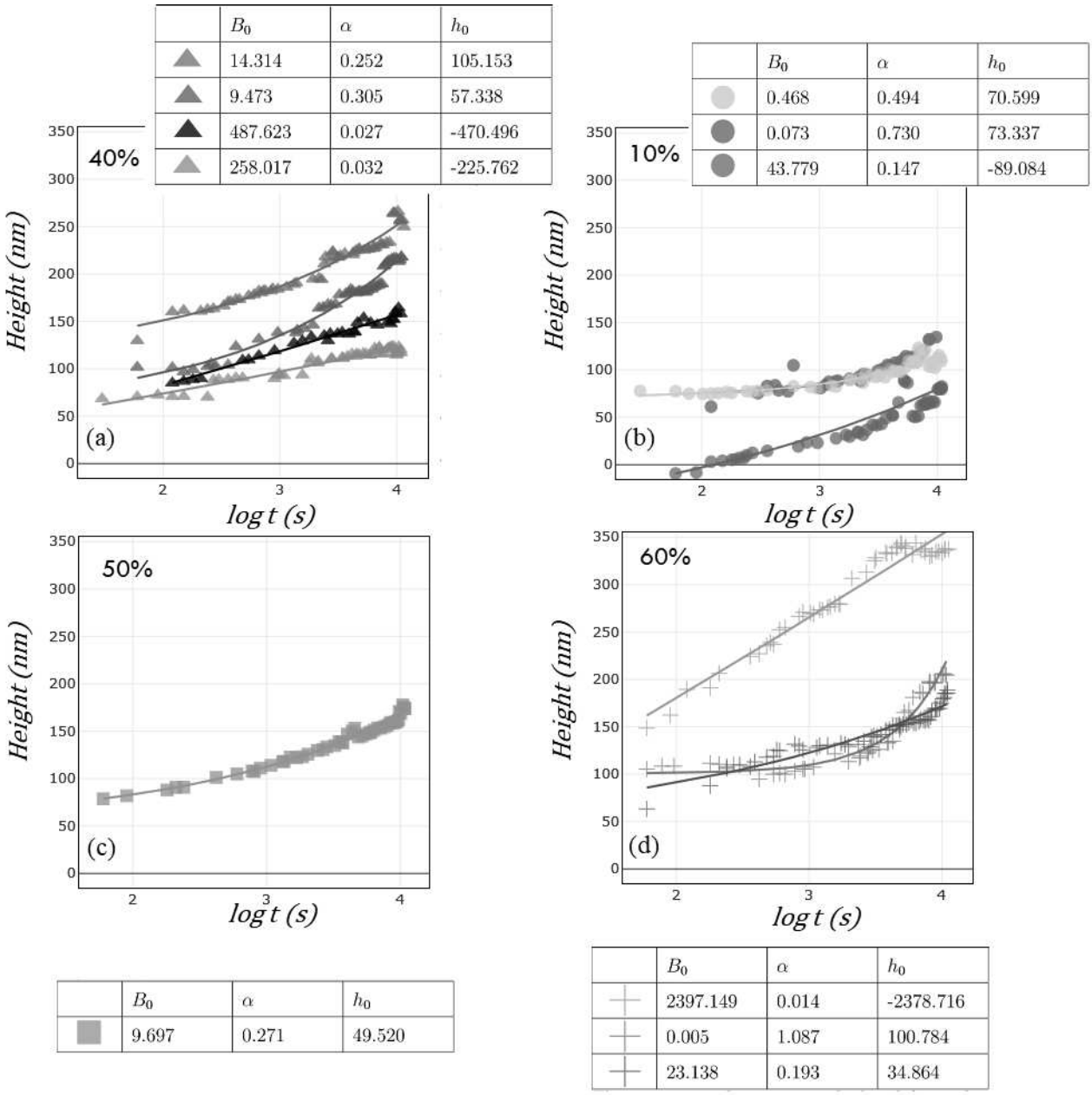

	B_0	α	h_0
▲	14.314	0.252	105.153
▲	9.473	0.305	57.338
▲	487.623	0.027	-470.496
▲	258.017	0.032	-225.762

	B_0	α	h_0
●	0.468	0.494	70.599
●	0.073	0.730	73.337
●	43.779	0.147	-89.084

	B_0	α	h_0
■	9.697	0.271	49.520

	B_0	α	h_0
+	2397.149	0.014	-2378.716
+	0.005	1.087	100.784
+	23.138	0.193	34.864

Figure 4.14: The bubble height evolution fitted with Eq.4.1 as a function of the humidity level: (a) 10%. The data represented in violet goes close to 0 because of the bad determination of the position of the film inside the hole at t=0 timestep. Still, the tendency of the bubble growth corresponds to the same data in green and red, but with a shift; (b) 40%. The black triangles correspond to the concentration of the polymer solution of 2.8% w/w and thickness of the polymer film of 120±5 nm; (c) 50%. The data for such humidity level presented in one sample only; (d) 60%. The blue data corresponds to the concentration of the polymer solution of 2.8% w/w and thickness of the polymer film of 120±5 nm.

From another point of view, the dependency of the bubble height for different humidity levels was obtained for mean values of bubble height for the data at the same humidity level from Fig.4.13. This was calculated for the data on the bubble height at three times of the experiment: 120 sec, 1000 sec and 10800 sec (Fig.4.15). The data for the humidity level of 50% is not taken into account since it exists only for one measurement. As can be seen from Fig.4.15, the overall tendency of a higher bubble height for higher humidity is proven.

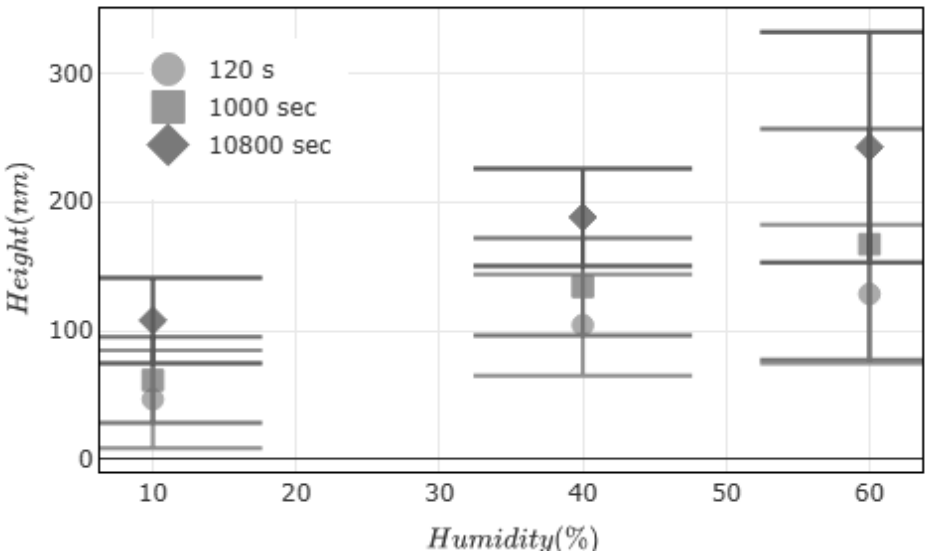

Figure 4.15: The mean values of bubble height at t = const depending on the humidity level: $t \sim 120$ sec in circles, $t \sim 1000$ sec in squares, $t \sim 10800$ sec in triangles. The error bars indicate standard deviation from averaging the data from Fig.4.13. The data at the humidity level of 50% is not taken into account since it exist only for one measurement.

Alongside the bubble height, the creep compliance was calculated for each experiment from Fig.4.14, keeping the same correspondence of colors (Fig.4.16). Even though the creep compliance is presented in 3-4 curves for the same humidity level, there is still a scatter of these curves and the averaging of the data for the same humidity level is inappropriate. Such a diversity of the creep compliance values and shapes for the same levels of humidity is one sign of the overall sensitivity of the experiment.

The slopes of creep compliance curves show the reaching of the rubbery plateau for the majority of experiments with a shift of these plateaus to later times for low humidity levels. From another point of view, this means that the polymer film reaches the creep behavior faster at higher humidity levels.

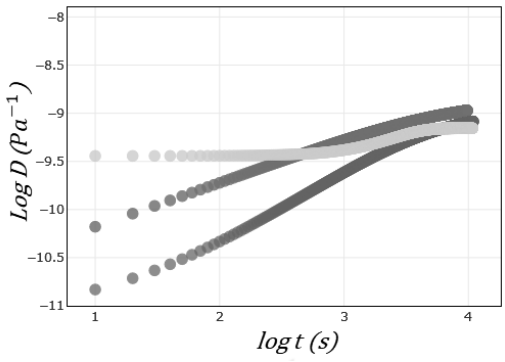

(a)

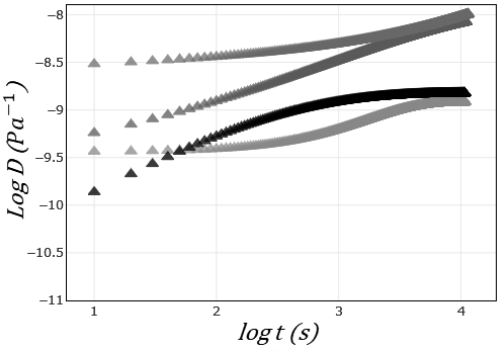

(b)

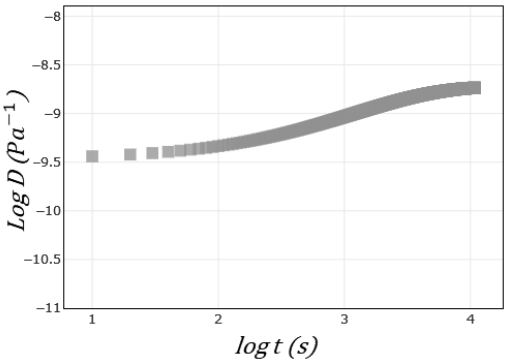

(c)

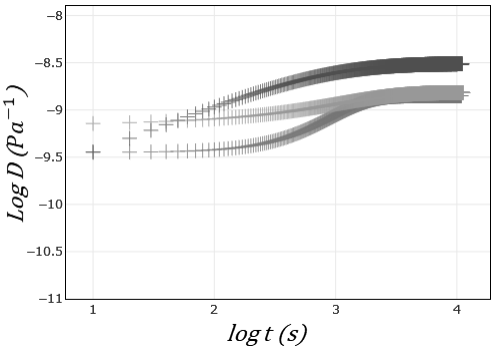

(d)

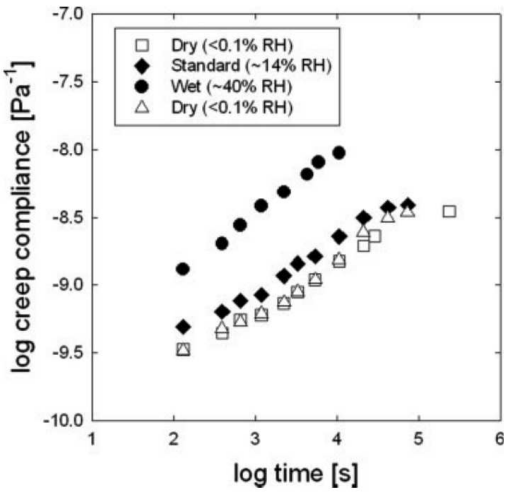

(e)

Figure 4.16: The creep compliance as a function of to the humidity level: (a) 10%; (b) 40%. The black triangles correspond to the concentration of the polymer solution of 2.8% w/w and thickness of the polymer film of 120±5 nm; (c) 50%. The data for a such humidity level presented in a single sample; (d) 60%. The blue data corresponds to the concentration of the polymer solution of 2.8% w/w and a thickness of the polymer film of 120±5 nm; (e) The creep compliances for PVAc polymer films, measured by McKenna et al. [29]. The sample was a 28 nm thick PVAc film tested at a temperature of 26°C and a pressure of 0.27 atm.

Still, the tendency of the creep compliance to be dependent on the humidity level is visible: the higher humidity level shows the higher creep compliance value. The small difference between creep compliances of 40% and 60% humidity level can be explained by the close level of the polymer film plasticization, while between low humidity and high humidity levels the difference is visible. Such a result and arguments that were specified above prove the assumption that humidity acts on the PVAc polymer films as a plasticizer, as indicated in other works [28, 29], which can also be seen in Fig.4.16e.

4.3.3 Inflection of the PVAc films

The inflection of the bubble for the ultrathin PVAc polymer films was observed for two experiments performed at the high humidity level of 60% and for two concentrations of polymer solution: 2.6% w/w and 2.8% w/w (corresponds to 110 ± 5 nm and 120 ± 5 nm thickness) (Fig.4.17).

The change in the bubble shape and inflection for PVAc polymer films can be explained by an enormous bubble deflection of around 350 nm. In comparison, maximum deflection obtained for the PS polymer films was around 250 nm (Fig.4.10). The bubble might become unstable due to large deflection and lead to the bubble shape fluctuation and wobbling. The inflection of the bubble for PVAc appeared around 100 minutes after the start of the experiment in both cases. The overall behavior of the bubble during inflection is similar for both polymers, PS and PVAc. After the inflection occurs, the bubble shape changes and the fitting of the bubble shape is not possible. One can notice that for the PVAc film during inflection, the data for the bubble height is not as scattered as for the PS films. But the difference of the deflection scale is higher for the PVAc bubble, so that the scattering and play of the bubble height might not be that visible in Fig.4.17c. Due to the change of the bubble shape, the stress and strain calculation is inappropriate and not representative for the true stress and strain of the polymer film.

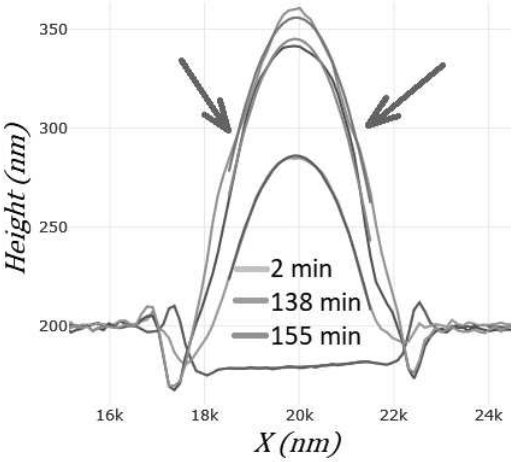

(a)

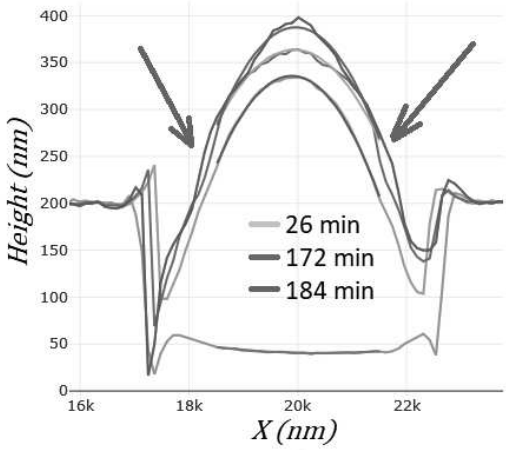

(b)

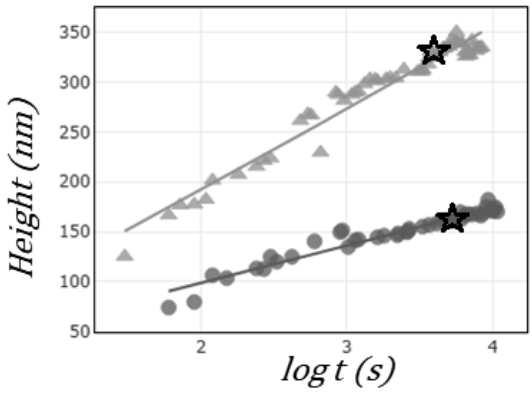

	B_0	α	h_0
▲	2911.436	0.011	-1188.006
●	1214.629	0.012	138.923

(c)

Figure 4.17: The bubble inflection and change of shape for a humidity level of 60%. The red arrows show the inflection regions. (a) Bubble deflection of the polymer film prepared at concentration of 2.8% w/w, which corresponds to a thickness of 120 ± 5 nm; (b) Bubble deflection of the polymer film prepared at a concentration of 2.6% w/w, which corresponds to a thickness of 110 ± 5 nm. (c) The evolution of the bubble height during the experiment over the 3 hours of the experiment in (a) presented in circles and (b) presented in triangles, fitted with Eq.4.1. The stars represent the point in time, when the inflection of the bubble appears. The parameters for the fits are presented in the table.

4.3.4 Conclusions

The experiments using the microbubble inflation technique were performed on ultrathin PVAc films of 100-120 nm thickness in order to investigate the influence of humidity, while the pressure level was identical for all experiments. A variation in the humidity from 10-60% was used in the experiments. The response of the polymer film appeared to have a creep behavior for all levels of humidity. But exceptions appeared for higher humidity levels. The elastic-like behavior was achieved for 25% and 50% of humidity with a huge deflection of the bubble compared to the experiments with the same humidity levels, but in creep behavior. The explanation might be that for such a case of elastic-like behavior, the huge deflection appears due to fast deflection of the bubble during the first moments of applying the pressure and the polymer film evolving too fast to catch it with the present setup. The overall tendency of the bubble height evolution and creep compliance show an increase with increasing humidity level. Such a result proves the suggestion that humidity acts on the PVAc polymer film as a plasticizer.

The inflection of the PVAc polymer film at high humidity level has similarities with the inflection behavior of the PS polymer films at high pressure level. The shape of the bubble for both, the inflection of the PS and PVAc films, changes in the same way, which can be a proof of the identical process of bubble inflection point appearance and overcoming of the yield point.

The project could be usefully continued in further work by investigating the influence of humidity for thinner PVAc films, particularly for polymer films below 60 nm, when the T_g decreases with a decrease in the film thickness. At that point, the influence of the annealing temperature, the pressure level and temperature of the experiment could be additional characteristics that influence the behavior of the PVAc ultrathin films.

Chapter 5

Modeling of the bubble inflation for PS films

Since the experiment based on the microbubble inflation technique is complex and sensitive to many different parameters, the extraction of the mechanical properties of the ultrathin polymer films is complicated. Modeling of the experiment using Finite element modeling was therefore performed in order to be able to compare the results with those from experiment.

In order to extract the mechanical properties of the ultrathin polymer films and the mechanism of bubble creation during the experiment by investigating the behavior of the bubble growth and inflection, a model using the Marc & Mentat environment was developed.

The model was improved during the process of the development and validation of the model to the point of becoming reliable and able to mimic the real characteristics and geometry of the polymer film from the experimental measurements.

In this chapter the results on the building and validation of the model by two test models, based on the pressure and the displacement, are presented. Alongside, the main points of model improvement to be close to the real experiment are noted. In addition, the results on the bubble inflation to mimic the experiment and the Young's modulus determination are also presented.

5.1 Computational strategy

The model of the polymer film inside the hole of the grid was built from a mesh containing 2065 elements in the form of a circle with a diameter of 5 mm. Such dimensions differ from the real size of the hole, but this has no influence on the pressure calculations during the validation of the model. In addition, the units for the length scale of mm corresponds to units of force in N and pressure of Pa, which simplifies the calculations of forces and pressures in the models. The high number of elements in the model during validation serve to minimize the errors in the process of calculating the pressure. The boundary conditions of the model were inserted into the model so as to fix the edges of the circle and so mimic the attachment of the polymer film to the edges of the hole in the grid.

The first step was to start with the pressure model. In this case, the Element type of the film was chosen to be a Thin shell. Despite the fact that this model is less realistic compared with the experiment since it does not include the pre-stress of the membrane, it was built for the following reasons:

1. To check if the model is reliable in terms of the initial conditions of pressure input compared to the pressure that acts on the film of the bubble evolving over time.

2. To set the pressure which causes the growth of the bubble and acts in the z-direction in order to obtain the shape of the bubble. The calculated shape of the bubble is useful for being able to compare it with the experimental result, as well as for validating the displacement model. The shape of the bubble calculated from the pressure model was then transferred to the displacement model to calculate the pressure that acts on the elements. The displacement model is expected to be more reliable and close to reality since the Element type corresponds to the membrane, which is more stable and includes the pre-stress of the membrane.

3. To compare the results on the pressure that acts on the elements of the film for both the pressure and displacement models to the initial pressure input.

Then, the displacement model was built to mimic the real experiment, but with a slight difference. The pressure input in the displacement model is replaced by implementing the shape of the bubble in the model. Thus, the simulations are controlled so as to match the experiments. The final model to mimic the experiment with realistic dimensions of the film and the grid hole was built on the basis of the displacement model.

5.1.1 Pressure model. Pressure calculation.

The pressure model was created to check the reliability of the pressure values after performing the simulation to mimic the bubble growth from the pressure input. This can be done by calculating the pressure that acts on the elements of the film and comparing it to the pressure input value. The boundary conditions for the pressure model are set to fix the edge of the film and to apply the pressure for the internal part of the membrane. The pressure calculation that acts on the elements of the film starts with the estimation of the forces that act on the four nodes of one element of the mesh. Each node in Figure 5.1 has x, y, z -components of the force, which represent the force that acts on the element from the neighboring elements.

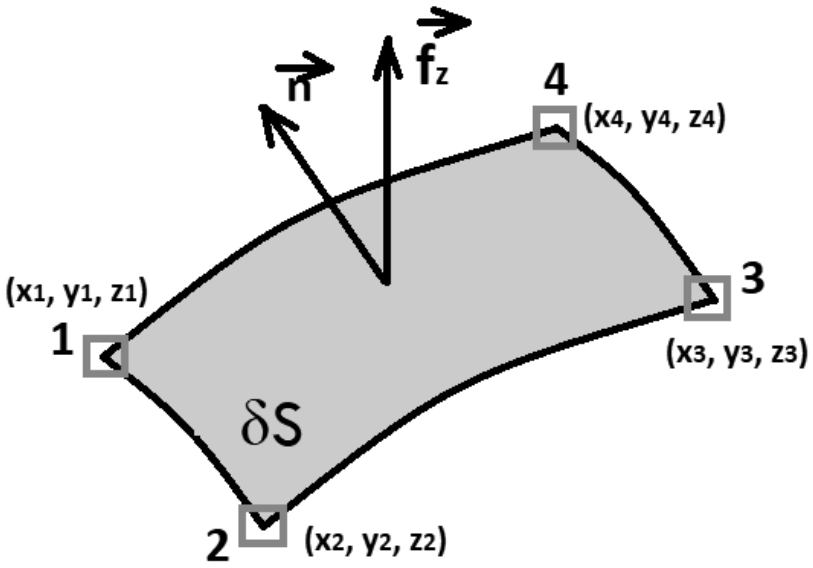

Figure 5.1: Schematic diagram of an element of the deformed mesh with four nodes. Each node has f_x^{node}, f_y^{node}, f_z^{node} component of force that acts on the element from the other elements. The vector f_z represents the sum of four f_z^{node} components. The vector $\vec{n}$ is the normal to the element plane.

As the pressure is only applied in the z-direction, we are only interested in the z-component of the force of each node (the x- and y-components are close to 0). While such an assumption about the z-direction only is far from the reality, since the displacement model is finally used, this inaccuracy can be ignored and focus can be placed on obtaining only the pressure value in the z-direction. The total f_z for each element is the sum of the residual forces from each node, which is taken from the output file of the simulation. The normal vector is calculated from the coordinates of the nodes. To find the total force that

acts on the element, the scalar product of the vectors is calculated as:

$$f = \vec{n} \cdot (0, \vec{0}, f_z) \tag{5.1}$$

or

$$f = n_z \cdot f_z \tag{5.2}$$

The pressure is calculated as:

$$P = \frac{f}{\delta S}, \tag{5.3}$$

where δS is the initial face area of the element before deforming. The initial face area was used in the calculation as it is the projection of the deformed area on the XY plane.

Both test model systems were built using a polystyrene film thickness of 0.1 (mm) with a Young's Modulus of 600 (MPa) and Poisson's ratio of 0.25. The structural element type for the pressure model is set to a thin shell. The film deforms under the pressure of 1.253 (MPa) according to the elastic law. Such a pressure value is high enough for bubble growth at comparable height-to-diameter ratio as in the experiments. The simulation is set for 1000 steps. In addition, as we are interested in the forces that act on the elements, the tolerance of the force estimation is set to 0.01 (precision for the force balance).

Following the procedure of determining the pressure presented above, we obtained the averaged pressure for the series of elements over the radius of the bubble. The value of pressure appeared to be p = 1.251 MPa, which is close to the initial conditions (p = 1.253 MPa) of the model (Fig.5.2).

The scattered data of the pressure along the radius of the film can be explained by different face areas of the elements and an error of the normal vector estimation. Finally, the close value of the pressure compared to the pressure input leads to the conclusion that the model is reliable and can be used for further development.

5.1.2 Displacement model

The displacement model contains certain changes compared to the pressure model. Firstly, the element type was changed to a Membrane Element Type in order to be as close as possible to a real polystyrene film, which implies the input of pre-stress of the membrane (see more in Section 5.4). Secondly, the pressure input was changed to a displacement

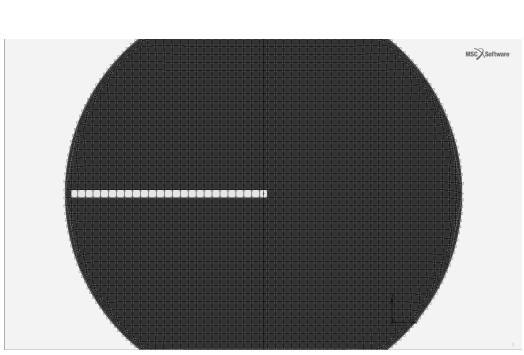

(a)

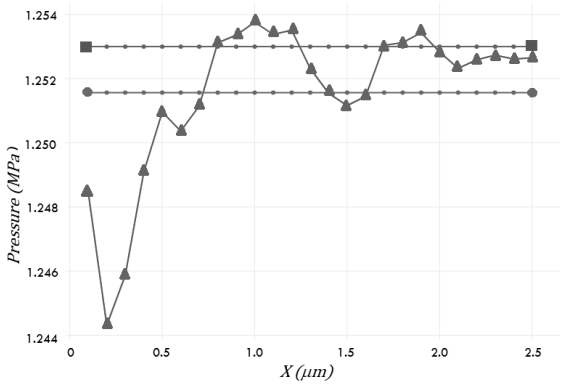

(b)

Figure 5.2: (a) The mesh of the model to validate the pressure and displacement model. The elements along the radius of the bubble that were chosen to calculate the pressure that acts on the bubble from external forces are presented in green; (b) The values of the pressure, calculated for elements along the radius of the bubble (triangles), the applied pressure in the model (squares) and the average of (a) (circles). The averaged value of the pressure 1.251 MPa calculated in the pressure model is close to the initial pressure applied of 1.253 MPa.

law, which is an alternative to applying pressure during the experiment. The idea is to use the law for bubble evolution that is based on the shape of the bubble from experiment using the spherical function fit Eq.3.11. But for validation of the model, the shape of the bubble from the pressure model, described above, was used first.

The pressure obtained for the displacement model showed the value of the averaged pressure along the radius of the bubble p = 1.241 MPa, which is close to the initial pressure applied of 1.253 MPa. The slight difference in pressure values, obtained from the forces that act on the elements for the two models, pressure (1.251 MPa) and displacement (1.241 MPa) can be explained by the different element types between the two models, a thin shell and a membrane. Still, the values are close to the initial pressure input and both models can be considered as being successfully validated.

5.2 Model characteristics

The final and realistic model was changed to a 30 nm-thick membrane and 5 μm diameter of film with a mesh divided into 493 elements with four nodes in each element. The characteristics of the polystyrene thin films were used: Young's modulus $E = 5 \times 10^9$ Pa and Poisson's ratio ν=0.35. Both values were taken from the literature [80]. Figure 5.3 shows the mesh of the final model of 493 elements with four nodes in each element.

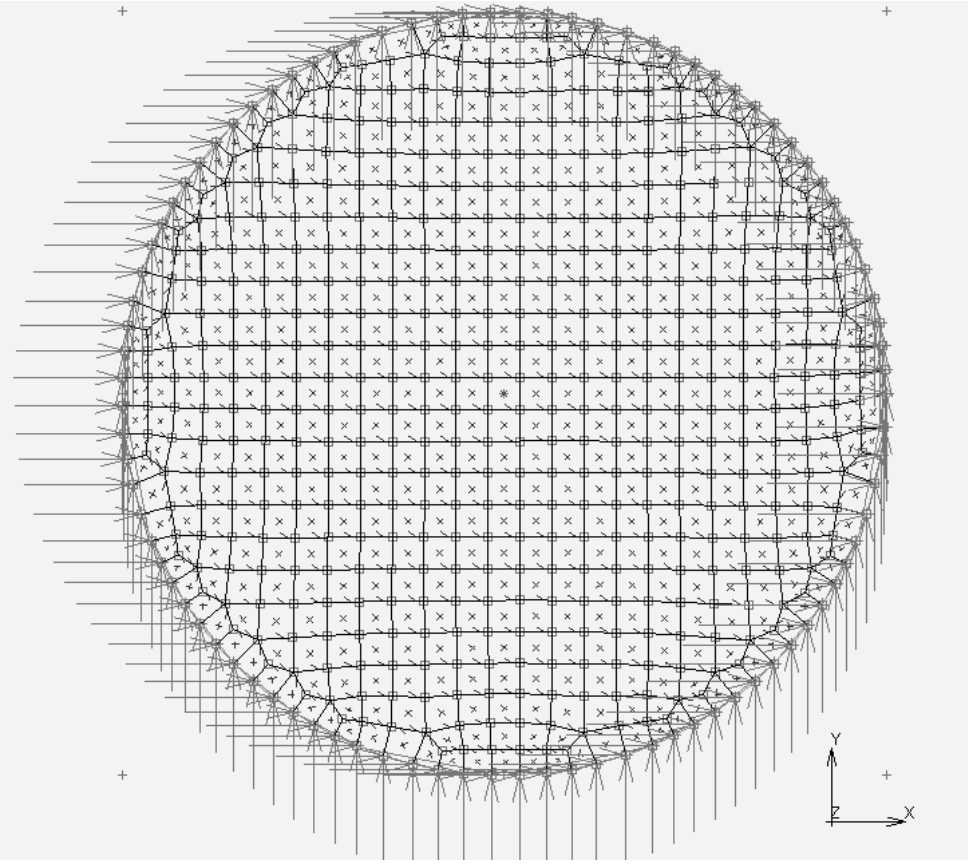

Figure 5.3: The model of the 30 nm-thick polystyrene membrane, divided into 493 sections. The arrows represent the boundary conditions for the fixing of the edge of the membrane.

The number of elements is not that critical for further calculations. But the fewer number of elements simplifies and speeds up the time for the calculations per simulation.

5.3 Bubble inflation

In order to have realistic bubble inflation to mimic the experimental conditions, the model was then updated with two points of elaboration. Firstly, to mimic the bubble height during a real experiment, the experimental data on creep of the bubble was fitted with a spherical function Eq.3.11. The result of the fit was placed into the displacement model as a law of bubble growth, so that the simulations are now built from experimental data. Secondly, to mimic the non-linear deflection evolution of the bubble over time, the bubble height evolution data from the same experiment was fitted with a power law:

$$h(t) = B_0 \times (t^{\alpha}) + h_0, \tag{5.4}$$

where B_0, α, h_0 are fitting parameters. The result of the fit is presented in Fig.5.4.

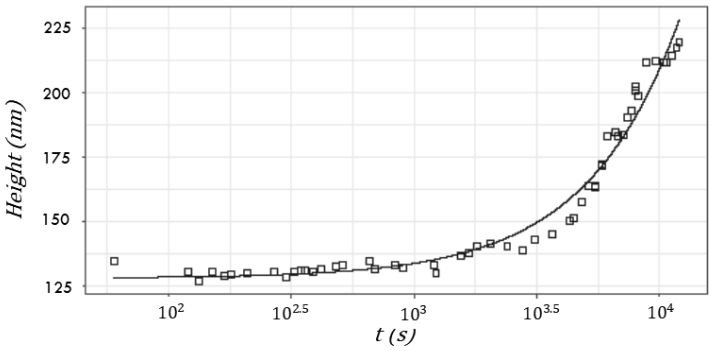

Figure 5.4: The dependence of the bubble height over time for the creep experiment (squares), fitted with Eq.3.11 (line).

Such an improvement in the model makes it possible to come closer to the experimental conditions, and a more precise extraction of the mechanical properties. The problem of extracting the mechanical properties lie in the difference between the strain and stress that were determined from the radius of curvature in the experiments and the stress and strain in the simulations. When considering the stress in the experiment in relation to the pressure, it is expected that the stress be constant for a constant pressure, with only the strain changing. But in this work, the stress is not this stress, but the internal stress of the polymer film, which is not the same. Because of this difference, the simulation cannot give the information on the internal stress, but only on the stress from applying the pressure. Because of this, the stress and strain in the simulations cannot be compared to what we obtained before. But, there is still the mechanical property that is available from the simulations that can lead to information that is not available from the experiment: the Young's modulus.

5.4 Young's modulus & Pre-stress

When the formula to mimic the bubble growth in the experiment was updated, the question of which Young's modulus value to use appeared. In the literature, the Young's modulus for a similar ultrathin polymer film is reported to be around 5 GPa [80]. The rough estimation of the Young's modulus for the elastic behavior data gave the result of 7 GPa (see § 4.2.2). But for such a value of the Young's modulus, using the simulations in Marc Mentat, the bubble height appeared to be grater than that expected from the experiments. To find the Young's modulus that would fit the real data from the experiment, a few different values of the Young's modulus were used in a model to find that

which matched (Fig.5.5).

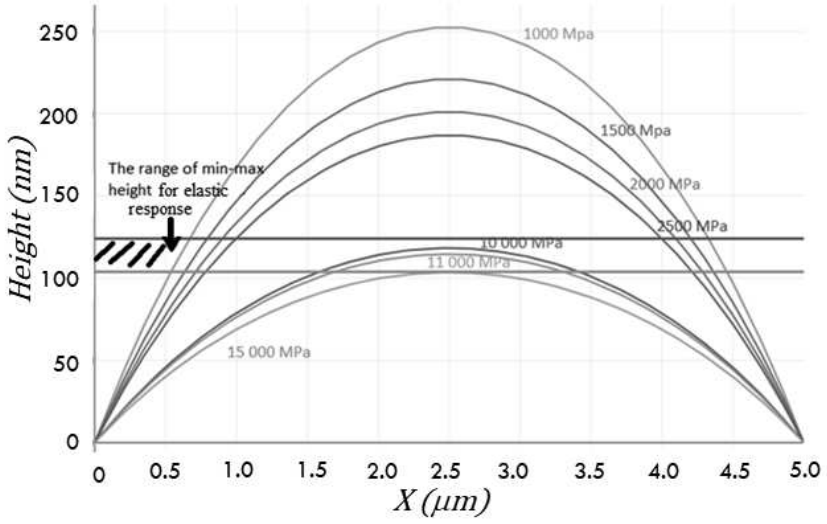

Figure 5.5: The various bubble heights depending on different values of the Young's modulus to meet the requirements of the bubble height from the elastic response of the 30 nm-thick PS polymer film.

As can be seen from Fig.5.5, to mimic the bubble deflection from the experiments, the Young's modulus appeared to be around 11 GPa, which is twice as high as that expected. Such a value of Young's modulus also appeared to be in agreement with the experimental data on the bubble height of the elastic response for an applied pressure of 0.7 atm.

In order to lower the value of the Young's modulus in the model to be more realistic, the next step was to implement the pre-stress of the membrane to the model. As the pre-stress and Young's modulus are competing characteristics of the material, by including the pre-stress, the Young's modulus should decrease. The pre-stress value was set to 2.6 MPa, which was calculated from the surface tension of 40 mN/m for similar PS films using Eq.5.5. The pre-stress was calculated from the surface tension using the equation:

$$\sigma_{xx} = \sigma_{yy} = \frac{2\gamma}{t_0}, \tag{5.5}$$

where γ is the surface tension of the polymer film, t_0 is the thickness of the polymer film and the factor 2 appears due to the two free surfaces of the freestanding film. The value of the surface tension for the polystyrene film of similar thickness was taken from the literature [77, 78].

To observe the influence on the Young's modulus values by changing the pre-stress and vice-versa, numerous calculations were performed with the models (Fig.5.6-5.7).

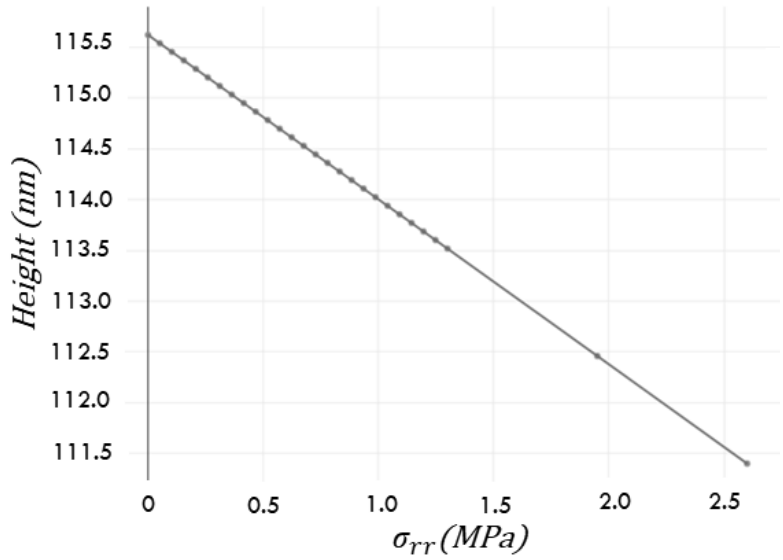

Figure 5.6: The dependence of the bubble height in modeling from different pre-stress values at a constant Young's modulus of 11 GPa. The change in bubble height is around 4 nm from applying the whole pre-stress of 2.6 MPa to the switching off of the pre-stress.

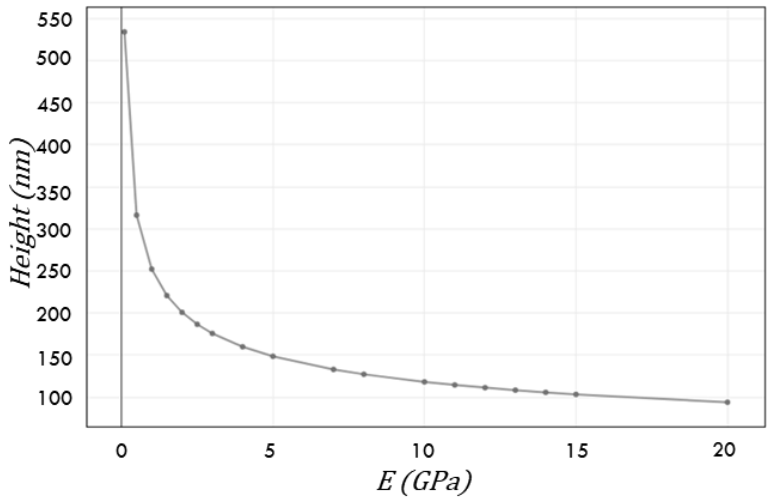

Figure 5.7: The dependence of the bubble height in modeling from different Young's modulus values at a constant pre-stress of 2.6 MPa. The change in bubble height is 400 nm from applying E=0 to the E=20 GPa.

As can be seen from the Fig.5.6-5.7, the influence of the Young's modulus on the bubble height is primordial, while the influence of pre-stress is small. Finally, the Young's modulus to achieve the height of the elastic response from the experiment was found to be around 11.1 GPa for the case without the pre-stress. On the contrary, the model including the pre-stress of 2.6 MPa (corresponding to a surface tension of 40 mN/m) showed a Young's modulus of around 10.8 GPa. So, the Young's modulus is lowered when taking into account the pre-stress, but not enough as was expected (E =5 GPa). Also, to use the Young's modulus of 5 GPa as reported in literature, the pre-stress would have to be around 13 MPa, which is unrealistic.

5.5 Theoretical prediction of the bubble growth under constant pressure

From another point of view, the theoretical prediction of the bubble deflection from applying the pressure in order to validate the model even for high values of Young's modulus was used:

$$h = R_0\Big(\frac{1}{\kappa} - \sqrt{\frac{1}{\kappa}^2 - 1}\Big) \tag{5.6}$$

with

$$\kappa = \sqrt[3]{\frac{3pR_0}{eE}} \tag{5.7}$$

where R_0 is the initial radius of membrane, p is the applied pressure, e is the thickness of the membrane, E is Young's modulus and h is the bubble deflection. The κ in Eq.5.7 does not include the surface tension. The theoretical model that include the surface tension has the form of:

$$ln\Big(\frac{sin^{-1}(\kappa)}{\kappa}\Big) - \frac{\pi_1}{\kappa} + \pi_2 = 0, \tag{5.8}$$

with

$$\pi_1 = \frac{R_0 p_0}{2eE} \quad \text{and} \quad \pi_2 = \frac{2\gamma}{eE}, \tag{5.9}$$

where γ is a surface tension. The Eq.5.8 can be linearized into the form of

$$\kappa^3 + \frac{12\gamma}{eE}\kappa = \frac{3pR_0}{eE} \tag{5.10}$$

The results of the bubble height using the theoretical prediction with and without the surface tension, is presented in Fig.5.8.

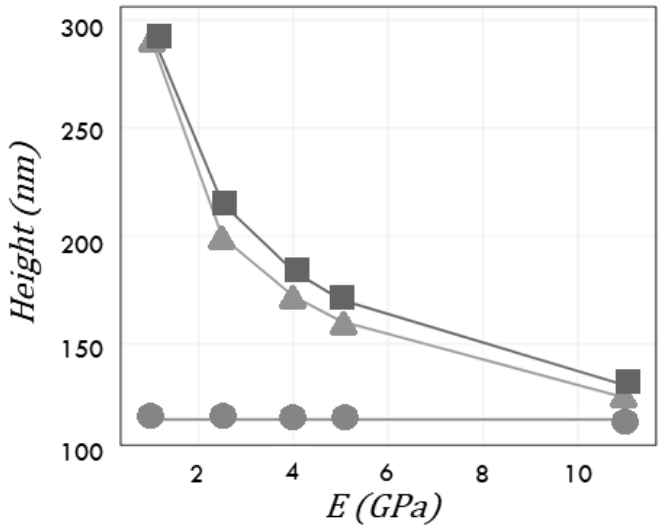

Figure 5.8: The theoretical prediction of the bubble deflection with the applied pressure. The squares represent the theoretical prediction without surface tension, calculated by Eq.5.6-5.7. The triangles represent the theoretical prediction including surface tension, calculated by Eq.5.6,5.10. The circles correspond to the bubble height from experiment for the same pressure level as was used in the model.

The theoretical prediction with surface tension was compared to the simulations for the same characteristics of the polymer film and experiment using the non-linearized model from Eq.5.8 (Fig.5.9).

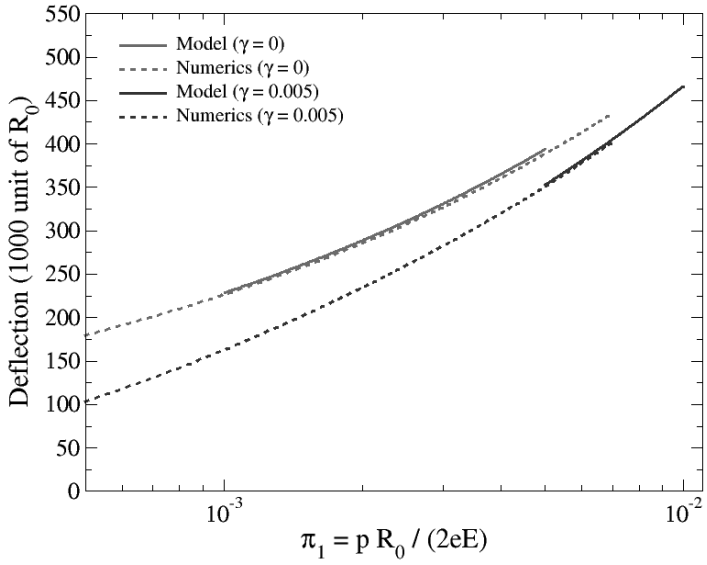

Figure 5.9: The theoretical predictions of the bubble deflection including both cases, with and without (γ=0) surface tension, are represented by the solid lines. The bubble deflection obtained from the simulations is represented by dashed lines.

The agreement between the theoretical prediction and simulation show that the value of Young's modulus from the literature might not be valid for such confined systems. By resolving the doubts concerning the Young's modulus value, the final model can be

considered as being reliable for further investigations of the mechanism and process of polymer film bubble formation and inflection.

5.6 Conclusions

Modeling using the Marc Mentat environment was used to complete the experiment and extract such mechanical properties as the Young's modulus due to the fact that the experiment cannot provide such information. The model was validated through two test models based on the pressure and the displacement. The calculations of the pressure that acts on the elements showed an agreement with the initial input pressure for both models. The final model was created in the same dimensions as the sample in the experiment. The Young's modulus in the final model appeared to be around 11 GPa, which is higher than the value of 5 GPa reported in the literature and the value of 7 GPa, obtained by a rough estimation from the elastic behavior from the experiments on the PS films. In order to decrease the value of the Young's modulus, the surface tension was implemented in the model in the form of pre-stress of the film. The presence of pre-stress lowered the Young's modulus to 10.8 GPa, which is still high, but lower than the initial value. In order to validate such a value of the Young's modulus, the theoretical prediction of the bubble deflection was used. The theoretical prediction showed agreement with the simulations with the surface tension being taken into account. The model was finalized by implementing the non-linear evolution of the bubble height over time and the shape of the bubble, taken from the experimental data to mimic the creep of the polymer film from the experiment. The model was thus validated and can be considered as being reliable for further investigations of the mechanism, the process and behavior of the polymer film bubble formation, and growth through the creep and inflection.

Chapter 6

Conclusions & Perspectives

In this work the microbubble inflation technique coupled with interference microscopy was used in order to investigate ultrathin polymer films of two polymers: Polystyrene and Poly(vinyl acetate). The polymer films in response to the applied pressure showed three behaviors for both, PS and PVAc: elastic-like, creep and inflection.

For the **PS** films the transition between these behaviors was found to be related to the change of pressure level, but with certain exceptions for some experiments, which can be explained by sensitivity of the experiment to the conditions during sample preparation, annealing and to the experimental conditions.

The elastic-like behavior, during which the bubble grows over the first few moments after the start of applying the pressure and the bubble height stays at the same level for the whole time of the experiment was observed for experiments with low pressure level, with a slight transition to creep for higher values of pressure. The mechanical properties of the polymer film, stress and strain, are constants for the elastic-like regime and are lower than during the creep behavior.

The creep behavior was observed for higher pressure levels and showed a strong dependence on bubble height with increased pressure levels. The evolution of the bubble over time enables the calculation of creep compliance from the time dependencies of the strain and stress. The creep compliances were calculated for various experiments for different pressure levels and at different annealing temperatures (Fig.6.1). The results of the creep compliance are comparable with previous investigations on similar polymer films [29].

The inflection of the bubble was observed for certain experiments at the high pressure level. The bubble height was found to be more scattered compare to the creep experiments

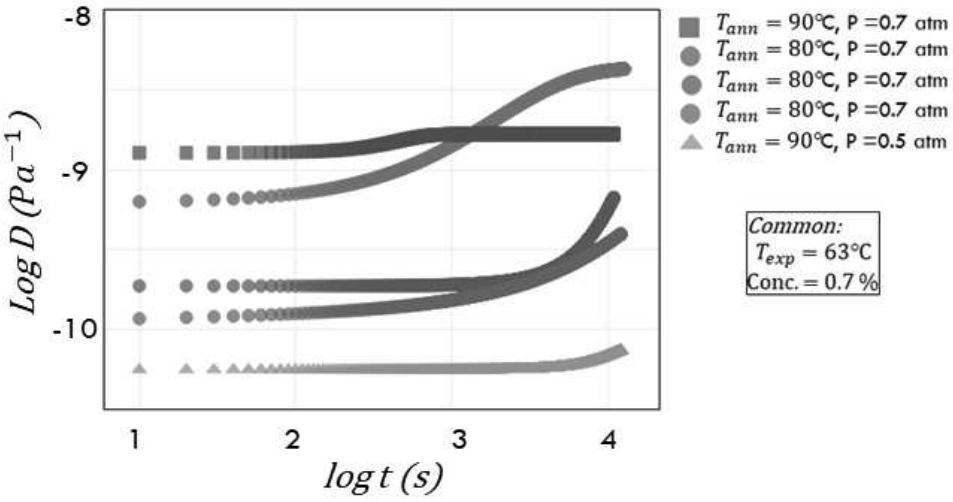

Figure 6.1: The creep compliances for the various experiments at different pressure levels and different annealing temperatures. A higher pressure level leads to an increase in the creep compliance values. At the same point, the higher annealing temperature leads to an increase in the creep compliance for the higher value of pressure compared to the lower annealing temperature.

as the bubble shape changes after the inflection points appear. The fitting of the bubble in order to extract the mechanical properties was found not to be valid as the shape of the bubble changes and the fit no longer follows the bubble shape. The change in the bubble shape proves an assumption that the bubble overcomes the creep regime and deforms in a plastic-like regime so that the polymer film does not recover the initial shape after the pressure is removed. The mechanism of the bubble inflection for microbubble inflation is unknown and requires further investigation.

The experiments on the **PVAc** polymer films were performed as a function of the humidity. A strong correlation between the humidity level and bubble height was observed (Fig.6.2), which can be coupled to the creep compliance dependence on the humidity.

The result on the bubble height and creep compliance proves the suggestion that humidity acts as a plasticizer on the ultrathin PVAc films.

The inflection of the PVAc polymer films was observed at high humidity levels of 60%. The behavior of the bubble after the inflection points appeared showed the similarities to inflection of the PS films at high pressure level. The form of the bubble shape is similar for both polymers for the inflection behavior, which is an argument for an identical process of inflection appearance and an overcoming of the yield point.

To investigate the process and mechanism of the polymer film deflection with the

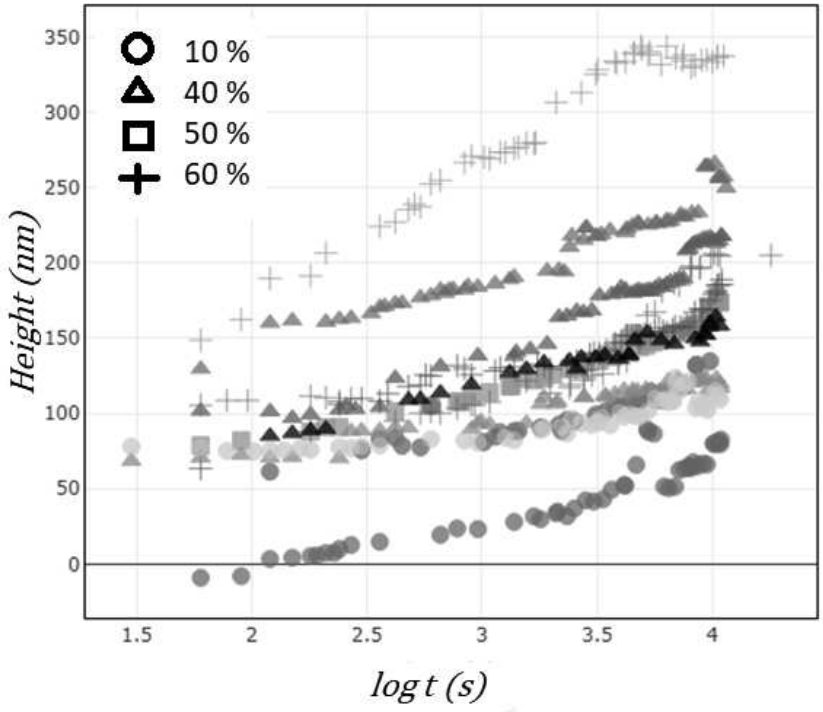

Figure 6.2: The dependence of the bubble deflection evolution over time of the experiment (180 minutes). Four different humidity levels presented in symbols: 10% in triangles, 40% in circles, 50% in squares, 60% in crosses.

applied pressure, so as to extract the mechanical properties of the polymer films, which cannot be obtained by experiment, the **FEM** was used to build the model and mimic the microbubble inflation experiment on the PS film. The model was validated by two test models, based on pressure and more realistically, on displacement, by calculation of the pressure value and comparison to the initial pressure input. Both models were in agreement in terms of the pressure. The displacement model was then improved to realistic dimensions to match the experimental conditions. The Young's modulus was extracted from the final model and appeared to be around 11 GPa, which is higher than the value of 5 GPa reported in the literature and roughly estimated value from experimental data of this work of 7 GPa. In order to decrease the Young's modulus and improve the model at the same time, the surface tension was implemented into the model in the form of pre-stress of the film. The presence of the pre-stress lowered the Young's modulus, but not as much as was expected, the new value being equal to 10.8 GPa. To resolve the difference between the value reported in the literature and the value of Young's modulus from the simulations, the theoretical prediction on the bubble deflection from the applied pressure was used and compared to the simulations (Fig.6.3).

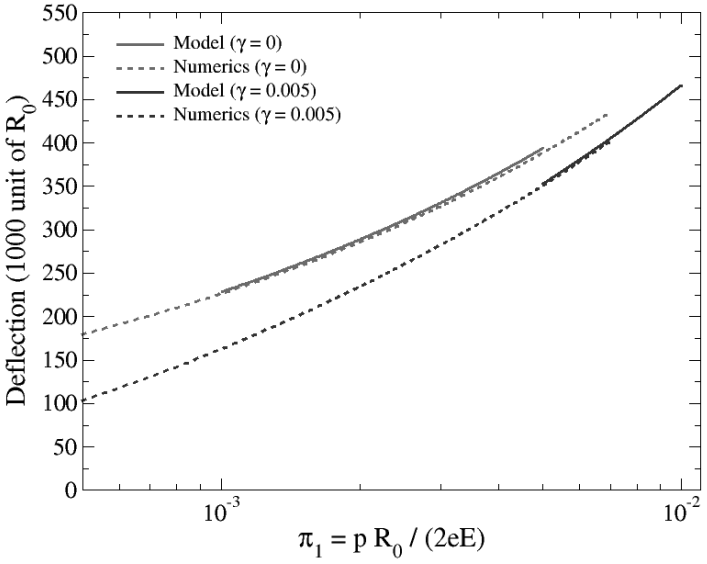

Figure 6.3: The theoretical prediction of the bubble deflection including with and without (γ=0) surface tension is presented in solid lines. The bubble deflection obtained from the simulations is represented by dashed lines.

The theoretical prediction showed an agreement with that from the simulations for both cases, including surface tension in the model or not. The model can be considered as being reliable for further investigations of the mechanism and behavior of the polymer film during bubble inflation.

The perspectives of the project can now be advanced to both the experimental and modeling part of this work. As mostly only the influence of the pressure level for the PS films was investigated in this work, the influence of the other characteristics is still an open question:

1. Annealing procedure (including temperature, duration of annealing, the speed of cooling down the sample). The possibility of attaching the polymer film to the grid without annealing should be considered. This would remove the huge factor of the influence on the behavior of the polymer film;

2. Thickness of the polymer film. The protocol of polymer film preparation can be extended to thinner polymer films. Also, the measurement of the polymer film thickness for each sample will increase the statistics on the value of the thickness and decrease the error in the T_g determination;

3. The change in thickness of the sample will lead to a change in T_g and temperature of the experiment to keep the sample at the required $0.9T_g$;

For PVAc polymer films, the main question is to advance the protocol to thinner polymer films, which would lead to a decrease in T_g, which would also lead to changes in the experimental conditions.

As the simulation model to mimic the microbubble inflation is now ready for further use, the question of bubble inflection mechanism investigation is open. As experimentally it is not possible to extract the mechanical properties of the polymer films during the inflection behavior, the simulation of this case could give the answers concerning this phenomenon.

The investigation of the behavior of polymer films under different environmental conditions in this doctoral work has led to some initial valuable information on the mechanical properties of ultra thin films. Despite the complexity of the experiment and intriguing results, the overall tendencies of polymer film behavior were obtained and analysed. The appearance of three behaviors as a response to different environmental conditions for both polymers presented in this work allowed us to compare and analyse the process of bubble growth in detail. As the phenomenon of bubble inflection appeared in the same manner for both polymers, the mechanism of it's appearance is most likely the same and remains one of the most promising points for further investigations. The modeling performed has allowed us to mimic the experiment of microbubble inflation, complete the experimental results and extract the mechanical properties of ultrathin polymer films. With the miniaturization of polymer films being one of the main questions in polymer physics today, such studies using interferometry and optical characterization could be further explored more widely so as to improve the properties of such thin films and allow them to be used in more and more areas of our lives.

Chapter 7

Résumé en français

Les polymères sont des matériaux présentant des avantages significatifs en termes de stabilité mécanique, de flexibilité et de fonctionnalité. Ils sont largement utilisés dans de nombreux domaines de notre vie quotidienne, dans les domaines de la science des matériaux, de l'industrie, de la médecine, etc. Le progrès technique exige que ces matériaux soient adaptés à de nouvelles formes d'utilisation, avec des modifications de leur structure et même la synthèse de nouveaux polymères. L'une des caractéristiques les plus importantes que l'on exige aujourd'hui d'un matériau polymère est le maintien de sa stabilité lors de la réduction de sa taille. Les polymères sont utilisés comme matériau de revêtement ou comme partie du dispositif lui-même et sont donc largement utilisés dans les micropuces, les cartes de circuits imprimés, les cartes mères et les dispositifs de stockage d'énergie, etc. ainsi que dans les revêtements optiques et dans d'autres applications importantes.

7.1 Films polymères en vrac et ultraminces

Avec les caractéristiques bénéfiques de plasticité, d'élasticité et d'endurance des polymères, ce sont les raisons de l'intérêt croissant pour les polymères au fil des ans. Les polymères se distinguent des autres matériaux par l'existence d'une température caractéristique bien définie - la température de transition vitreuse T_g qui marque la transition entre deux états du polymère : un matériau dur et rigide en dessous de T_g et un matériau souple et mou de type élastomère au-dessus de T_g. La percée scientifique significative dans le domaine des polymères de taille réduite a été l'étude des films polymères ultraminces (moins de 100 nm) proposée par Keddie et Jones il y a 25 ans [3]. Ils ont remarqué une diminution

drastique de la température de transition vitreuse T_g due à la diminution de l'épaisseur du film et ont marqué le début d'une étude substantielle des polymères confinés. Dans cette gamme d'épaisseur (< 100 nm), les chaînes du polymère sont tellement confinées que les bobines aléatoires peuvent être dénaturées. Simultanément, on a remarqué que la nature du changement de T_g dépendait de la nature chimique du polymère lui-même et de sa configuration : une diminution remarquable de T_g jusqu'à 80 K pour le polystyrène (PS) [3] et un changement ambigu (diminution ou augmentation) de T_g pour le poly(méthacrylate de méthyle) (PMMA) [4] qui était lié à la présence ou non d'un substrat (libre). Par la suite, les recherches sur les effets de confinement unidimensionnel ont donné lieu à des études non seulement des propriétés statiques des films polymères, mais aussi des propriétés dynamiques, telles que la mobilité des chaînes et l'interaction avec la surface, qui se sont avérées être les caractéristiques entraînant une réduction de T_g [5, 6]. La complexité de la relation entre ces facteurs et la compréhension de la nature et des propriétés mécaniques des polymères confinés et des polymères eux-mêmes sont des sujets clés dans ce domaine aujourd'hui.

7.2 Introduction à ce travail

Cette thèse est axée sur l'étude du comportement des films polymères ultraminces et en particulier sur leurs propriétés mécaniques dans différentes conditions environnementales telles que la température, la pression et l'humidité. Le premier polymère utilisé dans ce travail est le polystyrène (PS) afin d'étudier l'influence de différents niveaux de pression et le comportement du film polymère en réponse à la pression appliquée. Le deuxième polymère, le poly(acétate de vinyle) (PVAc), a été utilisé pour étudier l'influence de différents niveaux d'humidité sur le comportement des films ultraminces de PVAc sous la pression constante appliquée. Enfin, la méthode des éléments finis (FEM) a été utilisée dans l'environnement Marc Mentat pour simuler l'expérience et obtenir les propriétés mécaniques qui ne sont pas disponibles à partir de l'expérience.

En particulier, nous nous concentrons sur l'effet de fluage des films polymères ultraminces et l'atteinte du point de seuil, dans le but d'essayer de comprendre les deux processus et la transition entre eux, tant du point de vue expérimental que de la modélisation.

Le Chapitre 2 présente une vue d'ensemble de la littérature, les principales car-

actéristiques des propriétés mécaniques et physiques des films confinés par rapport au vrac, ainsi que les méthodes d'étude et de caractérisation. Le Chapitre 3 présente les matériaux et les méthodes utilisés dans ce travail : technique d'inflation de microbulles couplée à l'interférométrie. Ensuite, le Chapitre 4 contient les résultats et l'analyse des expériences sur les films PS et PVAc. Les résultats et les détails des simulations sont présentés dans le Chapitre 5. Enfin, les conclusions et les perspectives du projet sont données dans le Chapitre 6.

7.3 Configuration expérimentale

7.3.1 Polymères

Dans ce travail, nous utilisons deux polymères : **Polystyrène (PS)** et **Poly(acétate de vinyle) (PVAc)** :

- **Polystyrène (PS)**, fabriqué par PSS Polymer Standards Service GmbH, Allemagne, M_w=120 000 Da, PDI=1,05, T_g=100°C. Concentrations utilisées dans ce travail : 0.7 - 2.6%, ce qui correspond à une épaisseur de 30-100 nm.
- **Poly(acétate de vinyle) (PVAc)**, fabriqué par Sigma-Aldrich, Allemagne, M_w=100 000 Da, PDI=2,6, T_g=30°C. Concentrations utilisées dans ce travail : 2,6 - 2,8%, ce qui correspond à une épaisseur de 100-120 nm.

Les films polymères PS ont été utilisés pour réaliser des expériences de fluage à l'humidité ambiante, et les films polymères PVAc ont été utilisés pour réaliser des expériences de fluage à humidité contrôlée afin d'étudier l'influence de l'humidité sur le fluage du film polymère.

7.3.2 Cellule de pression et schéma du dispositif expérimental

La cellule de pression utilisée dans le présent travail a été développée et fabriquée sur mesure par le groupe (MIM, ICS et IPP, ICube), fruit d'un travail collaboratif depuis 2016. Le premier prototype développé par Pierre Chapuis (IE CDD), construit autour d'une base en aluminium, disposait d'un contrôle de température et de pression et a conduit aux premières mesures réussies sur le gonflement de la bulle [68]. Le second prototype, également construit par Pierre Chapuis, a permis un meilleur contrôle de l'humidité ainsi que le chauffage de l'échantillon et le contrôle simultané de la pression pendant l'expérience.

Elle est composée d'une base en aluminium et d'un support en aluminium-Téflon pour fixer l'échantillon (Fig.7.1a). Le détecteur de température est placé sur le fond de la partie supérieure de la cellule, qui contient également le détecteur d'humidité et les quatre trous pour la sortie du flux d'azote humidifié (Fig.7.1).

L'échantillon est fixé au support en téflon contenant un trou pour la pression. Pour assurer l'absence de fuites et pour fixer l'échantillon, une languette adhésive double face

(Ted Pella, Inc.) a été utilisée. En découpant un carré au milieu de la languette adhésive, l'échantillon est fixé aux côtés du substrat de Si, uniquement à la grille, évitant ainsi d'endommager la membrane de Si_3N_4. Ensuite, le support en aluminium est fixé avec des vis à la base afin de fixer l'échantillon. Le support a été conçu avec l'anneau Peltier autour de l'échantillon pour un chauffage uniforme de l'échantillon. Ensuite, la partie supérieure de la cellule est placée sur le support et l'anneau Peltier. La couverture complète de l'anneau Peltier par une cellule minimise la perte de chaleur. Le schéma de la cellule et de l'échantillon est présenté dans la Fig. 7.2.

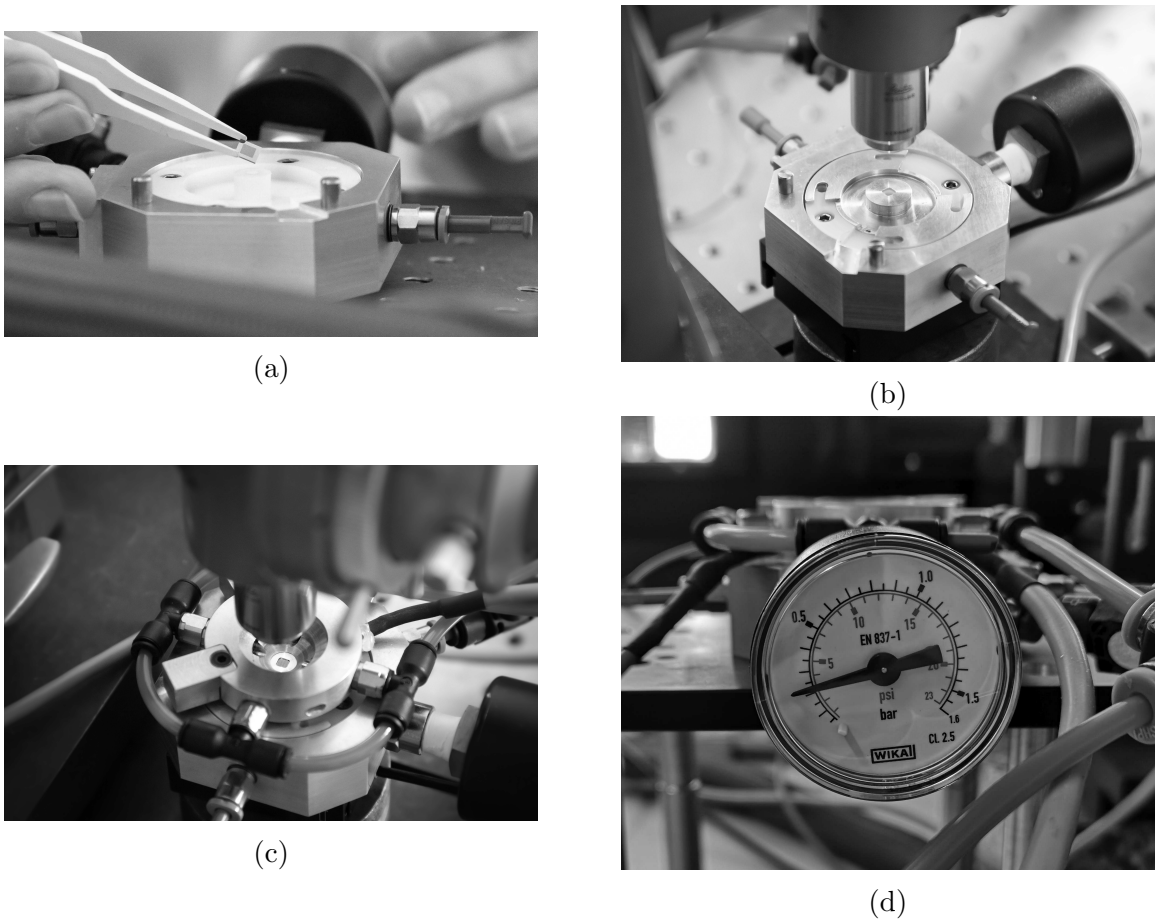

(a) (b) (c) (d)

Figure 7.1: Photos de la cellule de pression fabriquée sur mesure : (a) L'échantillon (grille recouverte d'un film polymère) sur le support en téflon ; (b) Un support en aluminium placé sur l'échantillon pour le fixer. L'objectif avec un faisceau de lumière verte est visible en haut de l'image ; (c) Vue finale de la cellule avec une partie supérieure de la cellule avec quatre trous pour une livraison d'humidité. Le détecteur d'humidité est un fil noir connecté à la cellule à droite de l'image ; (b) Détecteur de pression, qui indique la valeur de la pression d'entrée à l'intérieur de la cellule. La cellule elle-même est située à l'arrière du détecteur.

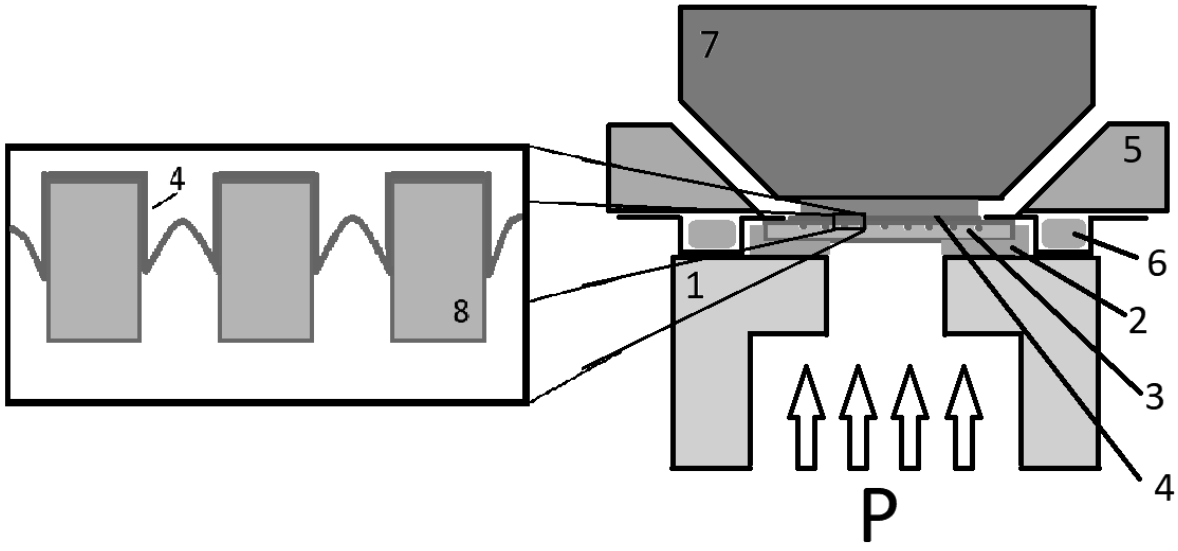

Figure 7.2: Schéma de la section transversale de la cellule expérimentale : (1) Support en téflon avec un trou pour une entrée de pression ; (2) languette adhésive pour assurer l'absence de fuites et la fixation de l'échantillon ; (3) grille avec des trous ; (4) film polymère ultrafin ; (5) support en aluminium ; (6) anneau Peltier ; (7) objectif du microscope à interférence ; (8) membrane de grille Si_3N_4 avec des trous.

7.3.3 Microscope interféromique Leitz-Linnik

Pour obtenir des franges d'interférence sur l'image des bulles, on a utilisé un interféromètre Leitz-Linnik, automatisé par l'équipe de l'IPP et utilisé depuis de nombreuses années pour mesurer la rugosité de surface des échantillons.

Le système se compose de deux bras, qui contiennent deux objectifs identiques de $\times 50$ (NA = 0,85) et construits dans une configuration d'interféromètre Leitz-Linnik (Fig. 7.3a). Un bras contient le miroir de référence, qui fournit un signal de référence d'un faisceau réfléchi. Le faisceau provenant de la réflexion de l'échantillon interfère avec le signal de référence, créant ainsi les franges (Fig.7.3b).

Une source de lumière verte quasi-monochromatique avec $\lambda = 540$ nm est fournie par une LED. La cellule est placée au dessus d'un nanopositionneur piézoélectrique (PI PIFOC), qui assure le balayage contrôlé des franges dans la direction z. Les images sont obtenues avec une caméra CMOS couleur (Photon Focus) montée sur le microscope, avec une connexion Giga Ethernet au PC. Les mesures sont contrôlées par un ordinateur personnel équipé d'un logiciel personnalisé basé sur LabVIEW (National Instrument, ver. 2014, 64 bits) combiné avec le module IMAQ Vision. La version améliorée du logiciel permet l'acquisition et la sauvegarde des données en quelques secondes seulement. La

disposition schématique complète du microscope interférentiel Leitz-Linnik est présentée dans la figure 7.3c, [71]. La technique de mesure de la forme de la surface est présentée ci-dessous.

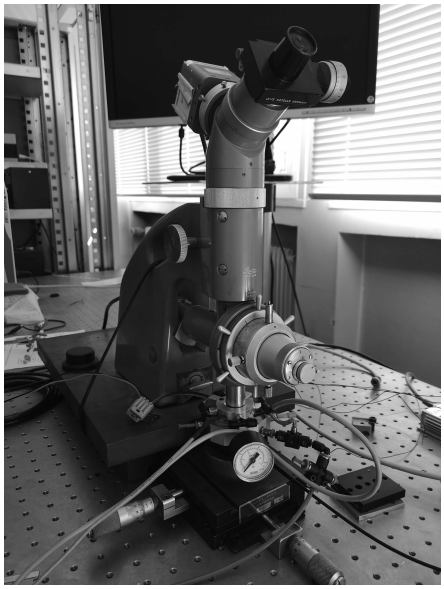

(a)

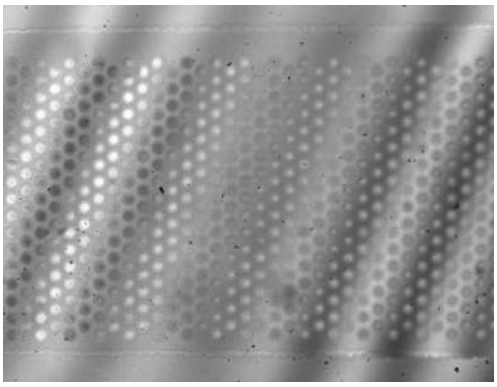

(b)

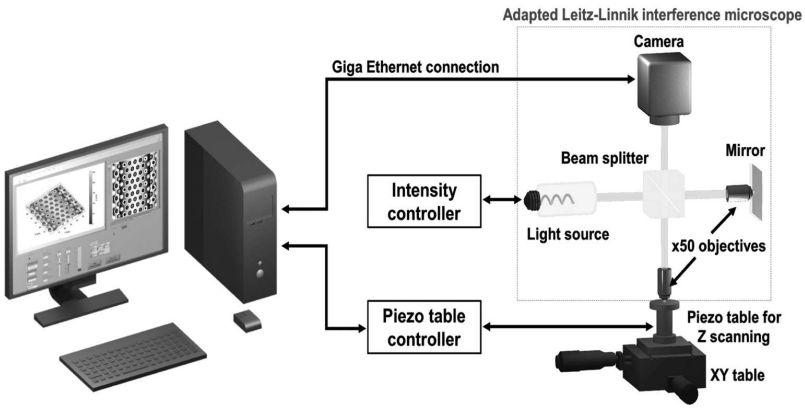

(c)

Figure 7.3: (a) Le microscope interféromique Leitz-Linnik couplé à une cellule de pression et à une caméra; (b) L'image des franges réelles avant traitement. Les deux ensembles de franges correspondent aux réflexions de la membrane Si_3N_4 et de la couche d'oxyde sur le dessus de la membrane, qui selon le fabricant est de ~ 1 μm. Le premier ensemble de franges a été utilisé pour l'analyse de l'expérience, car ce n'est qu'avec ces franges qu'il est possible de se concentrer sur le film de polymère à l'intérieur du film; (c) La disposition schématique du microscope interférentiel Leitz-Linnik; (d) La disposition schématique du microscope interférentiel Leitz-Linnik.

7.3.4 Méthode de gonflage par microbulles

Après le processus de recuit, le film polymère est fixé à la grille. En appliquant une pression sous le film, puisqu'il est fixé par adhésion à l'intérieur du bord circulaire du trou de la grille avec, qui a un diamètre de 5 μm, le film polymère se gonfle en bulle. Dans cette méthode, c'est le rayon de courbure de la bulle qui donne des informations sur les propriétés mécaniques du film. En mesurant le rayon de courbure, la compliance au fluage biaxial peut être calculée grâce à l'historique des déformations et des contraintes. La compliance au fluage, D, est définie par le rapport entre la déformation et la contrainte appliquée. Comme la déformation augmente avec le temps sous une contrainte constante, la compliance au fluage devient une propriété dynamique pour les expériences dépendant du temps.

Le rayon de courbure R pour les petites déviations (quelques centaines de nm pour un diamètre de 5 µm du film) est défini comme suit:

$$R = 1/k, \tag{7.1}$$

où k est la courbure de la bulle, qui peut être ajustée par un polynôme $z(x) = ax^2 + bx + c$ d'ordre 2^{eme}:

$$k = \frac{|z''|}{(1 + z'^2)^{3/2}}, \tag{7.2}$$

où z', z'' sont les dérivées première et seconde de $z(x)$.

La contrainte biaxiale σ_{11} et la déformation biaxiale ϵ_{11} peuvent alors être calculées comme suit:

$$\sigma_{11} = \sigma_{22} = \frac{PR}{2t_0} \tag{7.3}$$

and

$$\epsilon_{11} = \epsilon_{22} = \frac{Rsin^{-1}(\frac{R_0}{R})}{R_0} - 1, \tag{7.4}$$

où P - la pression, t_0 - l'épaisseur du film polymère, R_0 - le rayon du trou et R - le rayon de courbure [44].

Comme le rayon de courbure de la bulle change avec le temps au fur et à mesure de la croissance de la bulle, l'historique des contraintes et des déformations doit être pris en

compte pour calculer la compliance apparente au fluage [29, 72]:

$$D_{app}(t) = \frac{\epsilon_{11}(t)}{\sigma_{11}(t)} \tag{7.5}$$

où $\epsilon_{11}(t)$ - déformation biaxiale dépendant du temps, $\sigma(t)_{11}$ - la contrainte biaxiale dépendant du temps.

Les données obtenues à chaque pas de temps pour la contrainte et la déformation à l'aide de l'équation Eq.7.3 et de l'équation Eq.7.4 sont ajustées par la fonction de Kohlrausch-Williams-Watts (KWW) modifiée [29, 68]:

$$\sigma(t) = \sigma_0 + \sigma_1 \exp\left[-\left(\frac{t}{\tau}\right)^{\beta_\sigma} \right] \tag{7.6}$$

and

$$\epsilon(t) = \epsilon_0 + \epsilon_1 \left(1 - \exp\left[-\left(\frac{t}{\tau}\right)^{\beta_\epsilon} \right] \right), \tag{7.7}$$

où σ_0, σ_1, ϵ_0 et ϵ_1 sont des paramètres d'ajustement, τ - temps de retardement, β_σ et β_ϵ - paramètres de forme pour les courbes de contrainte et de déformation, respectivement.

Par conséquent, la compliance apparente au fluage est déterminée à partir de Eq.7.5.

7.4 Résultats

Dans ce travail, la technique de gonflage de microbulles couplée à la microscopie interférentielle a été utilisée pour étudier les films polymères ultraminces de deux polymères: Polystyrène et Poly(acétate de vinyle). En réponse à la pression appliquée, les films polymères ont montré trois comportements pour le PS et le PVAc: élasticité, fluage et inflexion.

Pour les films **PS**, la transition entre ces comportements s'est avérée être liée au changement de niveau de pression, mais avec certaines exceptions pour certaines expériences, qui peuvent être expliquées par la sensibilité de l'expérience aux conditions de préparation de l'échantillon, au recuit et aux conditions expérimentales.

Le comportement de type élastique, au cours duquel la bulle croît pendant les premiers instants après le début de l'application de la pression et la hauteur de la bulle reste au même niveau pendant toute la durée de l'expérience, a été observé pour les expériences à faible niveau de pression, avec une légère transition vers le fluage pour des valeurs de

pression plus élevées. Les propriétés mécaniques du film polymère, la contrainte et la déformation, sont des constantes pour le régime de type élastique et sont inférieures à celles du comportement de fluage.

Le comportement de fluage a été observé pour des niveaux de pression plus élevés et a montré une forte dépendance de la hauteur de la bulle avec l'augmentation des niveaux de pression. L'évolution de la bulle dans le temps permet de calculer la conformité de fluage à partir des dépendances temporelles de la déformation et de la contrainte. La conformité au fluage a été calculée pour diverses expériences à différents niveaux de pression et à différentes températures de recuit (Fig.7.4). Les résultats de la conformité au fluage sont comparables aux études précédentes sur des films polymères similaires [29].

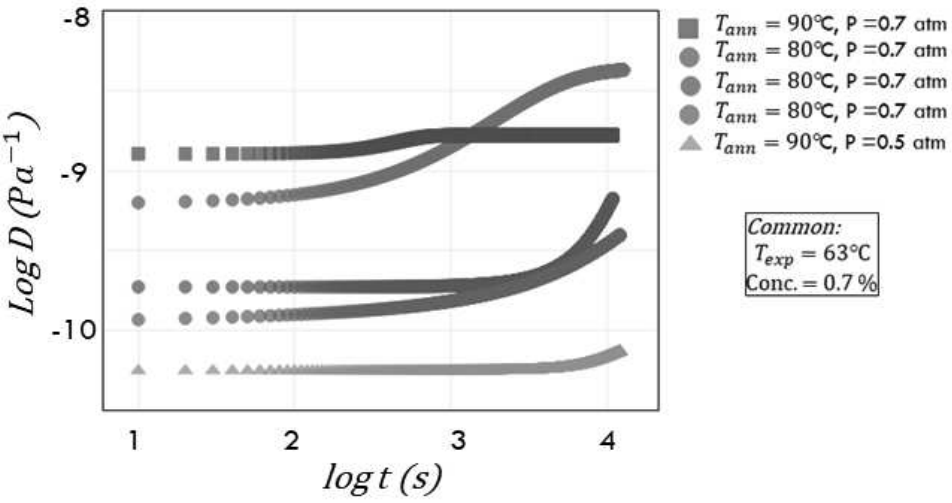

Figure 7.4: Les conformités de fluage pour les différentes expériences à différents niveaux de pression et différentes températures de recuit. Un niveau de pression plus élevé conduit à une augmentation des valeurs de conformité au fluage. De même, une température de recuit plus élevée entraîne une augmentation de la conformité au fluage pour la valeur de pression la plus élevée par rapport à la température de recuit la plus basse.

L'inflexion de la bulle a été observée pour certaines expériences à un niveau de pression élevé. La hauteur de la bulle s'est avérée plus dispersée que lors des expériences de fluage, car la forme de la bulle change après l'apparition des points d'inflexion. L'ajustement de la bulle afin d'extraire les propriétés mécaniques s'est avéré ne pas être valide car la forme de la bulle change et l'ajustement ne suit plus la forme de la bulle. Le changement de forme de la bulle prouve l'hypothèse selon laquelle la bulle dépasse le régime de fluage et se déforme dans un régime de type plastique, de sorte que le film polymère ne retrouve pas sa forme initiale après la suppression de la pression. Le mécanisme d'inflexion de la bulle

pour le gonflement des microbulles est inconnu et nécessite une étude plus approfondie.

Les expériences sur les films polymères **PVAc** ont été réalisées en fonction de l'humidité. Une forte corrélation entre le niveau d'humidité et la hauteur de la bulle a été observée (Fig.7.5), qui peut être couplée à la dépendance de la conformité de fluage à l'humidité.

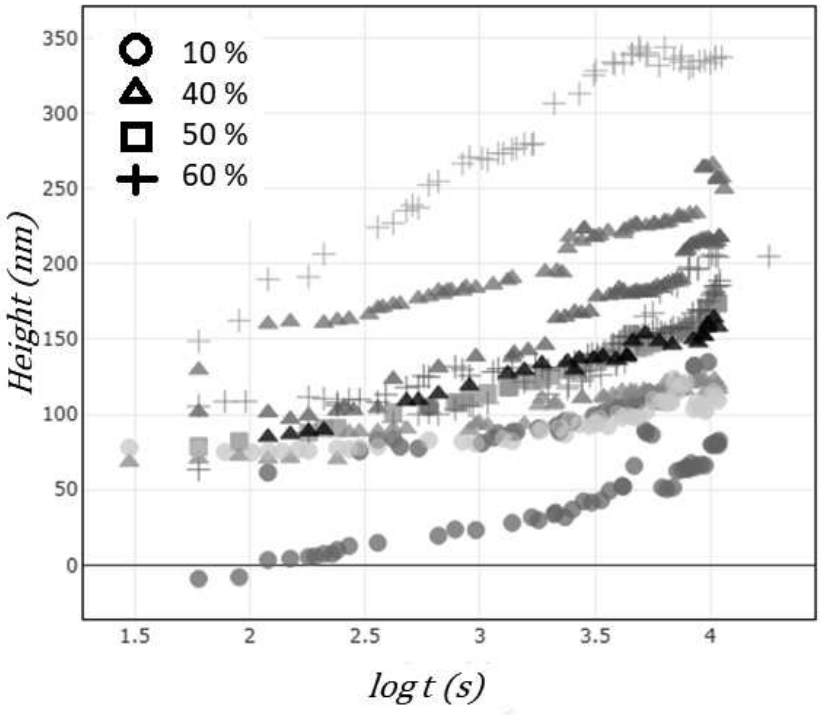

Figure 7.5: La dépendance de l'évolution de la déviation de la bulle au cours du temps de l'expérience (180 minutes). Quatre niveaux d'humidité différents présentés sous forme de symboles: 10% dans les triangles, 40% dans les cercles, 50% dans les carrés, 60% dans les croix.

Le résultat sur la hauteur de la bulle et la compliance au fluage prouve la suggestion que l'humidité agit comme un plastifiant sur les films ultraminces de PVAc.

L'inflexion des films polymères PVAc a été observée à des niveaux d'humidité élevés de 60%. Le comportement de la bulle après l'apparition des points d'inflexion a montré des similitudes avec l'inflexion des films PS à un niveau de pression élevé. La forme de la bulle est similaire pour les deux polymères pour le comportement d'inflexion, ce qui est un argument pour un processus identique d'apparition d'inflexion et un dépassement de la limite d'élasticité.

Pour étudier le processus et le mécanisme de la déflexion du film polymère avec la pression appliquée, afin d'extraire les propriétés mécaniques des films polymères, qui ne peuvent pas être obtenues par l'expérience, le **FEM** a été utilisé pour construire le

modèle et reproduire l'expérience d'inflation de microbulles sur le film PS. Le modèle a été validé par deux modèles d'essai, basés sur la pression et, de manière plus réaliste, sur le déplacement, par le calcul de la valeur de la pression et la comparaison avec l'entrée de pression initiale. Les deux modèles étaient en accord en ce qui concerne la pression. Le modèle de déplacement a ensuite été amélioré pour atteindre des dimensions réalistes afin de correspondre aux conditions expérimentales. Le module d'Young a été extrait du modèle final et s'est avéré être d'environ 11 GPa, ce qui est supérieur à la valeur de 5 GPa rapportée dans la littérature et à la valeur approximative de 7 GPa estimée à partir des données expérimentales de ce travail. Afin de diminuer le module d'Young et d'améliorer le modèle en même temps, la tension de surface a été implémentée dans le modèle sous la forme d'une précontrainte du film. La présence de la précontrainte a fait baisser le module d'Young, mais pas autant que prévu, la nouvelle valeur étant égale à 10.8 GPa. Pour résoudre la différence entre la valeur rapportée dans la littérature et la valeur du module de Young issue des simulations, la prédiction théorique sur la déviation de la bulle à partir de la pression appliquée a été utilisée et comparée aux simulations (Fig.7.6).

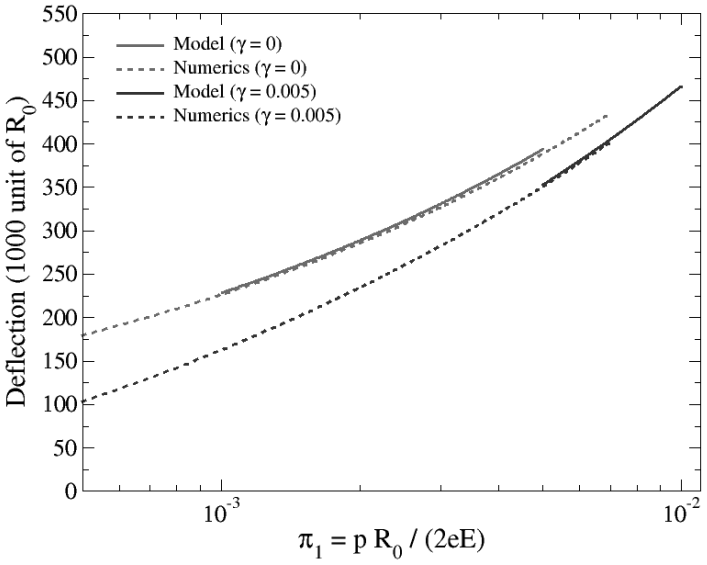

Figure 7.6: La prédiction théorique de la déviation des bulles, y compris avec et sans (γ=0) tension de surface, est présentée en lignes pleines. La déviation des bulles obtenue à partir des simulations est représentée par des lignes pointillées.

La prédiction théorique a montré un accord avec celle des simulations pour les deux cas, en incluant ou non la tension de surface dans le modèle. Le modèle peut être considéré comme fiable pour des recherches plus poussées sur le mécanisme et le comportement du film polymère pendant le gonflement des bulles.

Les perspectives du projet peuvent maintenant être avancées pour la partie expérimentale et la partie modélisation de ce travail. Étant donné que seule l'influence du niveau de pression des films PS a été étudiée dans ce travail, l'influence des autres caractéristiques

reste une question ouverte:

1. Procédure de recuit (y compris la température, la durée du recuit, la vitesse de refroidissement de l'échantillon). La possibilité d'attacher le film polymère à la grille sans recuit doit être envisagée. Cela permettrait d'éliminer le facteur énorme de l'influence sur le comportement du film polymère;

2. Epaisseur du film polymère. Le protocole de préparation du film polymère peut être étendu à des films polymères plus fins. De plus, la mesure de l'épaisseur du film polymère pour chaque échantillon augmentera les statistiques sur la valeur de l'épaisseur et diminuera l'erreur dans la détermination de T_g;

3. Le changement d'épaisseur de l'échantillon entraînera un changement de T_g et de la température de l'expérience pour maintenir l'échantillon à la valeur requise de $0.9T_g$;

Pour les films polymères PVAc, la question principale est d'avancer le protocole à des films polymères plus fins, ce qui conduirait à une diminution de T_g, qui conduirait également à des changements dans les conditions expérimentales.

Le modèle de simulation permettant d'imiter le gonflement des microbulles étant désormais prêt à être utilisé, la question du mécanisme d'inflexion des bulles reste ouverte. Comme il n'est pas possible d'extraire expérimentalement les propriétés mécaniques des films polymères pendant le comportement d'inflexion, la simulation de ce cas pourrait donner les réponses concernant ce phénomène.

L'étude du comportement des films polymères dans différentes conditions environnementales dans le cadre de ce travail de doctorat a permis d'obtenir des premières informations précieuses sur les propriétés mécaniques des films ultraminces. Malgré la complexité de l'expérience et des résultats intrigants, les tendances générales du comportement des films polymères ont été obtenues et analysées. L'apparition de trois comportements en réponse à différentes conditions environnementales pour les deux polymères présentés dans ce travail nous a permis de comparer et d'analyser en détail le processus de croissance des bulles. Comme le phénomène d'inflexion des bulles est apparu de la même manière pour les deux polymères, le mécanisme de son apparition est très probablement le même et reste l'un des points les plus prometteurs pour des investigations supplémentaires. La modélisation réalisée nous a permis de mimer l'expérience

d'inflation de microbulles, de compléter les résultats expérimentaux et d'extraire les propriétés mécaniques des films polymères ultrafins. La miniaturisation des films polymères étant l'une des principales questions de la physique des polymères aujourd'hui, de telles études utilisant l'interférométrie et la caractérisation optique pourraient être explorées plus largement afin d'améliorer les propriétés de ces films minces et leur permettre d'être utilisés dans de plus en plus de domaines de notre vie.

Appendix A

Viscoelastic properties of polymers

A.1 Strain and stress

The behavior of the polymer is based on the stress, strain and rate of strain and their relationship. The classical theory of elasticity describes the behaviour of the elastic solids, for which stress is always directly proportional to a strain at small deformations and independent of the rate of strain (Hooke's law). On the other hand, the classical theory of hydrodynamics describes the behaviour of viscous liquids, for which, stress is always proportional to the rate of strain but independent of the strain (Newton's law). As the viscoelastic polymers combine both solid-like and liquid-like behaviour, the stress-strain relation becomes more complicated [10].

The relationship between strain, stress and their time dependences are in general described by the rheological equation of state (or constitutive equation). For finite strain and rate of strain this equation may be complicated. But if strain and rate of strain are infinitesimal and stress-strain relations can be described by linear differential equations with constant coefficients (linear viscoelastic behaviour), the rheological equation of state is relatively simple.

The state of deformation at a given point in a viscoelastic system (as in a perfectly elastic body) is specified by the strain tensor. It represents the relative changes in dimensions and angles of a small cubical element at that point. The components of the infinitesimal strain tensor for an infinitesimal deformation in rectangular coordinates with the three Cartesian directions denoted by the subscripts 1,2,3 are

$$\gamma_{ij} = \begin{pmatrix} 2\partial u_1/\partial x_1 & \partial u_2/\partial x_1 + \partial u_1/\partial x_2 & \partial u_3/\partial x_+ \partial u_1/\partial x_3 \\ \partial u_2/\partial x_1 + \partial u_1/\partial x_2 & 2\partial u_2/\partial x_2 & \partial u_2/\partial x_3 + \partial u_3/\partial x_2 \\ \partial u_3/\partial x_1 + \partial u_1/\partial x_3 & \partial u_2/\partial x_3 + \partial u_3/\partial x_2 & 2\partial u_3/\partial x_3 \end{pmatrix}, \qquad \text{(A.1)}$$

where x_i and u_i are the coordinates of the point, where the strain is specified and its displacement in the strained state $u_i = x_i - x_i^0$ (superscript 0 corresponds to unstrained state).

Similarly, the rate of strain tensor $\dot{\gamma}_{ij}$ expresses the time derivatives of relative changes in dimensions and angles of that small cubical element at the point. This tensor is formulated similarly to A.1 by replacing the displacement in the strained point u_i by its time derivative $\partial u_i/\partial t = \vartheta_i$, the velocity of displacement.

The state of stress is specified by a stress tensor σ_{ij} which represents the forces acting on different faces of the cubical element from different directions

$$\sigma_{ij} = \begin{pmatrix} \sigma_{11} & \sigma_{12} & \sigma_{13} \\ \sigma_{21} & \sigma_{22} & \sigma_{23} \\ \sigma_{31} & \sigma_{32} & \sigma_{33} \end{pmatrix}, \qquad \text{(A.2)}$$

where the component of force per unit area σ_{ij}, parallel to the j direction, acting on the perpendicular to the i direction face of cubical element. The normal stresses are defined as being positive for tension and negative for compression.

A.2 Constitutive equation in simple shear

As the strain and stress tensors depend on the geometry and the form of deformation (for homogeneous deformations the stress and strain tensor are independent of x_i), the components of these tensors may take simpler forms [10]. One such deformation corresponds to simple shear, where two opposite faces of the cubic element are displaced by sliding (see Fig.A.1).

The strain and stress tensors for such geometry, respectively, are

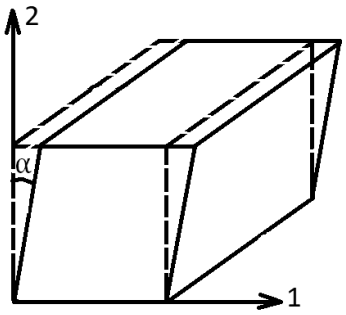

Figure A.1: Illustration of simple shear of a cubical element.

$$\gamma_{ij} = \begin{pmatrix} 0 & \gamma_{12} & 0 \\ \gamma_{21} & 0 & 0 \\ 0 & 0 & 0 \end{pmatrix}, \tag{A.3}$$

where $\gamma_{21} = \gamma_{12} = \partial u_1/\partial x_2 = \tan\,\alpha \cong \alpha$, and

$$\sigma_{ij} = \begin{pmatrix} \text{-P} & \sigma_{12} & 0 \\ \sigma_{21} & \text{-P} & 0 \\ 0 & 0 & \text{-P} \end{pmatrix}, \tag{A.4}$$

where P is an isotropic pressure.

The stress σ_{21} and strain γ_{21} are the functions of time and are connected by a constitutive equation for linear viscoelasticity, which has a simple form for a simple shear geometry. Assuming that sequential changes in strain are additive, the constitutive equation takes the form

$$\sigma_{21}(t) = \int_{-\infty}^{t} G(t-t')\dot{\gamma_{21}}(t')\,dt', \tag{A.5}$$

where $\dot{\gamma_{21}} = \partial\gamma_{21}/\partial t$ is the shear rate, $G(t)$ is the *relaxation modulus*, and as it keeps the history of strains in the sample, the integration is carried out over all past times t' up to the current moment in time t.

From an alternative point of view, the constitutive equation can be expressed for strain in terms of the history of the time derivatives of stress:

$$3\gamma_{21}(t) = \int_{-\infty}^{t} J(t-t')\dot{\sigma_{21}}(t')\,dt', \tag{A.6}$$

where $\dot{\sigma_{21}} = \partial\sigma_{21}/\partial t$, the $J(t)$ is the *creep compliance*.

With knowledge of either the relaxation modulus $G(t)$, or the creep compliance $J(t)$ of a particular material in the bulk, the relations between stress and strain for shear-like experiments can be predicted (for sufficiently small and/or slow motions).

The physical meaning of the relaxation modulus $G(t)$ and the creep compliance $J(t)$ can be explained by looking at various linear time-dependent experiments in shear, that are discussed below.

A.3 Relaxation modulus at stress relaxation after sudden strain

For such experiments that can be performed on both, viscoelastic liquids and viscoelastic solids, the shear strain γ is imposed for a short period of time ξ by a rate of strain $\dot{\gamma} = \gamma/\xi$ [10]. Then, the Eq.A.5 will take the form

$$\sigma_(t) = \int_{t_0-\xi}^{t_0} G(t-t')(\gamma/\xi)\, dt', \tag{A.7}$$

where t_0 is the time, when the strain is complete (and the rate of strain become zero). Using the theorem of Mean, the integral can be presented as

$$\sigma(t) = (\gamma/\xi)\xi G(t - t_0 + \epsilon\xi), \quad 0 \leq \epsilon \leq 1. \tag{A.8}$$

Let t_0 be equal to 0, then for the long time experiment compared to a short loading interval ξ ($\xi \ll$ t), the equation transforms into

$$\sigma(t) = \gamma G(t), \tag{A.9}$$

which shows the meaning of $G(t)$ as the time-dependent function of the stress-strain relation under the sudden strain conditions. For a perfect elastic solid the relaxation modulus $G(t)$ becomes time-independent and is called *the shear modulus* G, that is defined as σ/γ.

A.4 Creep compliance at creep after sudden stress

This experiment is opposite to the stress relaxation after a sudden strain, where, by analogy, a shear stress σ is applied for a short period before time $t = 0$ and maintained constant at $t > 0$. By using the same procedure for obtaining Eq.A.9 from Eq.A.5, the time dependence of strain $\gamma(t)$ can be obtained from Eq.A.6:

$$\gamma(t) = \sigma J(t). \tag{A.10}$$

Eq.A.10 shows the meaning of the creep compliance $J(t)$. For a perfect elastic solid $J = 1/G$, but for a viscoelastic material with a difference between the two experimental time patterns, $J(t) \neq 1/G(t)$ and the relation between $J(t)$ and $G(t)$ can take more complicated forms.

The examples above represent the relation between strain and stress for a simple shear experiment in the bulk. For the simple extension experiment, the relaxation modulus and creep compliance are represented by the tensile relaxation modulus (or Young's modulus) $E(t)$ and the tensile creep function $D(t)$ respectively.

Appendix B

R code for analysis of raw data

The **R** code of program **for** analysis of the raw **data** with profiles of 10–15 holes.

```
plotProfiles <- function (folderPath  # String. Full path to a folder
with data.
  , xShift = 20.01  # Decimal. If differnt from zero – shift bubble
                    # center to this coordinate on X axis.
                    # If equal to zero – do not perform any shift
, yShift = 200.0  # Decimal. Level up the membrane
                    to this coordinate
                    # in Y axis.
                    # Current membrane coordinate is obtained by
                    # averaging first 'yHeadAve' (see below) data points.

, yHeadAve = 5      # Integer. Number of data points for averaging of
                    # the membrane level.

, aveSeveralHoles = FALSE      # FALSE. Plot whole file content.
                               # In this case no averaging or fitting
                               #  is performed.
                               # or
                               # Integer. Average data over this
                               # many holes and apply fits.

, symmetrize = FALSE           # Boolean. Symmetrize the
                               # central region of the hole.
                               # Applied after
                               # averaging over holes.

, width = 1.5       # Decimal. width of the symmetrizing/fitting
                    # region  (in units as in the file).

, latPeriod = 13.685           # Decimal. Assume data periodicity
                               # with this approximate period.
                               # This should be a multiple of
                               # written data frequency
                               # (usually 0.115). 13.685 is a good
```

```
                                # choice.

, fitMethod = 'par'             # String.
                                #         'par' - parabolic function
                                #         'mat' - Matieu's function
                                # It is possible to do
                                # c ('par', 'mat') to fit separately
                                # using each method.

, filmThickness = 60.0          # Decimal. In nanometers.

, pressVec                      # Vector of pressure values.
                                # Should match to the list of files
                                # sorted alphabetically.

, timeVec)                      # Vector of time values.
                                # Should match to the list of files
                                # sorted alphabetically.

{
  library(data.table)
  library(plotly)
  library (stringr)

  checkDiff <- function (inputVec, diff, rever = FALSE)
  {
    if (rever)
    {
      j <- 1
      for (i in length (inputVec):2)
      {
        if (abs (inputVec[i-1] - inputVec[i]) > diff)
        {
          j <- length (inputVec) - i + 1
          break
        }
      }
      return (tail (inputVec, j))
    }
    else
    {
      j <- length (inputVec)
      for (i in 1:(length (inputVec) - 1))
      {
        if (abs (inputVec[i+1] - inputVec[i]) > diff)
        {
          j <- i
          break
        }
      }
      return (head (inputVec, j))
    }
  }

  corrManual <- function (inputVec2, plot = FALSE)
  {
    dataLength <- length (inputVec2)
    inputVec <- inputVec2 - mean (c (head (inputVec2, yHeadAve),
```

```
  tail (inputVec2, yHeadAve)))
  ccfVec <- rep (-1, times = dataLength * 2 + 1)

  for (lag in 0 : (dataLength * 2))
  {
    corrData <- data.frame(V1 = c (rep (0, times = dataLength)
                  , inputVec, rep (0, times = dataLength))
                  , V2 = c (rep (0, times = lag)
                  , rev (inputVec)
                  , rep (0, times = dataLength * 2 - lag)))

    ccx <- sum (corrData$V1 * corrData$V2)
    ccfVec[lag+1] <- ccx
  }

  if (plot == TRUE)
  {
    plot (ccfVec)
    plotData <- data.frame(V1 = c (rep (0, times = dataLength)
                  , inputVec, rep (0, times = dataLength))
                  , V2 = c (rep (0, times = which.max (ccfVec))
                  , rev (inputVec)
                  , rep (0, times = dataLength * 2
                  - which.max (ccfVec))))
    plot(0,0,xlim = c(0,119*3),ylim = c(-250,20),type = "n")
    lines (plotData[[1]], col = rainbow(2)[1], type = 'b')
    lines (plotData[[2]], col = rainbow(2)[2], type = 'b')
  }
  return (ccfVec)
}
getShiftedX <- function (inputDataFrame, xShift, All = TRUE
                  , latPeriod = latPeriod
                  , yHeadAve = yHeadAve)
{
  if (xShift != 0)
  {
    if (All)
    {
      workDataFrame <- inputDataFrame
    }
    else
    {
      workDataFrame <- subset (inputDataFrame
                  , V1 < inputDataFrame$V1[1] + latPeriod)
    }
  }
      # By manual corr
  CCX <- corrManual (workDataFrame$V2, plot = FALSE)
  tempMaxID <- floor (which.max (CCX) / 2)
  maxID <- tempMaxID
  # print (which.max(CCX))
  # print(maxID)
  shiftDiff <- 0.115 * maxID
  return (inputDataFrame$V1 + xShift - shiftDiff - inputDataFrame$V1[1])
}

getShiftedY <- function (inputDataFrame, yShift, yHeadAve)
{
```

```
    return (inputDataFrame$V2 + yShift
            - mean (head (inputDataFrame$V2, yHeadAve)))
  }

  files <- str_sort (list.files (path = folderPath
                      , full.names = TRUE), numeric = TRUE)
  inputData <- lapply (files , fread , header = FALSE
                      , data.table = FALSE)

  if (length (pressVec) != length (inputData))
  {
    stop ("Inconsistent input!
    Pressure vector length does not match number of files.")
  }
  if (length (timeVec) != length (inputData))
  {
    stop ("Inconsistent input!
    Time vector length does not match number of files.")
  }

  if (aveSeveralHoles)
  {
    inputDataAveraged <- list()
    for (fileID in 1:length (inputData))
    {
      # aveOver <- floor (tail (inputData[[fileID]]$V1, 1)
                          %/% latPeriod)
      # if (tail (inputData[[fileID]]$V1, 1)
                          %% latPeriod > 0.5 * latPeriod)
                           aveOver <- aveOver + 1
      print (paste ("File"
                  , fileID
                  , ": averaging over"
                  , aveSeveralHoles
                  , "holes ("
                  , tail (inputData[[fileID]]$V1, 1)
                  , "%%"
                  , latPeriod
                  , ").") )
      for (holeID in 1:aveSeveralHoles)
      {
        inputDataSelected <- subset (inputData[[fileID]]
                          , V1 >= inputData[[fileID]]$V1[1]
                             + (holeID - 1) * latPeriod & V1
                             < inputData[[fileID]]$V1[1]
                             + holeID * latPeriod)
        inputDataSelected$V1 <- as.character (getShiftedX
                                              (inputDataSelected
                                              , xShift
                                              , TRUE
                                              , latPeriod
                                              , yHeadAve))
        if (holeID == 1)
        {
          inputDataTemp <- inputDataSelected
        }
        else
        {
```

```
        inputDataTemp <- merge (inputDataTemp
                                , inputDataSelected
                                , by = colnames (inputDataSelected)[1]
                                , all.x = FALSE)
      }
    }

    # if (fileID == 7) View (inputDataTemp[, 2:ncol(inputDataTemp)])

    inputDataAveraged[[fileID]] <- data.frame
                  (V1 = as.numeric (inputDataTemp$V1)
                  , V2 = rowMeans (inputDataTemp[,
                       2:ncol(inputDataTemp)])
                  , V3 = matrixStats::rowSds(as.matrix
                  (inputDataTemp[, 2:ncol(inputDataTemp)])))

    if (symmetrize)
    {
      centerPos <- which (inputDataAveraged[[fileID]]$V1 == xShift)
      range <- width %/% 0.115
      symmetricDF <- inputDataAveraged[[fileID]]
      for (rowID in 1:nrow (symmetricDF))
      {
        if ((rowID > (centerPos - range)) &
            (rowID < (centerPos + range)))
        {
          symmetricDF$V2[rowID] <- (symmetricDF$V2[rowID]
          + symmetricDF$V2[rowID
          + 2 * (centerPos - rowID)]) / 2.0
        }
      }
      inputDataAveraged[[fileID]] <- symmetricDF
    }
    inputDataAveraged[[fileID]] $V2shifted <- getShiftedY
   (inputDataAveraged[[fileID]]
   , yShift, yHeadAve)
  }
  inputData <- inputDataAveraged
}

print ("Done preparing")

names (inputData) <- str_sort (list.files (path = folderPath)
                               , numeric = TRUE)
dataNames <- names (inputData)

matFittedData <- vector (mode = 'list', length = length (inputData))
parFittedData <- vector (mode = 'list', length = length (inputData))

fitSummary <- data.frame (File = names (inputData)
                          , Rpar = rep (NA, length (inputData))
                          , R = rep (NA, length (inputData))
                          , R1 = rep (NA, length (inputData))
                          , Alpha = rep (NA, length (inputData))
                          , Beta = rep (NA, length (inputData)))

plotObj <- plot_ly (type = 'scatter'
                    , mode = 'lines')
```

```
parFitList <- vector (mode = 'list', length = length (inputData))
parFitFormula <- V2 ~ A * V1^2 + B * V1 + C

matFitList <- vector (mode = 'list', length = length (inputData))
matFitFormula <- V2 ~ R1 *
((1 - (abs(V1) / R1)^Alpha)^(1 / Alpha)
- (1 - (R / R1)^Alpha)^(1 / Alpha))# + A0

elasticData <- data.frame (Pressure = pressVec
          , Time = timeVec
          , Curvature = rep(NA, times = length (inputData))
          , RadiusOfCurvature = rep(NA, times = length (inputData))
          , Stress = rep(NA, times = length (inputData))
          , Strain = rep(NA, times = length (inputData)))

for (fileID in 1:length (files))
{
  plotObj <- plotObj %>%
  add_trace (x = getShiftedX (inputData[[fileID]]
  , xShift, ifelse (nrow (inputData[[fileID]])
      > 1.5 * latPeriod / 0.115, FALSE, TRUE)
      , latPeriod
      , yHeadAve) * 1000
           , y = getShiftedY (inputData[[fileID]]
                              , yShift, yHeadAve)
           # , error_y = list(array=inputData[[fileID]]$V3)
           , name = dataNames[[fileID]])

  if (aveSeveralHoles)
  {

    if ('par' %in% fitMethod)
    {
      fitData <- subset (data.frame (V1 = inputData[[fileID]]$V1
                       , V2 = getShiftedY (inputData[[fileID]]
                       , yShift = yShift, yHeadAve = yHeadAve))
                      , V1 > (xShift - width) & V1 < (xShift + width))
      fitData$V1 <- fitData$V1 * 1000.0

      print (fileID)

      parFitList[[fileID]] <- nls (formula = parFitFormula
                                   , data = fitData
                                   , start = list (A = 0.000001
                                                   , B = 0.000001
                                                   , C = 1.0)
                                   , control = list (minFactor = 1e-9))

      print(parFitList[[fileID]]$m$getAllPars())


      parFittedData[[fileID]] <- data.frame (V1 = fitData$V1
                         , V2 = predict (parFitList[[fileID]]
                         , list(V1 = fitData$V1)))

      plotObj <- plotObj %>%
        add_lines (x = parFittedData[[fileID]]$V1
```

```
                , y = parFittedData[[fileID]]$V2
                #predict (parFitList[[fileID]]
                #, list(V1 = fitData$V1))
                , name = paste (dataNames[fileID], "fit par"))

  xMax <- parFittedData[[fileID]]$V1[which.max (parFittedData[[fileID]]$V2)]
  # print (xMax)
  rCurv <- (1 + (2 * parFitList[[fileID]]$m$getAllPars()["A"] * xMax
  + parFitList[[fileID]]$m$getAllPars()["B"])^2)
  ^ 1.5 / (abs (2 * parFitList[[fileID]]$m$getAllPars()["A"]))
  stress <- pressVec[fileID] * rCurv / (2 * filmThickness)
  rHole <- 2500
  # strain <- rCurv / (rHole * sin (rHole / rCurv)) - 1
  strain <- rCurv * asin (rHole / rCurv) / rHole - 1

  elasticData$Curvature[fileID] = 1 / rCurv
  elasticData$RadiusOfCurvature[fileID] = rCurv
  elasticData$Stress[fileID] = stress
  elasticData$Strain[fileID] = strain
  fitSummary$Rpar[[fileID]] <- rCurv
  # print (paste (fileID, "done"))\
}

if ('mat' %in% fitMethod)
{
  fitData <- subset (data.frame (V1 = inputData[[fileID]]$V1
                                 , V2 = getShiftedY (inputData[[fileID]]
                                 , yShift = yShift, yHeadAve = yHeadAve))
                     , V1 > (xShift - width) & V1 < (xShift + width))
  fitData$V1 <- fitData$V1 * 1000.0
  fitData$V1 <-  fitData$V1 - xShift * 1000

  matFitList[[fileID]] <- nls (formula = matFitFormula
                               , data = fitData
                               , start = list (R1 = 10000
                                               , R = 1000
                                               , Alpha = 1.61)
                                               # , A0 = 80)
                               , control = list (maxiter = 100
                                                 , minFactor = 1e-20
                                                 , tol = 1e-4
                                                 , printEval = TRUE))

  matFittedData[[fileID]] <- data.frame (V1 = fitData$V1
                                         , V2 = predict (matFitList[[fileID]]
                                         , list(V1 = fitData$V1)))

  plotObj <- plotObj %>%
    add_lines (x = matFittedData[[fileID]]$V1
    + xShift * 1000#fitData$V1 + xShift * 1000
              , y = matFittedData[[fileID]]$V2#predict
              #(matFitList[[fileID]], list(V1 = fitData$V1))
              , name = paste (dataNames[fileID], "fit mat"))

  fitSummary$R[fileID] <- matFitList[[fileID]]$m$getAllPars()["R"]
  fitSummary$R1[fileID] <- matFitList[[fileID]]$m$getAllPars()["R1"]
  fitSummary$Alpha[fileID] <- matFitList[[fileID]]$m$getAllPars()["Alpha"]
  fitSummary$Beta[fileID] <- 1 / matFitList[[fileID]]$m$getAllPars()["Alpha"]
```

```
      }
    }
  }

  plotObj <- plotObj %>% layout (xaxis = list (title = "X (mm)")
                                 , yaxis = list (title = "Y (mm)"))

  print ("Done plotting")

  retList <- list (inputData = inputData
                   , plot = plotObj
                   , parFitList = parFitList
                   , matFitList = matFitList
                   , ElasticData = elasticData
                   , fitSummary = fitSummary)
  return (retList)
}



tempData <- plotProfiles (folderPath = "C:/DiskD/PhD/Nast/24_07_20_TXT_corrected/"
                          , xShift = 20.01
                          , yShift = 200.0
                          , yHeadAve = 5
                          , aveSeveralHoles = 10
                          , symmetrize = FALSE
                          , width = 1.5
                          , latPeriod = 13.685
                          , fitMethod = 'par'
                          , filmThickness = 30.0
                          , pressVec = rep (0.7, 33) * 10^5
                          , timeVec = c(1.5, 2, 2.5, 4, 4.3, 4.6, 5, 6, 11
                                        , 15, 16, 20, 21, 24, 27, 28, 29, 33
                                        , 40, 42, 49, 62, 68, 71, 74, 79, 87
                                        , 96, 106, 106.5, 113, 117, 121) * 60)

tempData$plot
```

The program to calculate the stress and strain, to determine their time dependencies and to determine the creep compliance is presented below. The program should be used in couple with previous one.

```
stressExpFitFormula <- Stress ~ sigma_0 + sigma_1 *
                       exp (-1 * (Time / tau) ^ Beta_sigma)
strainExpFitFormula <- Strain ~ epsilon_0 + epsilon_1 *
                       (1 - exp (-1 * (Time / tau) ^ Beta_epsilon))
library (minpack.lm)
stressNlsFitObj <- nlsLM (formula = stressExpFitFormula
                          , data = data.frame (Time = tempData$ElasticData$Time
                          , Stress = tempData$ElasticData$Stress)
                          , start = list (sigma_0 = 10^6
                                          , sigma_1 = 10^6
                                          , tau = 10^3
                                          , Beta_sigma = 1.0)
                          , lower = c (0.0, 0.0, 0.0, 0.0)
```

```
                              , control = list(maxiter = 500
                                               , warnOnly = TRUE))

strainNlsFitObj <- nlsLM (formula = strainExpFitFormula
                              , data = data.frame (Time = tempData$ElasticData$Time
                                                   , Strain = tempData$ElasticData$Strain)
                              , start = list (epsilon_0 = 10^-4
                                              , epsilon_1 = 10^-2
                                              , tau = 10^4
                                              , Beta_epsilon = 1.0)
                              , lower = rep (0.0, times = 4)
                              , control = list(maxiter = 500))

tempTimes <- seq (from =   min (tempData$ElasticData$Time)
                  , to = max (tempData$ElasticData$Time)
                  , by = 10)
stressDataFitted <- data.frame (Time = tempTimes
                                , Stress = predict (stressNlsFitObj
                                , data.frame (Time = tempTimes)))
strainDataFitted <- data.frame (Time = tempTimes
                                , Strain = predict (strainNlsFitObj
                                , data.frame (Time = tempTimes)))

creepComplianceSum <- data.frame (Time = tempTimes
                                , Stress = predict (stressNlsFitObj
                                , data.frame (Time = tempTimes))
                                , Strain = predict (strainNlsFitObj
                                , data.frame (Time = tempTimes))
                                , deltaD = 0.0
                                , D = NA)

Dg <- creepComplianceSum$Strain[[1]]/creepComplianceSum$Stress[[1]]

creepComplianceSum$deltaD[[1]] <- Dg
creepComplianceSum$D[[1]] <- Dg


creepComplianceSum$deltaD[[2]] <- 2 * (creepComplianceSum$Strain[[2]]
                                - Dg *creepComplianceSum$Stress[[2]])
                                /creepComplianceSum$Stress[[1]]

creepComplianceSum$D[[2]] <- Dg + creepComplianceSum$deltaD[[2]]

for (i in 3:nrow(creepComplianceSum))
{
  S <- 0
  for (j in 1:(i-2))
  {
    S <- S + creepComplianceSum$Stress[[i-j+1]] * creepComplianceSum$deltaD[[j+1]]
  }
  creepComplianceSum$deltaD[[i]] <-  2 * (creepComplianceSum$Strain[[i]]
  - Dg * creepComplianceSum$Stress[[i]] - S)/creepComplianceSum$Stress[[1]]

  creepComplianceSum$D[[i]] <- sum(head(creepComplianceSum$deltaD, i))
}

creepComplianceSum["CreepCompliance"]] <- creepComplianceSum["Strain"]]
                                          /creepComplianceSum["Stress"]]
```

Bibliography

[1] G. E. Moore. *Lithography and the Future of Moore's Law*. SPIE, Vol. 2439 (1995).

[2] K. J. Kuhn. *Moore's Law Past 32nm: Future Challenges in Device Scaling*. IEEE 13th International Workshop on Computational Electronics (IWCE) (2009) 1-6.

[3] J. L. Keddie, R. A. L. Jones. *Glass Transition Behavior in Ultra-Thin Polystyrene Films*. Israel Journal of Chemistry Vol. 35, (1995).

[4] J. L. Keddie, R. A. L. Jones, R. A. Cory. *Interface and surface effects on the glass transition temperature in thin polymer films*. Faraday discuss, 98 (1994) 219-230.

[5] C. B. Roth, J. R. Dutcher. *Glass transition and chain mobility in thin polymer films*. Journal of Electroanalytical Chemistry, 584 (2005) 13–22.

[6] P. G. De Gennes. *Glass transitions in thin polymer films*. The European Physical Journal E, 2(3) (2000) 201–205.

[7] R. F. Landel, L. E. Nielsen. *Mechanical Properties of Polymers and Composites*. CRC Press, (1993).

[8] J. Brandrup, E. H. Immergut, E. A. Grulke. *Polymer handbook (4th Edition)*. Wiley, New York (1999).

[9] J. L. Keddie, R. A. L. Jones, R. A. Cory. *Size-dependent depression of the glass transition temperature in polymer films*. Europhys. Lett., 27(l) (1994) 59-64.

[10] J. D. Ferry. *Viscoelastic properties of polymers (3rd Edition)*. Wiley: New York, (1980).

[11] J. A. Forrest, K. Dalnoki-Veress. *The glass transition in thin polymer films*. Advances in Colloid and Interface Science, 94 (2001) 167.

[12] P. G. De Gennes. *Reptation of a polymer chain in the presence of fixed obstacles*. The Journal of Chemical Physics, 55(2) (1971) 572–579.

[13] O. Prucker, S. Christian, H. Bock, J. Rühe, C. W. Frank, W. Knoll. *Glass Transition in Ultrathin Polymer Films*. Organic Thin Films, 17 (1998) 233–249.

[14] W. E. Wallace, J. H. van Zanten, W. L. Wu. *Influence of an impenetrable interface on a polymer glass-transition temperature*. Physical Review E, 52(4) (1995) R3329–R3332.

[15] C. J. Ellison, J. M. Torkelson. *The distribution of glass-transition temperatures in nanoscopically confined glass formers*. Nature Mat., 2 (2003) 695-700.

[16] J. A. Forrest, K. Dalnoki-Veress, J. R. Stevens, J. R. Dutcher. *Effect of free surfaces on the glass transition temperature of thin polymer films*. Physical Review Letters, 77(10) (1996) 2002-2005.

[17] K. Dalnoki-Veress, J. A. Forrest, J. R. Dutcher. *Interface and chain confinement effects on the glass transition temperature of thin polymer films*. Physical Review E, 56(5) (1997) 5705-5716.

[18] J. Mattsson, J. A. Forrest, L. Börjesson. *Quantifying glass transition behavior in ultrathin free-standing polymer films*. Physical Review E, 62(4) (2000) 5187-5200.

[19] K. Dalnoki-Veress, J. A. Forrest, C. Murray, C. Cigault, J. R. Dutcher. *Molecular weight dependence of reductions in the glass transition temperature of thin,freely standing polymer films*. Physical Review E, 63(3) (2001) 031801.

[20] H. Bodiguel, C. Fretigny. *Viscoelastic properties of ultrathin polystyrene films*. Macromolecules, 40 (2007) 7291-7298.

[21] H. Hasegawa, T. Ohta, K. Ito, H. Yokoyama. *Stress-strain measurement of ultrathin polystyrene films: film thickness and molecular weight dependence of crazing stress*. Polymer, 123 (2017) 179-183.

[22] J. Haudin. *Handbook of Materials Behavior Models Volume I —— Plasticity of Polymers*. (2001) 255–264.

[23] A. L. Smith, R. B. Mulligan, H. M. Shirazi. *Determining the effects of vapor sorption in polymers with the quartz crystal microbalance/heat conduction calorimeter*. Journal of Polymer Science Part B: Polymer Physics, 42(21), (2004) 3893–3906.

[24] B. D. Vogt, C. L. Soles, H.-J. Lee, E. K. Lin, W.-L. Wu. *Moisture absorption into ultrathin hydrophilic polymer films on different substrate surfaces*. Polymer, 46(5) (2005) 1635–1642.

[25] M. Mukherjee, M. Souheib Chebil, N. Delorme, A. Gibaud. *Power law in swelling of ultra-thin polymer films*. Polymer, 54(17) (2013) 4669–4674.

[26] A. Singh, M. Mukherjee. *Swelling Dynamics of Ultrathin Polymer Films*. Macromolecules, 36(23) (2003) 8728–8731.

[27] R. M. Hodge, T. J. Bastow, G. H. Edward, G. P. Simon, A. J Hill. *Free Volume and the Mechanism of Plasticization in Water-Swollen Poly(vinyl alcohol)*. Macromolecules, 29(25) (1996) 8137–8143.

[28] W. G. Knauss, V. H. Kenner. *On the hygrothermomechanical characterization of polyvinyl acetate*. Journal of Applied Physics, 51(10) (1980) 5131.

[29] P. A. O'Connel, S. A. Hutcheson, G. B. McKenna. *Creep Behavior of Ultra-Thin Polymer Films*. J. of Pol. Sci., 46 (2008) 1952-1965.

[30] H. K. Nguyen, M. Labardi, M. Lucchesi, P. Rolla, D. Prevosto. *Plasticization in Ultrathin Polymer Films: The Role of Supporting Substrate and Annealing*. Macromolecules, 46(2) (2013) 555–561.

[31] S. Kim, M. K. Mundra, C. B. Roth, J. M. Torkelson . *Suppression of the T_g - Nanoconfinement Effect in Thin Poly(vinyl acetate) Films by Sorbed Water*. Macromolecules, 43(11) (2010) 5158–5161.

[32] K. E. Al Ani, A. E. Ramadhan. *Kinetic Study of the Effect of Plasticization on Photodegradation of Polystyrene Solid Films*. Materials Sciences and Applications, 6 (2015) 617-633.

[33] N. R. Horn, D. R. Paul. *Carbon Dioxide Sorption and Plasticization of Thin Glassy Polymer Films Tracked by Optical Methods*. Macromolecules, 45 (2012) 2820-2834.

[34] J. L. Ellis, H. G. L. Coster, T. C. Chilcott, D. L. Tomasko, F. Dehghani. *Structure and Characterization of Polystyrene Thin Films*. Proceedings of 9th International Symposium on Supercritical Fluids, Arcachon, France (2009).

[35] G. Reiter. *Mobility of Polymers in Films Thinner than Their Unperturbed Size*. Europhysics Letters, 23(8) (1993) 579-584.

[36] F. Saulnier, E. Raphael, P. G. De Gennes. *Dewetting of thin-film polymers*. Physical Review, E 66 (2002) 061607.

[37] C. B. Roth, B. G. Nickel, J. R. Dutcher. *Differential Pressure Experiment to Probe Hole Growth in Freely Standing Polymer Films*. Review of Scientific Instruments, 74(5) (2003) 2796.

[38] C. Rotella, S. Napolitano, L. De Cremer, G. Koeckelberghs, M. Wubbenhorst. *Distribution of Segmental Mobility in Ultrathin Polymer Films*. Macromolecules, 43 (2010) 8686-8691.

[39] A. B. Mann. *Nanoindentation. Surfaces and Interfaces for Biomaterials*. (2005) 225–247.

[40] Z. Hu. *Characterization of Materials, Nanomaterials, and Thin Films by Nanoindentation*. Microscopy Methods in Nanomaterials Characterization, (2017) 165–239.

[41] C. M. Stafford, B. D. Vogt, C. Harrison, D. Julthongpiput, R. Huang. *Elastic Moduli of Ultrathin Amorphous Polymer Films*. Macromolecules, 39(15) (2006) 5095-5099.

[42] J. M. Torres, C. M. Stafford, B. D. Vogt. *Impact of molecular mass on the elastic modulus of thin polystyrene films*. Elsevier Polymer, 51 (2010) 4211-4217.

[43] R. K. Bay, A. J. Crosby. *Uniaxial Extension of Ultrathin Freestanding Polymer Films*. ACS Macro Letters, 8 (2019) 1080-1085.

[44] P. A. O'Connel and G. B. McKenna. *Rheological Measurements of the Thermoviscoelastic Response of Ultrathin Polymer Films*. Science, 307, 1760 (2005).

[45] F. Espinosa-Loza, M. Stadermann, C. Aracne-Ruddle, R. Casey, P. Miller, R. Whitesides. *Modeling the mechanical properties of ultra-thin polymer films*. High Power Laser Science and Engineering, 5(27) (2017).

[46] P. S. Crider, M. R. Majewski, J. Zhang, H. Oukris, N. E. Israeloffa. *Local dielectric spectroscopy of polymer films*. Appl. Phys. Lett., 91 (2007) 013102.

[47] S. Xu, P. A. O'Connell, G. B. McKenna, S. Castagnet. *Nanomechanical properties in ultrathin polymer films: Measurement on rectangular versus circular bubbles*. Journal of Polymer Science Part B: Polymer Physics, 50(7) (2011) 466–476.

[48] O. O. Okudur, K. Vanstreels, I. De Wolf, U. Hangen. *Extraction of elastic modulus of porous ultra-thin low-k films by two-dimensional finite-element simulations of nanoindentation*. Journal of Applied Physics, 119(2) (2016) 025302.

[49] M. Zhang, Y. Li, P. V. Kolluru, L. C. Brinson. *Determination of Mechanical Properties of Polymer Interphase Using Combined Atomic Force Microscope (AFM) Experiments and Finite Element Simulations*. Macromolecules, 51, 20 (2018) 8229–8240.

[50] D. W. Grainger and D. G. Castner. *Surface Analysis and Biointerfaces: Vacuum and Ambient In Situ Techniques*. Comprehensive Biomaterials, 1–22 (2011).

[51] J. E. Pye, C. B. Roth, *Two Simultaneous Mechanisms Causing Glass Transition Temperature Reductions in High Molecular Weight Freestanding Polymer Films as Measured by Transmission Ellipsometry*. Physical Review Letters, 107 (2011) 235701.

[52] L. Bakshi, S. Eliezer, Z. Henis, N. Nissim, L. Perelmutter, D. Moreno, M. Sudai, M. Mond. *Equations of State and the ellipsometry diagnostics*. Laser and Particle Beams, 27 (2009) 79–84 .

[53] M. Gilliot. *Errors in ellipsometry data fitting*. Optics Communications, 427 (2018) 477-484.

[54] G. Binnig, C. F. Quate, Ch. Gerber. *Atomic force microscope*. Phys. Rev. Lett., 56 (9) (1986) 930-933.

[55] I. Sokolov, M. E. Dokukin, N. V. Guz. *Method for quantitative measurements of the elastic modulus of biological cells in AFM indentation experiments*. Methods, 60(2) (2013) 202–213.

[56] Y. Martin, C. C. Williams, H. K. Wickramasinghe. *Atomic force microscope – force mapping and profiling on a sub 100Å scale*. J. Appl. Phys., 61 (1987) 4723-4729.

[57] Q. Zhong, D. Inniss, K. Kjoller, V. B. Elings. *Fractured polymer/silica fiber surface studied by tapping mode atomic force microscopy.* Surface Science Letters, 290(1-2) (1993) 688-692.

[58] K. Miyake, N. Satomi, S. Sasaki. *Elastic modulus of polystyrene film from near surface to bulk measured by nanoindentation using atomic force microscopy.* Appl. Phys. Lett., 89(3) (2006) 031925.

[59] M. Chyasnavichyus, S. L. Young, V. V. Tsukruk. *Probing of polymer surfaces in the viscoelastic regime.* Langmuir, 30(35) (20) 10566–10582.

[60] P. A. O'Connel and G. B. McKenna, *Novel nanobubble inflation method for determining the viscoelastic prorerties of ultrathin polymer films.* Rev. Sci. Instrum., 78 (2007) 013901.

[61] A. Koorikkat, O. Payton, L. Picco, W. Schwarzacher. *Imaging the surface of a polycrystalline electrodeposited Cu film in real time using in situ high-speed AFM.* J. Electrochem. Soc., 167 (2020) 162510.

[62] T. Ando, T. Uchihashi, N. Kodera. *High-speed AFM and applications to biomolecular systems.* Annual Review of Biophysics, 42(1) (2013) 393–414.

[63] P. J. De Groot. *Principles of interference microscopy for the measurement of surface topography.* Advances in Optics and Photonics, 7(1) (2015) 1.

[64] D. Sundeep, A G. Krishna, T V. Kumar. *Spectroscopic Investigations of MoO3/CuO Nanocomposites.* Scholars' Press (2016).

[65] K. Kitagawa. *Thin film thickness profile measurement using an interferometric surface profiler.* Proc. of SPIE, Vol. 6716 (2006) 671607-1.

[66] P. J. De Groot, X. C. De Lega. *Transparent film profiling and analysis by interference microscopy.* Proc. of SPIE, Vol. 7064 (2008) 70640I-3.

[67] D. I. Mansfield. *Thin film extraction from scanning white light interferometry.* Proc. SPIE, Optifab 10316 (2007) 1031626.

[68] P. Chapuis, P. C. Montgomery, F. Anstotz, A. Leong-Hoï, C. Gauthier, J. Baschnagel, G. Reiter, G. B. McKenna, A. Rubin. *A novel interferometric method for the study of the*

viscoelastic properties of ultrathin polymer films determined from nanobubble inflation. Rev. Sci. Instrum., 88 (2017) 093901.

[69] *https://www.aquamarijn.nl/shop/high-porosity-microsieves/* Accessed on 8th of Nomember, 2021.

[70] E. Liu, K. Sakurai. *Slow dynamics in thermal expansion of polyvinyl acetate thin film with interface layer.* Polymer Journal (2019).

[71] P. C. Montgomery, P. Chapuis, A. Leong-Hoï, F. Anstotz, A. Rubin, J. Baschnagel, C. Gauthier, G. Reiter, and G. B. McKenna. *Optical nanoscopy characterization of nanofilms.* J. Phys.: Conf. Ser., 780 (2017) 012003.

[72] S. Xu. *Mechanical properties of ultrathin polymer films investigated by a nanobubble inflation technique: surface tension, geometry and molecular architecture effects.* Dessertation, Graduate Faculty of Texas Tech University (2011).

[73] P. C. Montgomery, D. Montaner, F. Salzenstein. *Tomographic analysis of medium thickness transparent layers using white light scanning interferometry and XZ fringe image processing.* Proc. SPIE, 8430 (2012) 843014.

[74] P. C. Montgomery, A. Leong-Hoï, F. Anstotz, D. Mitev, L. Pramatarova, O. Haeberle. *From superresolution to nanodetection: overview of far field optical nanoscopy techniques for nanostructures.* J. Phys.: Conf. Ser., 682 (2016) 012010.

[75] R Core Team. *R: a language and environment for statistical computing, R Foundation for Statistical Computing.* Vienna, Austria (2021).

[76] R. Bracewell. *Pentagram Notation for Cross Correlation." The Fourier Transform and Its Applications.* New York: McGraw-Hill (1965) pp. 46, 243.

[77] P. A. O'Connell, G. B. McKenna. *Dramatic stiffening of ultrathin polymer films in the rubbery regime.* Eur. Phys. J., E 20 (2006) 143–150.

[78] J. E. Mark. *Physical Properties of Polymers Handbook.* AIP Press, New York (1996).

[79] M.F. Ashby, D.R.H Jones,. *Engineering Materials 1—An Introduction to Properties, Applications, and Design.* Elsevier: Amsterdam, The Netherlands (2012) p.317.

[80] J.Chang, K. B. Toga, J. D. Paulsen, N. Menon, T. P. Russell. *Thickness Dependence of the Young's Modulus of Polymer Thin Films*. Macromolecules, 51, 17 (2018) 6764–6770.

Université de Strasbourg

Anastasiia SHPIRUK

École doctorale Physique, chimie-physique ED 182 Université de Strasbourg

Modélisation et étude expérimentale des propriétés viscoélastiques de films polymères ultra-minces par technique de gonflement couplée à la microscopie interférométrique.

Résumé

Cette thèse est axée sur l'étude du comportement des films polymères ultraminces et en particulier sur leurs propriétés mécaniques dans différentes conditions environnementales telles que la température, la pression et l'humidité. Le premier polymère utilisé dans ce travail est le polystyrène (PS) afin d'étudier l'influence de différents niveaux de pression et le comportement du film polymère en réponse à la pression appliquée. Le deuxième polymère, le poly(acétate de vinyle) (PVAc), a été utilisé pour étudier l'influence de différents niveaux d'humidité sur le comportement des films ultraminces de PVAc sous la pression constante appliquée. Enfin, la méthode des éléments finis (FEM) a été utilisée dans l'environnement Marc Mentat pour simuler l'expérience et obtenir les propriétés mécaniques qui ne sont pas disponibles à partir de l'expérience. En particulier, nous nous concentrons sur l'effet de fluage des films polymères ultraminces et l'atteinte du point de seuil, dans le but d'essayer de comprendre les deux processus et la transition entre eux, tant du point de vue expérimental que de la modélisation.
Le chapitre 2 présente une vue d'ensemble de la littérature, les principales caractéristiques des propriétés mécaniques et physiques des films confinés par rapport à la masse, ainsi que les méthodes d'étude et de caractérisation. Le chapitre 3 présente les matériaux et les méthodes utilisés dans ce travail. Ensuite, le chapitre 4 contient les résultats et l'analyse des expériences sur les films PS et PVAc. Les résultats et les détails des simulations sont présentés dans le chapitre 5. Enfin, les conclusions et les perspectives du projet sont données dans le chapitre 6.
Mots clés : films polymères ultrafins, technique de gonflage par microbulles, interférométrie, méthode des éléments finis, polystyrène, poly(acétate de vinyle).

Résumé en anglais

The thesis is focused on the investigations of the behavior of ultrathin polymer films and in particular on their mechanical properties under different environmental conditions such as temperature, pressure and humidity. The first polymer that was used in this work is Polystyrene (PS) in order to investigate the influence of different pressure levels and how the polymer film behaves in response to the applied pressure. The second polymer, Poly(vinyl acetate) (PVAc) was used to investigate the influence of different humidity levels on the behavior of ultrathin PVAc films under the applied constant pressure. Finally, the Finite Element Method (FEM) was used in the Marc Mentat environment to simulate the experiment and to obtain the mechanical properties that are not available from experiment. In particular, we concentrate on the creep effect of ultrathin polymer films and the reaching of the threshold point, with the aim of trying to understand both processes and the transition between them from both, the experimental and modeling points of view.

In Chapter 2 an overview of the literature is given together with the main features of the mechanical and physical properties of confined films in comparison to the bulk, as well as the methods of their investigation and characterization. Chapter 3 presents the materials and methods used in this work. Then, Chapter 4 contains the results and analysis of the experiments on the PS and PVAc films. The results and details of simulations are presented in Chapter 5. Finally, the conclusions and perspectives of the project are given in Chapter 6.

Keywords : ultrathin polymer films, microbubble inflation technique, interferometry, finite element method, polystyrene, poly(vinyl acetate).